Optothermoacoustic Methods for Low-Cost Air Quality Monitoring

Philipp Breitegger

Supervisor: Prof. A. Bergmann

Institute of Electrical Measurement and Sensor Systems
Graz University of Technology

This dissertation is submitted for the degree of
Doktor der technischen Wissenschaften

Graz

March 2020

Declaration

I declare that I have authored this thesis independently, that I have not used other than the declared sources/resources, and that I have explicitly indicated all material which has been quoted either literally or by content from the sources used. The text document uploaded to TUGRAZonline is identical to the present doctoral dissertation.

Philipp Breitegger
March 2020

Acknowledgements

First of all I want to thank my supervisor, Prof. Alexander Bergmann, for his guidance, enriching discussions and contributions to the scientific quality of this work.

I appreciate the outstanding works of my master students Markus Knoll, Alexander Kerschhofer and Martin Lampel.

Further I want to thank my friends and colleagues Mario Schriefl, Reinhard Klambauer, Alexander Schossmann, Martin Kupper, Georg Brunnhofer, Markus Bainschab, Paul Maierhofer, Anton Buchberger, Stefan Cesnik, Benjamin Lang and Markus Knoll for the valuable discussions during endless coffee breaks and activities outside work. Particularly I would like to thank Benjamin Lang for sharing his never ending scientific knowledge with me and Mario Schriefl for encouraging me to try QEPAS with soot.

I have had the pleasure of working with Prof. Simone Hochgreb and Robert Nishida from the University of Cambridge, who I thank for sharing ideas and critical discussions.

I also want to thank Julia Schönfelder and Esther Schennach for their administrative work, and Sitaram Stepponat for his technical support.

I also want to thank my parents and my family for their support. I want to particularly thank my girlfriend Christine for her love, and her patience and encouragement during my thesis. I also want to thank our son Benedikt for his contagious cheerfulness.

Abstract

Air pollution is one of the biggest challenges of our time. In addition to its adverse health effects millions of premature deaths are linked to air pollution. Apart from adverse health impacts and mortality, air pollution causes huge economic costs.

At present, air pollution monitoring is carried out at low spatial resolution due to high costs coming along with high accurate measurement equipment. However, to enact mitigation actions, such as temporary speed limits and pollution dependent city tolls, possibilities to monitor air quality at high spatial and temporal resolution are necessary. Such possibilities are also necessary to perform research on the spatial patterns and dispersion of pollutants, as well as to perform cohort studies to better understand the health impacts and mortality caused by air pollution.

A possible solution to monitor air quality at high spatiotemporal resolution is the development of dense sensor networks equipped with air-quality sensors. Sensor network technologies are available. However, the lack of sufficiently accurate, low-drift and reliable low-cost sensors is identified as the main bottleneck for establishing such sensor networks within a review in this thesis.

As the best candidate for a reliable sensing concept, optothermoacoustic sensors were selected. Optothermoacoustic methods are a branch of optical spectroscopy, which offer an indirect method to measure light absorption. One of the advantages of these methods is the linear relationship between analyte concentration and the induced signal amplitude. An excitation light source is chosen such that it is absorbed by the analyte. Since the excitation light source is modulated at a certain frequency, absorption and excitation of the analyte molecules is followed by subsequent relaxation, which produces changes of the (i) pressure, (ii) temperature, and (iii) via temperature the density of the gas mixture. Photoacoustic as well as its subbranch quartz-enhanced photoacoustic spectroscopy (QEPAS) detect the pressure change. QEPAS uses a piezoelectric quartz tuning fork (QTF) to measure the pressure wave. Photothermal interferometry (PTI) mainly detects the change of temperature due to an induced refractive index change.

This work describes the development and characterization of two sensing concepts for the measurement of NO_2, one QEPAS-based and one PTI-based. Both sensing concepts are characterized with reference concentrations of NO_2, and their long-term stability is studied. Due to the millimeter-sized QTF the QEPAS-based sensing concept bears excellent miniaturization potential. Commonly, micro-resonators are used to additionally amplify the QEPAS signal, which makes them difficult to operate in changing environmental conditions. In contrast, the presented bare fork QEPAS setup is more robust and easily adopted by the use of a low-cost temperature and humidity sensor. A noise analysis is performed. The detection limit is shown to be close to the theoretically achievable. The minimum achievable noise equivalent concentration is determined to 21 ppb NO_2 for 120 s measurement time, which is sufficient to detect the exceedance of air quality limit values.

The PTI-based sensing concept is realized by means of a fiber-coupled Fabry–Pérot interferometer. Due to the rigid structure of the interferometer, the interferometer is robust against mechanical vibrations, which is also verified experimentally. The minimum achievable noise equivalent concentration is determined to 26 ppb NO_2 for 100 s measurement time. Theoretical investigations show that the detection limit could be further improved by a different laser beam alignment or by using mirrors with higher reflectivity for the interferometer, without the need of increasing the power of the excitation laser. Due to the small size of the interferometer, chip-level miniaturization of the sensing concept is possible.

Finally, the measurement of black carbon in the form of soot is demonstrated with a QEPAS sensing concept. To the best of the author's knowledge, this thesis describes the first demonstration for the detection of soot by QEPAS. Although the detection limit of $\approx 25\,\mu\mathrm{g\,m^{-3}}$ (19 s measurement time) is yet only sufficient for air quality monitoring in highly poluted areas, optimized electronics and higher excitation laser powers would enable small-footprint, low-cost black-carbon sensing.

Articles included in this thesis

Paper 1. Breitegger P. and Bergmann A. (2016). Air quality and health effects — How can wireless sensor networks contribute? A critical review. In *2016 International Conference on Broadband Communications for Next Generation Networks and Multimedia Applications (CoBCom)*.

Paper 2. Breitegger P. and Bergmann A. (2018). A Precise Gas Diluter Based on Binary Weighted Critical Flows to Create NO2 Concentrations. *Proceedings*, 2(13):998.

Paper 3. Breitegger P., Lang B. and Bergmann A. (2019). Intensity Modulated Photothermal Measurements of NO2 with a Compact Fiber-Coupled Fabry–Pérot Interferometer. *Sensors*, 19(15):3341.

Paper 4. Breitegger P., Schweighofer B., Wegleiter H., Knoll M., Lang B. and Bergmann A. (in press). Towards Low-Cost QEPAS Sensors for Nitrogen Dioxide Detection. *Photoacoustics*.

Paper 5. Breitegger P., Schriefl M. A., Nishida R. T., Hochgreb S. and Bergmann A. (2019). Soot Mass Concentration Sensor using Quartz-Enhanced Photoacoustic Spectroscopy. *Aerosol Science and Technology*, 53(9):971–975.

Table of contents

Nomenclature

Acronyms / Abbreviations

AM	Amplitude modulation
AQ	Air quality
BAM	Beta attenuation monitor
BC	Black Carbon
CAPS	Cavity-attenuation phase-shift spectroscopy
CAQI	Common air quality index
CAST	Combustion Aerosol Standard
CEN	European Committee for Standardization
CEPAS	Cantilever-enhanced photoacoustic spectroscopy
CLD	Chemiluminescence detector
CO_2	Carbon dioxide
CO	Carbon monoxide
CPC	Condensation Particle Counter
CRDS	Cavity-ring-down-spectroscopy
DC	Diffusion charger
DFB	Distributed feedback laser
DOAS	Differential optical absorption spectroscopy

DR	Dilution Ratio
EC	Electrochemical
E-MOCAM	Electrical modulation cancellation method
EU	European Union
FPI	Fabry–Pérot interferometer
FWHM	Full width at half maximum
ICAD	Iterative cavity-enhanced differential optical absorption spectroscopy
ICL	Interband cascade laser
LED	Light emitting diode
LIA	Lock-in amplifier
LOD	Limit of detection
MEMS	Microelectromechanical system
MFC	Mass Flow Controller
MFM	Mass Flow Meter
MIR	Mid infrared
MOX	Metal oxide
MSS	Micro Soot Sensor; by AVL List GmbH
NIR	Near infrared
NO	Nitrogen monoxide
NO_2	Nitrogen dioxide
NO_x	Nitrogen oxides
H_2O	Water
O_3	Ozone
OPC	Optical particle counter

OPO	Optical parametric oscillator
PA	Photoacoustic
PAS	Photoacoustic spectroscopy
PAX	Photoacoustic Extinctometer; by Droplet Technologies
PM_{10}	PM fraction with an aerodynamic particle diameter of less than 10 µm
$PM_{2.5}$	PM fraction with an aerodynamic particle diameter of less than 2.5 µm
PM	Particulate Matter
PN	Particle number concentration
PTI	Photothermal interferometry
QCL	Quantum cascade laser
QEPAS	Quartz-enhanced photoacoustic spectroscopy
QTF	Quartz tuning fork
SMPS	Scanning Mobility Particle Sizer
UFP	Ultrafine Particles, PM fraction with an aerodynamic particle diameter of less than 100 nm
U.S. EPA	United States Environmental Protection Agency
UV	Ultra violet
WM	Wavelength modulation

Chapter 1

Introduction

1.1 Motivation

In 2015 air pollution caused 6.4 million premature deaths worldwide. While household air pollution is decreasing (2.8 million deaths in 2015), ambient air pollution (4.2 million deaths in 2015) is predicted to cause between 6 and 9 million deaths in 2060 if air pollution is not sufficiently controlled [57].

Apart from premature deaths, air pollution decreases the quality of life by causing, e.g. cardiovascular and respiratory diseases [118]. Also, health impacts caused by air pollution result in economic damage. The yearly costs of air pollution's health impacts are estimated to be EUR 330 billion to 940 billion in the EU in 2010 [2]. Further, people of lower socio-economic status, elderly, children and people in poor health are more negatively affected by the adverse effects of air pollution [32].

According to the European Environment Agency, the main air pollutants affecting the human health are particulate matter (PM), ozone (O_3) and nitrogen dioxide (NO_2) [31]. Amongst other pollutants, these three have to be monitored in zones or agglomerations either exceeding 250,000 inhabitants or of a specified population density within the EU [33, 79]. Due to the high cost of the measurement equipment, the number of measurement stations per area is very low. E.g., Graz has approximately one measurement station per $16\,\mathrm{km}^2$. On the other hand, pollutant concentrations may vary on scales below $100\,\mathrm{m}$ [130, 7].

Therefore, possibilities to monitor air quality at high spatial resolution are of high interest to better understand air pollution, assess the impact of air quality improvement measures, and help citizens monitor their individual exposure. This requires a much denser sensor network of low-cost but reliable sensors, which is able to monitor air pollution values directly.

In this work, sensing concepts based on optothermoacoustic methods for the measurement of

NO_2 and black carbon are developed and characterized. The developed sensing concepts are capable of miniaturization and low-cost production, if mass-produced.

1.2 Air quality monitoring

Limit values for pollutants are based on experimental animal, controlled human clinical and epidemiological studies. Especially in the latter, it can be difficult to map down isolated effects of single pollutants, as usually multiple pollutants are present at the same time. Therefore, different institutions or organizations may come to different conclusions on limit values. In the EU, the legislation for limit values and measurement techniques are described in the 2008/50/EG [33] und 2015/1480/EC [79] directive. The limit values for NO_2 are similar in WHO and EU (cf. Table 1.1). Short-term NO_2 levels above $200\,\mu g\,m^{-3}$ have indicated effects, whereas $500\,\mu g\,m^{-3}$ show acute health effects [118].

Table 1.1 Limit values for NO_2 and PM2.5 according to the EU and WHO. $1\,\mu g\,m^{-3}$ NO_2 is equal to 0.522 93 ppb.

Pollutant	**Averaging period**	**EU Ambient Air Quality Directives**	**WHO air quality guidelines**
NO_2	1 day	$200\,\mu g\,m^{-3}$ (not to be exceeded more than 18 days per year)	$200\,\mu g\,m^{-3}$
	C. year	$40\,\mu g\,m^{-3}$	$40\,\mu g\,m^{-3}$
$PM_{2.5}$	1 day	-	$25\,\mu g\,m^{-3}$
	C. year	$25\,\mu g\,m^{-3}$	$10\,\mu g\,m^{-3}$

The mass concentration of particulate matter in the ambient must be monitored for particles with aerodynamic diameters smaller than 10 µm (PM_{10}) and smaller than 2.5 µm ($PM_{2.5}$) [1]. However, since the volume scales cubic with size, this metric essentially measures large particles. On the other hand, studies suggest, that especially ultrafine particles (UFP; smaller than 100 nm) should be regulated [78]. Compared to larger particles, they are more biologically active and can therefore cause severe adverse health effects (e.g. inflammatory activity, reduced lung function, cardiovascular changes, lung cancer) [107]. Due to their small size, they can enter blood and lymph circulation. Black carbon (BC) which is produced from combustion, typically has a mean diameter between 40 and 80 nm. It "is possibly carcinogenic to humans (Group 2B) based on sufficient evidence in experimental animals and

---

[1] Actually, a size selective inlet is used with 50 % cut-off at an aerodynamic diameter of 10 µm or 2.5 µm, respectively [114].

inadequate evidence from epidemiological studies" according to the International Agency for Research on Cancer [55]. To date, no air quality limit values regarding BC have been published. Therefore, the limit values and air quality indices for $PM_{2.5}$ are shown in Table 1.1 and Table 1.2, respectively. To inform citizens on air quality, a common air quality index (CAQI) was established which ranges from 0 (very low pollution) to 100 (very high pollution). The CAQI for NO_2 and $PM_{2.5}$ is depicted in Table 1.2.

Table 1.2 Common air quality index for NO_2 and $PM_{2.5}$ (same values for roadside and background measurements) [110]. $1\,\mu g\,m^{-3}$ NO_2 is equal to 0.522 93 ppb.

Index class	**NO_2** ($\mu g\,m^{-3}$)	**$PM_{2.5}$** ($\mu g\,m^{-3}$)	
	1 hour	1 hour	24 hours
Very high (>100)	>400	>110	>60
High (75-100)	200-400	55-110	30-60
Medium (50-75)	100-200	30-55	20-30
Low (25-50)	50-100	15-30	10-20
Very low (0-25)	0-50	0-15	0-10

1.2.1 A selection of commercial instruments to measure ambient pollutants

The following section shows a selection of commercial instruments and low-cost sensors to measure ambient concentrations of NO_2 and PM. The reference methods are regulated in EN14211 (NO_2) and EN 12341 (PM) and equivalent methods may be qualified. Exhaustive reviews for PM sensors may be found elsewhere [38, 5].

NO_2

Chemiluminescence Detector

Chemiluminescence detectors (CLD) are the reference method for the measurement of nitrogen oxides NO_X, NO and NO_2 according to EN14211. A schematic drawing is depicted in Figure 1.1. NO reacts with O_3 to form excited NO_2, which de-excites radiatively. The produced light is proportional to the number of NO molecules in the measurement chamber. A light detector is used to measure the produced light [114].

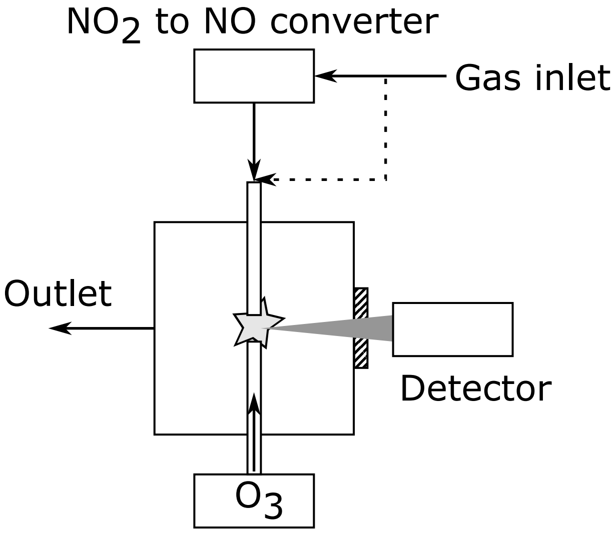

Fig. 1.1 Scheme of a chemiluminescence detector. The air sample enters the reaction chamber directly or via an NO_2 converter. Ozone and NO react. The produced light is measured by means of a detector.

To be able to also measure NO_2, NO_2 can be converted to NO and oxygen by using a catalyzer (typically made from molybdenum) which has to be heated to temperatures exceeding 300 °C. The CLD then measures the total amount of NO and NO_2 molecules. By subtracting the concentration of NO from the concentration of NO_X, the concentration of NO_2 can be determined [114].

A typical lower detectable limit is 0.12 ppb with an upper range selectable between 5 ppm and 25 ppm (ECO Physics, Model: nCLD 82 S).

Cavity-ring-down-spectroscopy

In cavity-ring-down-spectroscopy (CRDS), an absorption cell which is comprised of two highly reflecting mirrors (M_1 and M_2 in Figure 1.2) is used to mimic long absorption path lengths.

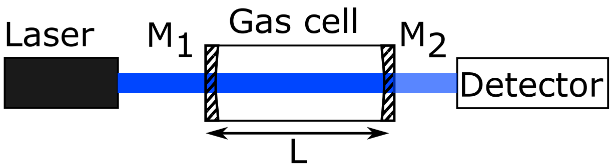

Fig. 1.2 Scheme of a cavity-ring-down-spectroscopy setup. Absorption cell is comprised of mirrors M_1 and M_2. The laser pulse is attenuated by multiple absorptions of NO_2, which is measured with a detector.

Intensity modulated light, with a wavelength which is well absorbed by NO_2 (e.g. 450 nm for Teledyne T500U) is coupled into the absorption cell. A detector at the back of the cell measures the transmitted intensity. Due to the long optical path length in the absorption cell, the transmitted intensity $I(t)$ follows an exponential decay, once the light source is switched off:

$$I(t) = I_0 \cdot e^{-\frac{-t}{\tau_0}}. \tag{1.1}$$

Here, I_0 is the intensity which is coupled in and τ_0 the decay constant. NO_2, with an absorption coefficient α of concentration C, which is present in the cell of length L, changes I_0 to I_0' due to absorption, described by the law of Beer-Lambert:

$$I_0' = I_0 \cdot e^{-\alpha \cdot C \cdot L}. \tag{1.2}$$

The change in I_0 leads to a change in τ_0 which can be determined by analyzing the temporal evolution of the transmitted intensity $I(t)$ [114]. Cavity-attenuation phase-shift spectroscopy (CAPS) is a special form of cavity-ring-down-spectroscopy (CRDS), where the change of τ_0 is measured to determine the concentration of NO_2 [114].

The lower detectable limit is better than 40 ppt (Teledyne, model: T500U CAPS NO_2

Analyzer). According to Teledyne the T500U is an equivalent method for the measurement of NO_2 in accordance with EN14211.

Iterative cavity enhanced differential optical absorption spectroscopy

In differential optical absorption spectroscopy (DOAS) the spectral absorption features of trace gases in a certain wavelength range are measured and compared to reference spectra. Due to the uniqueness of their structure, even spectrally overlapping analytes can be separated and the concentration can be determined. The iterative cavity enhanced DOAS (ICAD) instrument by Airyx uses an LED, emitting in the range between 430 and 465 nm for the measurement of NO_2 concentrations by active DOAS in a multipath cell (cf. Figure 1.3) [3]. According to Horbanski et al. [43], strong absorbers and scatterers decrease the effective length of the light path in the multipath cell. Therefore, an iterative algorithm is used for correction of the light path length, to correctly determine the concentration. This allows to evaluate the measured optical density $D_{meas}(\lambda) = \ln(I_0(\lambda)/I(\lambda))$, with $I_0(\lambda)$ the intensity measured with zero gas and $I(\lambda)$ the intensity measured with NO_2 being present. Thus, the measurement is independent of long-term fluctuations of the LED. To measure $I_0(\lambda)$, the cell is flushed with zero air once an hour [43].

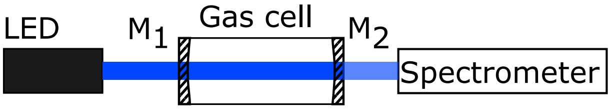

Fig. 1.3 Scheme of a cavity enhanced differential optical absorption spectroscopy setup. The absorption cell is comprised of mirrors M_1 and M_2. NO_2 absorbs portions of the light emitted by the LED, which is measured by a spectrometer to calculate the concentration of NO_2.

The lower detection limit for 2 s integration time is 300 ppt (Airyx, model: ICAD) for the measurement of NO_2 [3]. By using an NO to NO_2 converter, the concentration of NO_X can be measured in a second cell. Compared to a CLD, this method is more robust and has minimal long-term drift (less than 0.1 ppb per month).

Electrochemical sensors

Electrochemical (EC) sensors exist for a large range of gases. A scheme of an EC sensor is shown in Figure 1.4. EC sensors for NO_2 have an opening for gas exchange, which is covered by a membrane, which is, ideally, only permeable for NO_2. A chemical reaction at the measurement electrode leads to the release of electrons. A counter electrode balances the reaction, while ions are exchanged via an electrolyte. A measurable current is produced, which is directly proportional to the concentration of NO_2 [114]. As the membrane is also permeable to other gas molecules, these contribute to the current as well. Cross-sensitivities to gases such as O_3, H_2S and NO are reported (Alphasense, model: NO2-A43F), where the cross-sensitivity to O_3 is around 100 % [69]. The NO2-A43F has a noise equivalent concentration of 15 ppb.

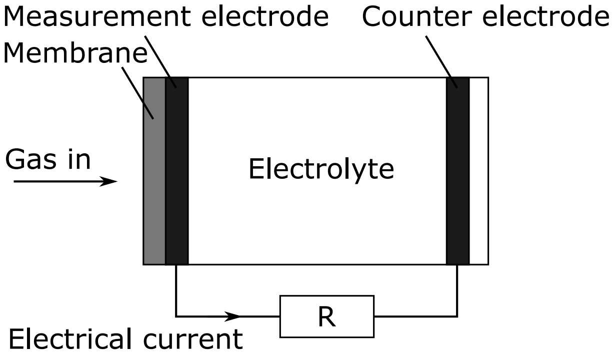

Fig. 1.4 Scheme of an electrochemical sensor. The air sample enters the EC sensor via diffusion through a membrane. A chemical reaction at the measurement electrode results in an electrical current between the two electrodes.

Due to their cross-sensitivity to other gases, long-term drift and dependency on parameters such as humidity and temperature [20, 70] these sensors are not intended to replace the above mentioned sensors for stationary air pollution measurements according to the national air quality directives. Their small footprint (approximately 20 mm diameter and 17 mm height for Alphasense, model NO2-A43F), low cost and low energy consumption, however, are often convincing arguments to use them in sensor network approaches [69, 60, 21, 8, 41]. At the moment, however, even laboratory pre-calibration is insufficient for obtaining sufficient results under real-world conditions [20].

Metal oxide sensors

Metal oxide (MOX) sensors consist of a metal oxide semiconducting material (typically SnO_2 or ZnO), which changes its resistance upon adsorption of oxidizing or reducing molecules. For a faster adsorption process and thus a better response time, these sensors are typically heated to 300 to 600 °C [114].

The physical and chemical processes are complex, but the change of the resistance $R_S(c)$ with respect to a concentration c can be described by two empirical constants, α and β as

$$R_S(c) = \alpha \cdot c^{\beta}. \tag{1.3}$$

If the molecule to detect is oxidizing, such as NO_2 the resistance increases further. If the gas is reducing, such as CO, the resistance decreases. Thus, MOX sensors do not offer selectivity, as many gases interact with the surface.

To the best of the author's knowledge, only one commercial metal oxide (MOX) sensor exists that is deticated for the detection of NO_2 (SGX Sensortech, model: MICS-2714). MOX sensors are even smaller than EC sensors (MICS-2714: $5\,\mathrm{mm} \times 7\,\mathrm{mm} \times 1.55\,\mathrm{mm}$) and also cost less (approximately $1/10$ of EC sensors). The lower detection limit is worse than for EC sensor (MICS-2714: 50 ppb) and so is the longer-term drift (6 months) [66]. Also, the resistance depends on temperature and humidity.

Particulate Matter

Filter-based measurement

The reference method for the sampling and measurement of $PM_{2.5}$ as well as PM_{10} is a gravimetric measurement method (EN 12341). A size selection is usually carried out by continuous suction of the air sample through an impactor (deposition by mass inertia and orifices of different flow velocities) or cyclone (deposition by inertia by centrifugal force) inlet [38].

The sample is collected on a pre-weighed filter. After a certain amount of time (typically 24 h) the filter is removed and sealed. The loaded filter is then heated and weighed. As the filter is loaded by a constant volumetric flow rate, the mass concentration in $\mu\mathrm{g\,m}^{-3}$ can be determined. Samplers, which automatically change the filters exist, to reduce the necessity for manual, daily filter exchange [114]. For a precise measurement, filters must be packed under controlled conditions of humidity and temperature. Care must be taken about filter conditioning, charged particles and filter handling [38]. Particle loss of soot due to wrong filter handling can be on the order of 20 µg [38]. Typical volumetric flow rates are in the range of 1 and $2.3\,\mathrm{m}^3\,\mathrm{h}^{-1}$.

Beta attenuation monitors

Beta attenuation monitors (BAM) measure the attenuation of beta rays through a filter before and after particles are deposited. The mass concentration is determined due to a defined volumetric mass flow, which loads the filter [114]. As the filter is realized as a filter belt, quasi-continuos monitoring down to 1 min averages is possible (ET enviro, model: E-BAM). The attenuation of the beta rays (E-BAM: C_{14} β^- emitter) can e.g. be measured with a scintilation probe (E-BAM).

The measurement range is on the order of 0 to $65\,\mathrm{mg\,m}^{-3}$ with an accuracy of $2.5\,\mu\mathrm{g\,m}^{-3}$ or 10 % in 24 h (E-BAM).

Photoacoustic sensors

To the best knowledge of the author, two commercial photoacoustic sensors for the mea-

surement of carbonaceous particles exist: The Photoacoustic Extinctometer (PAX; Droplet Technologies) and the Micro Soot Sensor (MSS; AVL List GmbH).
As the focus of this thesis was photoacoustic spectroscopy, a more extensive review of existing instruments, theoretical considerations, as well as experimental results will be covered more extensively in chapters 2, 3 and 4.

Other sensing principles
A common type for low-cost sensing of PM is the optical particle counter (OPC), which measures the light scattered by a particle. Differently sized particles produce different scattering curves, described by the Mie-theory. Usually the photodiode is placed 90° from the light source, where the measured intensity scales with particle size in a certain size range. Due to the sensor principle, such sensors can only measure sizes down to 350 nm [4].
Diffusion chargers can be used to measure particle numbers [97], rather than particle mass. Particle number legislation, however, has not yet found its way into ambient air quality measurements.

1.2.2 Sensor networks for AQ monitoring

In **Paper 1** a review of sensor networks for air quality (AQ) monitoring was performed. Possible applications and services that could be provided by such sensor networks were investigated. A list of possible applications for sensor networks with air quality sensors is shown below, where the requirements on the sensor accuracy are increasing from (a) to (l). Details can be found in **Paper 1**.

(a) Participative sensing, i.e. users measure air pollution and upload the measurements to the cloud
(b) Personal exposure
(c) Concentration maps for cities and agglomerations
(d) Mitigation actions, such as traffic control; to enforce different strategies based on pollutant levels and other variables
(e) Real-time AQ maps
(f) Real-time AQ alerts
(g) Pollution-poor route smartphone app for pedestrians and cyclists
(h) Cohort studies
(i) Research in spatial patterns and dispersion of pollutants

(j) Research on the influence of external variables, e.g. UV radiation or wind, on air pollution

(k) Remote sensing, i.e. real driving emissions from cars, on the road

(l) Accurate point measurements in accordance with 2008/50/EG and 2015/1480/EC

A selection of projects and an overview of the sensor technologies used is given in Table 1.3. With respect to the NO_2 sensors, EC or MOX sensors were used. However, in a study where the performance of low-cost sensors was tested, EC sensors for NO_2 showed bad agreement with reference equipment, when co-located under real-world conditions with large inter-device differences and strong cross-interferences to other gases, dependency on environmental conditions, and dependence on the location [20]. In addition, long-term drift is another problem with EC sensors [70]. As previously mentioned, MOX sensors perform worse than EC sensors.

Therefore, sensor readings by EC and MOX sensors can only give approximate values and they are only feasible for indicative applications and to raise awareness such as applications (a) and (b). Concentration maps (application (c)) might only be available after extensive post-processing with other predictor variables, such as car counts and temporal averaging such as in OpenSense [77].

Table 1.3 Projects reviewed in **Paper 1** and sensor technologies used.

Project name	NO_2 sensor	PM sensor	Reference
RESCATAME	MOX	pressumably low-cost optical particle counter	[42]
CamMobSens	EC	-	[69]
CITI-SENSE	EC (AQMESH)	OPC (AQMESH)	[8]
OpenSense	EC	diffusion charger	[41]

Traffic control (application (d)) based on AQ measurements by low-cost sensors was tried in RESCATAME, but actions and outcomes of the project lack behind the project goal. The only action to improve air quality was the temporary closing of a street by local police officers [42]. It appears that already in close proximity to roads, where one would expect high pollution levels, present low-cost sensors can not sufficiently discriminate between pollution levels.

Also applications (e) to (l) can not be realized with commercially available low-cost sensors. Application (l), regulatory monitoring, is virtually impossible to achieve for any low-cost sensor, without a proper gas conditioning system and periodic re-calibration, which would contradict the term low-cost (measurement devices for legislative measurements are typically 5,000 to 30,000 EUR [20]). Application (k), remote sensing, would also be difficult to implement at low cost, since a proper conditioning system and temporal resolution are necessary to measure the exhaust of passing cars. However, it is expected that applications (a) to (j) would be feasible with a low-cost sensor technology with performance characteristics between present low-cost and highly accurate devices.

Suggested performance goals for specific applications are e.g. given by the US Environmental Protection Agency [115]. Also, it is worth noting, that the European Committee for Standardization (CEN/TC264/WG42) is currently working on a technical specification for testing procedures for the performance evaluation for low-cost sensors that are intended to monitor gaseous pollutants in ambient air. A first draft is expected for the first quarter of 2020.

Another important point is the spatial resolution that the installation of multiple sensors can provide and that is necessary for a specific application. Literature shows that the spatial resolution in proximity to roads should be higher. E.g., a measurement setup to measure fine and ultra fine particles (with condensation particle counter and scanning mobility particle sizer) is reported, where a significant drop in particle concentration and a change in size distribution was seen at the measurement points, placed 17, 20, 30, 90, 150, and 300 m away from a road [130]. Apte et al. [7] produced maps of 30 m spatial resolution, by collecting data with lab grade instruments, mounted in a Google street view vehicle. PM was measured with PAS, NO with a CLD and NO_2 with CAPS.

1.3 Problem statement and scope

At the moment air quality is only monitored at low spatial resolution. This is due to high cost of the high accurate measurement equipment such as CLD, CRDS, or BAM. However, denser networks offering better spatiotemporal resolution are necessary to enact mitigation actions, perform research on pollutants, and better understand the health impacts and mortality caused by air pollution to name a few of the applications defined in the previous section.

Such dense sensor networks require sufficiently accurate low-cost sensors. Regarding the measurement of NO_2, MOX and EC sensors are available at low cost, which, however suffer from cross-interference to other gases, drift and dependence on ambient conditions [20, 66]. Regarding the measurement of PM, air quality legislation currently regulates $PM_{2.5}$ and PM_{10}. However, due to the adverse health effects of UFPs [78] and particularly BC [55], a low-cost sensor capable of measuring the BC concentration would be of high interest.

This thesis aims at developing and characterizing sensing technologies, which are capable of monitoring relevant air pollutants at high spatial and temporal resolution. It should close the gap between present low-cost sensors and highly accurate measurement devices. For that purpose, the sensor should be able to be manufactured at low cost, have small size but at the same time yield sufficient accuracy to reliably determine the CAQI, have long-term stability as well as not have cross-sensitivity to other pollutants or changing environmental conditions.

Optical methods offer a low detection limit, good dynamic range, long-term stability and insensitivity to other gases (upon a proper selection of the wavelength). Photoacoustic (optocaoustic) and photothermal (optothermal) methods additionally have the advantage of a linear signal dependency on the concentration and high dynamic range. Of those, quartz-enhanced photoacoustic spectroscopy (QEPAS) and photothermal interferometry (PTI) offer the best miniaturization potential and were thus further investigated. Apart from the above mentioned advantages, an optothermoacoustic detector can be used to monitor multiple analytes – only the light source has to be changed, such that its wavelength matches the absorption spectrum of the targeted analyte.

This work describes the detection of NO_2 and BC with optothermoacoustic methods, but the detection of other pollutants is mainly a question of available laser sources. Further, more than one laser can be used in a single instrument to excite an optothermoacoustic wave and hence a multi-pollutant instrument could be built.

A QEPAS-based and a PTI-based sensing concept for the measurement of NO_2 are described, developed and characterized. Both sensing concepts are characterized with reference concentrations of NO_2, and their long-term stablity is studied.

The QEPAS-based sensing concept which uses a bare fork configuration with acoustic filters is characterized over varying temperature and humidity. A noise analysis is performed and comparison to a theoretical model are carried out.

A novel PTI-based sensing concept is realized by means of a fiber-coupled Fabry–Pérot interferometer. The sensitivity to mechanical vibrations is investigated by using an electrodynamic shaker. A simple theoretical model is conducted to give advice for further improvement of the interferometer.

Finally, the measurement of BC in the form of soot is demonstrated with a QEPAS sensing concept. To the best of the author's knowledge, it is the first demonstration for the detection of soot by QEPAS.

1.4 Organization of this thesis with respect to the related articles

In the course of the thesis a number of papers were published, which also describe the efforts towards the development of the sensor concepts. First, state-of-the-art pollution monitoring was investigated and previous projects on sensor networks and air pollution monitoring were reviewed (**Paper 1**). This is brievly summarized in Section 1.2.2. Chapter 2 gives an overview over photoacoustic spectroscopy (PAS), quartz-enhanced photoacoustic spectroscopy (QEPAS) and photothermal interferometry (PTI). Since the work on QEPAS was the largest part of this thesis, the review of QEPAS methods takes the most room in that chapter and also contains a detailed investigation of a theoretical QEPAS model. Chapter 3 summarizes the work on the PTI- (**Paper 3**) and QEPAS- (**Paper 4**) sensing concepts for the measurement of NO_2. For the characterization of gas sensors a gas diluter was developed (**Paper 2**). Chapter 4 summarizes the work on the QEPAS sensing concept for black carbon (**Paper 5**). Finally, Chapter 5 concludes the work and gives an outlook future developments.

Chapter 2

Photoacoustic and photothermal spectroscopy

Photoacoustic spectroscopy (PAS) is an indirect method to measure light absorption by the generation of sound. The photoacoustic effect was discovered in 1880 by Alexander Graham Bell, who used modulated light to transmit audio [12]. His invention, the photophone, used a thin mirror to modulate light, which was transmitted to the receiver, where it was focused onto a light absorbing solid. The light absorbing solid made it possible to hear the audio from the sender. Bell also found, that the effect worked well with gases [12].

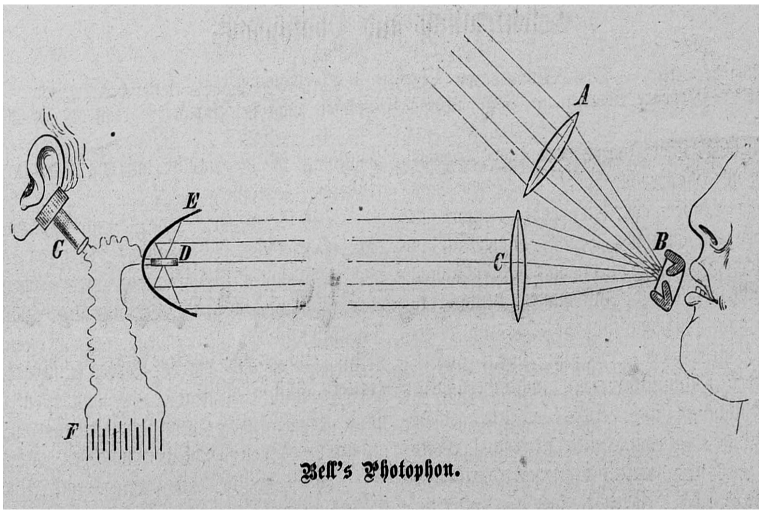

Fig. 2.1 Schematic of the photophone. Light gets focused (A) onto a thin mirror (B), which vibrates with the frequency of the talking person. The modulated light is collimated (C) and focused (E) onto a light absorbing solid (D), which by its opto-electricity drives a loudspeaker (G). Public domain.

Nevertheless, it took until 1938 when M.L. Viengerov (as cited by Bialkowski et al. [12]) utilized the photoacoustic effect to study light absorption by gases. Photothermal interferometry (PTI) for the study of gases was first reported in 1968 [67]. The mass concentration measurement of Diesel soot by photoacoustic spectroscopy was reported first in 1979 [34]. While conventional photoacoustic spectroscopy uses a microphone and an acoustic resonator to amplify and measure the acoustic wave, Kosterev et al. [51] presented the method of quartz-enhanced photoacoustic spectroscopy (QEPAS) for gas measurements, which uses a piezoelectric quartz tuning fork (QTF) as mechanical resonator and transducer for the photoacoustic signal. In contrast to conventional PAS, the cell volume can be extremely small ($< 1\,\mathrm{cm}^3$). To the best of the author's knowledge, **Paper 5** is the first demonstration for the detection of soot by QEPAS. One of the features of these methods is the linear relationship between analyte concentration and acoustic amplitude [16, 82, 23].
The processes involved in opto-thermoacoustic spectroscopy, as they were used in this thesis, are shown in Figure 2.2. For gas measurements, a light source is chosen such that its emission wavelength(s) matches one ore more absorption lines of the analyte, which ideally does not interfere with other analytes in the gas mixture.

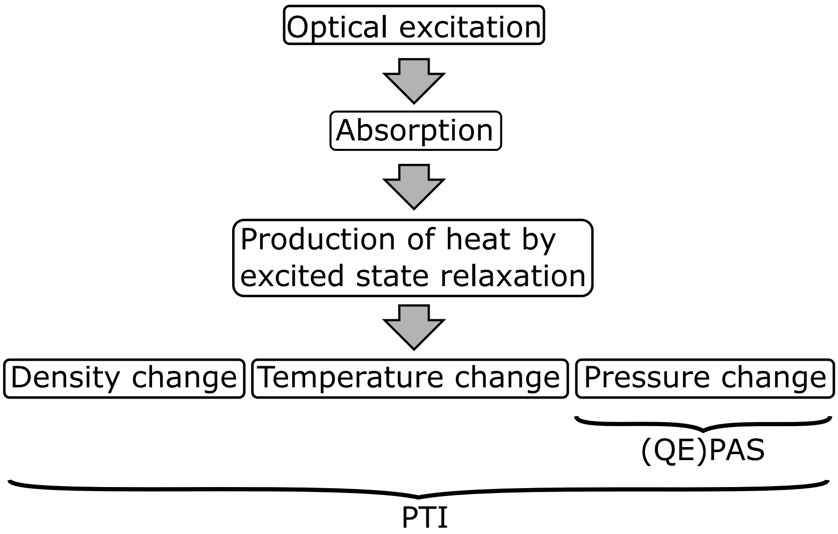

Fig. 2.2 Processes involved in the production of the photoacoustic and photothermal signal. Redrawn from Bialkowski et al. [12]

The light source is modulated at a frequency f, which leads to absorption and excitation of the analyte molecules, which subsequently relax by different mechanisms. The mechanism of collisional relaxation and translational energy transfer (for sufficiently short relaxation times), periodically produces heat (at frequency f). This periodic heat production periodically changes the (i) pressure, (ii) temperature, and (iii) via temperature the density of the gas mixture. The thermal wave is usually heavily damped and only visible in the sub-millimeter range [71], whereas the acoustic wave is only weakly damped. In PAS, only the pressure change is detected, as the microphone is usually placed some millimeters away. In contrast, a combination of both is measured in PTI, where a probe beam detects the induced refractive index change.

2.1 State of the art

The following section gives an overview over detection schemes for the opto-thermoacoustic effect, including conventional PAS, QEPAS, and PTI with a modulated excitation beam and a Fabry–Pérot interferometer as used for this thesis. Due to the focus of this work on QEPAS, and the large number of recent advances in this technique, the section on QEPAS is the most extensive one. PTI on the other hand, might be based on other interferometer types as well, and is only one of the classes of photothermal spectroscopy, which uses a wide range of detection schemes, such as photothermal lensing [12]. A comprehensive in depth discussion of photothermal spectroscopy methods might be found elsewhere [12].

2.1.1 Detection schemes

Opto-thermoacoustic detection schemes, which use modulated light sources, are usually based on the scheme shown in Figure 2.3. A function generator is used to modulate an excitation light source, usually a laser, at frequency f by means of pulsed mode, amplitude (AM) or wavelength modulation (WM) [16, 82]. The excitation laser is directed into a gas cell containing the analyte (although called gas cell, it might also contain aerosol), which produces periodic changes in density, temperature and pressure. The signal of a transducer for one or more of these effects (e.g., microphone, QTF, interferometer) is fed into a two-phase lock-in amplifier (LIA). The LIA, a narrow-band bandpass filter, outputs the in-phase (I) and quadrature (Q) part of the opto-thermoacoustic signal with respect to the phase and frequency f of the function generator.

Background noise, e.g. due to absorption by contaminated windows or the cell walls causes a non-zero background signal which has the same frequency but a different phase than the useful signal [16]. To obtain the useful signal, proportional to the analyte concentration, the background signal must be subtracted vectorially from the measured signal, which is the reason a two-phase LIA has to be used.

As phase and magnitude of the background are not stable, regular background measurements must be carried out. Therefore, a gas-handling system must be used to switch between the gas stream for concentration measurements and the gas stream containing the background

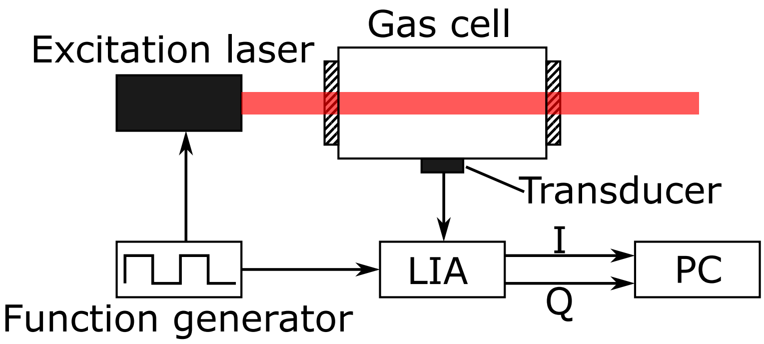

Fig. 2.3 General scheme for opto-thermoacoustic detection. LIA – lock-in amplifier, I and Q – in-phase and quadrature component of the opto-thermoacoustic signal.

only. The background stream might come from a gas cylinder containing the background mixture, or a gas stream where the analyte has been removed by means of a scrubber [16]. The selection of a suitable gas flow rate is a balance of response time and detection limit. The background noise may rise for flow rates exceeding 0.5 slpm ([16], **Paper 3**).
Up to a certain power of the excitation laser, the optothermoacoustic signal scales linearly with the analyte concentration c, described by a slope m. Thus, a detection limit (LOD) is often defined as a multiple n (usually n is 1, 2 or 3) of the standard deviation of the background noise σ divided by m as [16]

$$LOD_{n\sigma} = \frac{n \cdot \sigma}{m}. \tag{2.1}$$

With respect to the modulation frequency, it must be noted, that the signal in conventional PAS and PTI follows a $1/f$ frequency dependency, and therefore low modulation frequencies should be favored. However, ambient acoustic noise also follows a $1/f$ dependency and therefore modulation frequencies in the kHz range are preferred [16]. One exception is cantilever-enhanced photoacoustic spectroscopy (CEPAS), where the measurement cell is closed before the measurement, which shields it from ambient acoustic noise. On the other hand, if the modulation frequency is too high and the period of the modulation is comparable to the relaxation time from the excited state to the collisional deactivation, the produced signal might drop. This delayed molecular relaxation (which can also play a role for aerosols, Cf. Chapter 4) is described by the efficiency η as a function of relaxation time τ and the modulation frequency f_0 by: [16]

$$\eta = \frac{1}{\sqrt{1+(2\pi f_0 \tau)^2}} \tag{2.2}$$

While for AM a shutter or a laser with current modulation is sufficient, WM can require more complex setups and is only feasible for analytes with distinct absorption peaks. In WM setups the $2f$ component of the signal is used as useful signal, which offers better noise immunity than AM [51, 16] but to lock the laser wavelength to the absorption peak of the analyte, a complex $3f$ locking-technique can be necessary [82].

In contrast to gas molecules, which have distinct absorption peaks or ranges, soot exhibits a broad absorption (σ) in the visible to infrared range, which follows a power law of $\sigma \propto \lambda^{-\alpha}$ with respect to the wavelength λ [95]. Therefore, one is free to choose a wavelength, such that cross-interferences to absorbing gas molecules are minimized, usually in the near-infrared [94, 86, 74]. Owing to the broad absorption of soot, only AM modulation can be used.

Typically, lasers are used for opto-thermoacustic methods, due to their high power and narrow wavelength. Laser diodes cover the visible and near infrared (NIR) range from 380 nm up to above 2 µm. The mid infrared (MIR) region is of high interest in spectroscopy, since many molecules have distinct strong fundamental rovibrational transitions in the so called fingerprint region (6.7 to 25 µm) [101]. While photodetectors for this wavelength region need to be cooled, photoacoustic sensors can detect absorption at any desired wavelength, due to the production of the sound wave. In the MIR region, gas lasers (CO and CO_2), optical parametric oscillators (OPOs) and quantum cascade lasers (QCL) as well as interband cascade lasers (ICL) are available [29]. Distributed feedback (DFB) QCLs have high performance, while external cavity QCLs offer a higher tuning range. Tunable MIR-Lasers allow multicomponent detection of different gases with the same PAS setup, since certain gases have multiple fingerprints in a narrow region [125, 65]. Light emitting diodes (LED) can be preferred in some applications, as they offer a low-cost and robust alternative to lasers. Furthermore, LEDs are available for wavelength regions, where no laser sources are available. One example is Ref. [15], where UV-LEDs are used for Ozone-monitoring with QEPAS. As LEDs have a very broad wavelength spectrum, one is restricted to amplitude modulation.

2.1.2 Conventional photoacoustic spectroscopy

This chapter gives a short overview on conventional photoacoustic spectroscopy, where the photoacoustic signal is enhanced by an acoustic resonator. A more comprehensive review on photoacoustic spectroscopy was written by Bozóki et al. [16]. A review on photoacoustic resonators is given by Miklós et al. [71]. A brief summary of the theoretical concepts can be found in Chapter 2.2.1.

A scheme of a photoacoustic setup with a cylindrical resonator is shown in Figure 2.4. The gas sample is contained in the photoacoustic cell. A laser is modulated at frequency f_0, which is typically one of the resonance frequencies of the cylindrical resonator. Typically,

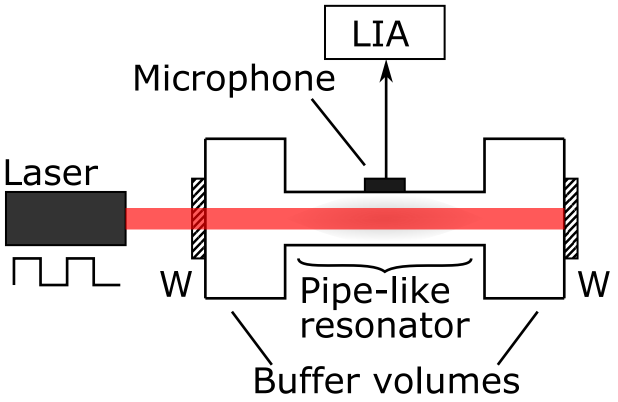

Fig. 2.4 Scheme for photoacoustic spectroscopy. The laser is modulated and enters the cell through a window (W). A window (W) at the back of the cell enables monitoring the laser power externally. The pipe-like resonator has two buffer volumes, to mimic an open-open resonator. The microphone is placed at the antinode of the longitudinal wave and the signal is fed into a LIA.

cylindrical resonators are operated at their first longitudinal mode, and the laser is directed through the resonator, such that it efficiently excites the corresponding mode. Two buffer volumes at the cylinder openings simulate an open end, such that pressure nodes are located at the resonator openings. The microphone, which records the photoacoustic signal is usually placed at the position of the pressure antinode and directed to the LIA.

Only in rare cases an acoustic resonator is omitted (e.g. some QEPAS variants, CEPAS and a low-cost implementation of PAS [cf. section 2.1.3]). Acoustic resonators offer an acoustic amplification by a quality factor (Q-factor) of around ten to eighty [16, 90, 124]. Except for the most commonly used type of organ-pipe resonators for longitudinal resonances, cylindrical resonators for the excitation of radial, azimutal modes (cf. [71]), T-cells [64, 47] and Helmholtz resonators ([71, 103, 87]) are reported in literature. Furthermore, differential variants of photoacoustic cells exist, where two identical resonators are used, but only the first resonator records the gas measurement and the second resonator is intended to record the background signal to be subtracted [87, 124].

2.1.3 Commercial photoacoustic sensors

multiSense

The french company mirsense offers a photoacoustic and QCL based spectrometer [19]. Using QCLs a wide variety of gases such as NO, NO_2, CO, CO_2, H_2O or NH_3 can be detected [72]. As the sensor is equipped with two QCLs, two gaseous components can be detected with one sensor. Owing to the fact that it is a commercial product no publications can be found on the PA cell. The cell is heated to 50 °C to avoid condensation effects. As an example, the detection limit for CO_2 is 100 ppb for an integration time of 1 s. The cell and the control electronics are each of size 100 mm × 70 mm × 30 mm and weight 200 g. [72]

CEPAS by Gasera

In the review paper by Bozóki et al. [16], it was noted that optical microphones could contribute substantially to PAS, due to their higher sensitivity as compared to conventional microphones without its availability at that time. To date the company Gasera, a spin-off from the University of Turku, offers commercial cantilever enhanced photoacoustic spectroscopy (CEPAS) products, relying on optical microphones based on microelectromechanical systems (MEMS) cantilevers. Instead of a microphone membrane, a silicon cantilever of thickness 10 µm, width 10 mm and length 5 mm is used (cf. Figure 2.5). The cantilever is fixed on one side and performs movements due to the photoacoustically induced pressure changes. The displacement of the cantilever is sensed by an interferometric readout system. A laser is focused on the side opposing the probe volume and the deflection of the laser beam, together with a non-deflected beam, results in an interferometric pattern. By this, the minimum detectable absorption of the pressure sensor was shown to be around 100 times better than that of an electret microphone-based differential PA cell [61]. One reason is, that the deflection of conventional microphones is greatest in the center of the membrane, but only its average deflection is measured. In case of the cantilever, however, the maximum deflection can be sensed (only bending, no stretching). Another reason is, that in contrast to a cantilever, the microphone membrane is damped due to stretching, which results in nonlinear response [109].

Figure 2.5 also shows a balance cell. Movement of the instrument would produce acceleration noise, which would disturb the cantilever. This is a particular problem, since CEPAS usually uses modulation frequencies below 100 Hz. Therefore, a balance cell is used to induce a pressure difference upon movement of the instrument, which compensates the movement of the cantilever [109].

Due to the optical microphone's high sensitivity, an acoustic resonator is not necessary and would also amplify noise at the same factor as it would amplify the useful signal [109]. Also, the optimum response of a cantilever is in the low Hz-range. [61] As a result, the sample volume can be very small (e.g. 30 mL for the PA201 by Gasera [37]. As a result of the $1/f$ dependency of environmental noise and the low modulation frequency of the Gasera cells, the probe volume always has to be closed before a measurement. With respect to applications which require continuos monitoring, such as environmental sensing, this might be a limiting factor.

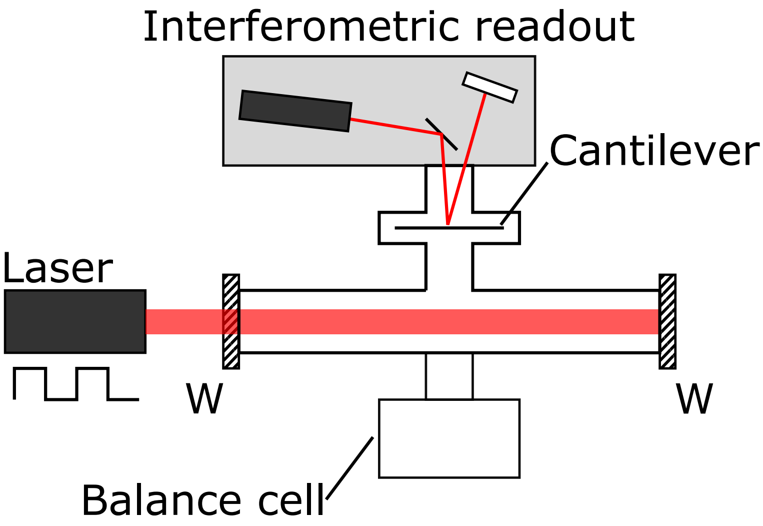

Fig. 2.5 Working principle of the PA201 Gasera CEPAS system. Redrawn from [48].

McNaghten et al. [68] reports multi-component detection using a Gasera cell. The combination of CO and CO_2, CO, C_2H_2 and CH_4 is realized by using four NIR tunable diode lasers. A possible combination of a Gasera cell with a tunable light source, such as an optical parametric oscillator (OPOs), is discussed as a possibility for multi-component air quality monitoring [48].

Nonresonant low-cost PA sensor for CO_2

Commercial low-cost sensors for the measurement of CO_2 are usually based on a conventional absorption cell. Low-cost photoacoustic based CO_2 sensors promise to deliver comparable performance at lower cost and size [100].

One such commercial photoacoustic device will soon be available by Infineon (PAS210) [45]. It is based on a broadband infrared light source, an optical filter for the CO_2 absorption lines around 4.2 µm and a nonresonant photoacoustic cell with a MEMS microphone and a diffusion port for air exchange. A similar product has also been announced by Sensirion (SCD40) [100]. The size of the SCD40 is 12 mm × 12 mm × 7 mm. An integrated temperature and humidity sensor is assumed to offer a compensation based on the two quantities, since temperature affects the photoacoustic signal and H_2O also absorbs in the 4.2 µm range.

A different sensing concept for a low-cost photoacoustic based gas sensor for CO_2 uses a nonresonant CO_2-filled photoacoustic cell as detector [44, 96]. A broadband light source shines through a sample volume before it excites the CO_2-molecules in the encapsulated cell. CO_2 molecules in the sample volume damp the light power, which can enter the encapsulated cell, resulting in a weaker signal amplitude. The design does not allow for low limits of detection (better than 50 ppm CO_2), but for low-cost and small devices. An introduction into the market is unclear at this point.

Photoacoustic aerosol sensors

To the best of the author's knowledge two commercial instruments are available for resonant photoacoustic measurement of aerosol absorption. The *Micro Soot Sensor* has been commercialized by AVL List GmbH and has great commercial success in the automotive industry [38]. The *PAX* by Droplet Measurement Technologies, Inc. has, e.g. been used as cloud particle spectrometer and for measuring atmospheric black carbon.

MSS The Micro Soot Sensor (MSS) uses a longitudinal resonator for the photoacoustic measurement of soot. The detection limit for 1 s averaging time is better than $10\,\mu g\,m^{-3}$ [10]. The MSS uses a twin cell design, to avoid pollution of the laser windows. It consists of a longitudinal resonator with buffer volumes with another non-resonant part added to the second buffer volume. The non-resonant part is used to let the sample flow enter from the left, while the sample flow also enters through the buffer volume on the right and exits from the middle (left buffer volume of the resonator). Furthermore, the aerosol enters the cell through ring channels, such that the sample enters the cell at low speed and without turbulence [10]. The longitudinal resonator has a resonance frequency of $\approx 4\,kHz$. The laser wavelength is $\approx 808\,nm$ and has less than 2 W of optical power. The flow rate is $\approx 2\,L\,min^{-1}$. The weight of the instrument is 26 kg and the size is approximately $40\,cm \times 48\,cm \times 56\,cm$.

PAX The Photoacoustic Exctinctometer (PAX) consists of a photoacoustic cell and a (reciprocal) nephelometer to simultaneously measure absorption and scattering (explaining the name of the product: extinction is the sum of both) [27]. The PAX offers three wavelength options (405 nm for brown carbon, 532 nm to mimic what the human eye sees, and 870 nm for black carbon (soot)). The dynamic range reaches from 1 Mm to 10.000 Mm for 60 s averaging time (for 870 nm, where $1\,Mm \approx 0.16\,\mu g\,m^{-3}$ [40]). No publications on the working principle or performance can be found. It is, however, expected that a full wavelength plane wave longitudinal resonator such as the one described by Moosmüller et al. [74] and Patrick Arnott et al. [83] has been used. Such a resonator consists of a longitudinal half wavelength resonator with a quarter wavelength resonator attached perpendicular to each opening (cf. Figure 2.6). The resonator has a resonance frequency of approximately 1.5 kHz [27]. The weight of the instrument is 18 kg and the size is $18\,cm \times 48\,cm \times 61\,cm$.

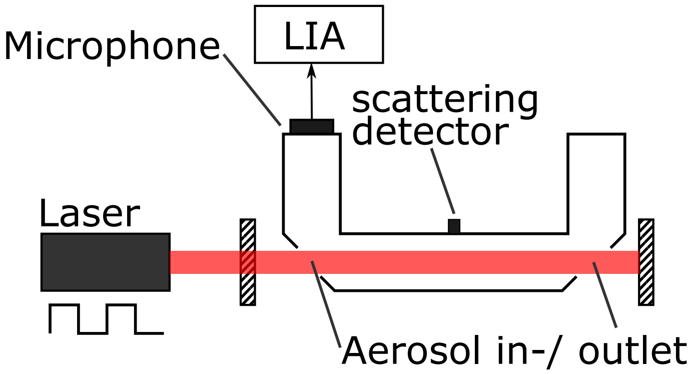

Fig. 2.6 Scheme of the full wavelength plane wave longitudinal resonator described by Moosmüller et al. [74] without buffer volumes. A full wavelength longitudinal wave is formed in the resonator. The aerosol in and outlets are placed at the node of the standing wave. The microphone is placed at the antinode of the quarter wavelength part of the resonator and the signal is fed into a LIA.

2.1.4 Quartz-enhanced photoacoustic spectroscopy

In quartz-enhanced photoacoustic spectroscopy (QEPAS) a quartz tuning fork (QTF) is used as a pressure sensor for the photoacoustic (PA) signal instead of a microphone [51]. The QTF itself serves as a mechanic resonator offering a superb Q-factor, which is around 8000 to 13000 at ambient pressure [16, 82], as compared to the Q factor of 10 to 80 of the acoustic resonators used in conventional PAS. Standard QTFs are mass produced as time base for quartz watches with a resonant frequency f_0 of 32.768 kHz ($2^{15} = 32768$ to derive 1 s by dividing the clock by 2 for 15 times) and are therefore available for prices in the cent range. The high resonance frequency results in small size of the QTF (prong size of approximately $0.58\,\mathrm{mm} \times 0.3\,\mathrm{mm} \times 3.8\,\mathrm{mm}$) and high background noise immunity to $1/f$ noise. Due to the cut of the quartz, QTFs exhibit a high frequency stability with respect to temperature changes (cf. **Paper 4**). Additional advantages are a small and simple sensor design, as the QTF combines the resonator and electric transducer in one component and high background noise immunity, due to the quadrupole characteristic of the QTF [92]. For a commercial QTF relative to conventional PAS, the effect of background noise is reduced by a factor of 46 [91]. The most simple setup is bare fork (bf) QEPAS, first described by [51]. A scheme of this setup is shown in Figure 2.7. The laser modulation frequency is set to the resonance frequency of the QTF, f_0 and both AM and WM are possible. The QTF is mounted in a nonresonant cell with two windows. The laser is focused between the prongs of the QTF. The vertical position of the focus is adjusted such that it is located approximately 0.7 mm from the top of the prongs, which gives the strongest signal [51, 85]. The photoacoustically produced pressure results in resonant stimulation of the QTF, which produces a pA current [85]. Typically, the current signal is converted to a voltage signal with a transimpedance amplifier with a feedback resistance between 4.4 [51] and 10 MΩ (e.g. [62, 25]) and possibly by another voltage amplifier with a band-pass [62], after which the signal is fed into a lock-in amplifier. Although a voltage amplifier is sometimes suggested for the first amplification stage [104, 105, 116] it remains unclear, whether that configuration is superior to the transimpedance amplifier, because QEPAS setups for gas measurements and their characterization in terms of linearity, long-term stability and corresponding noise analysis are yet to be made. Apart from being used as a sensor for point measurements, Kumar et al. [56] demonstrated the application of a QTF as sensor for open-path monitoring.

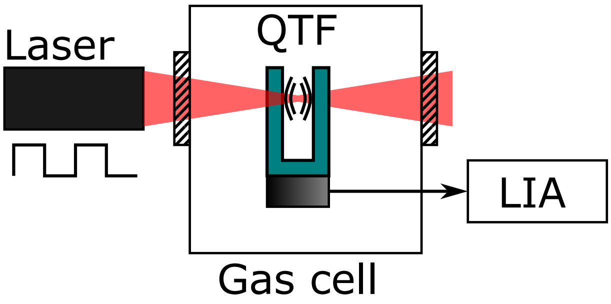

Fig. 2.7 Scheme for a bf QEPAS setup.

Despite its advantages, QEPAS also comes with challenges, especially when using standard QTFs. Standard QTFs have a prong spacing of approximately 300 µm. Therefore, the light source must be very well focused or collimated, in order to fit between the prongs. Still, residual illumination of the prongs always produces background noise. A solution to this might be off-beam configurations, where a small photoacoustic resonator is coupled to a QTF, E-MOCAM, where the background signal is electronically cancelled, or custom QTFs, which can be designed with wider prong spacing. Further, due to the high resonance frequency of a standard QTF, which corresponds to a period of approximately 30 µs, the signal could be attenuated by delayed molecular relaxation for certain molecules (cf. Equation (2.2)). Again, this can be overcome by custom QTFs. Another challenge is arising from methods, which acoustically amplify the QEPAS signal, because the acoustic resonator responds differently to changing environmental conditions than the QTF (cf. section 2.1.4).

Detection schemes

In literature detection schemes beyond the continuous modulation of the laser at f_0 can be found for QEPAS. These include beat frequency QEPAS, where the modulation frequency is scanned around f_0 and the beat frequency signal is analyzed, E-MOCAM, where the background signal is electronically cancelled, electrical co-excitation, where the QTF is part of a pierce oscillator circuit, phase quadrature measurements, and a CHIRP, where the modulation frequency is scanned around f_0 and the response analyzed by an FFT.

Beat frequency QEPAS Beat Frequency QEPAS is described by Wu et al. [120]. The laser is driven by the sum of a slow ramp and a sinusoidal wave with slightly shifted frequency (approx. 200 Hz) to the resonance frequency of the QTF. The resulting electronic signal from the QTF is a decreasing oscillation of the beat frequency between the modulation frequency and the true resonance frequency of the QTF. By that and the decay time, the Q-factor can be determined. The noise equivalent concentrations for 1 s integration time are 59 ppb (H_2O), 10 ppb (CO) and 40 ppm (CH_4).

Electrical modulation cancellation method The electrical modulation cancellation method (E-MOCAM) is advantageous for light sources of poor beam quality, e.g. high power light sources, to electrically cancel the straylight induced noise. Zheng et al. [129] uses a high power LED for detecting NO_2 with QEPAS. In order to get maximum signal amplification, an on-beam configuration (see below) is used, where, as a matter of the poor beam quality, noise is induced by heating the micro-resonator and the prongs with the beam. As this noise differs in phase as compared to the QTF signal, the noise can be suppresed by attaching an electronic signal with the resonance frequency but shifted phase to the QTF where usually ground would be connected. With an average power of 156 mW and 1 s averaging time, a detection limit for NO_2 in N_2 of 1.3 ppb is achieved [129]. Wu et al. [119] reports a detection limit for H_2S of 142 ppb for 67 s integration time (734 ppb with 1 s integration time) with a 1.4 W DFB laser and E-MOCAM. According to the authors the noise is reduced to the theoretical thermal noise due to E-MOCAM.

Electrical co-excitation Mordmüller et al. [76] reports on a low-cost QEPAS approach, which is getting along without a frequency generator. It combines an oscillator circuit which is based on a Pierce-oscillator with a QTF-readout. The measured quantity is the superposition of the electrical and optical signal. This approach has two advantages compared to conventional QEPAS. Firstly, one can go without a precise frequency generator (for modulation and demodulation). Secondly, the setup is immune to changes of the resonance frequency, as the QTF always oscillates at its resonance frequency. This method is intended for low-cost sensors to detect concentrations in the %-range. The detection limit for CH_4 is 10 ppm with a DFB laser of 6.5 mW optical power. The same group described an approach, where the QTF is subsequently excited electrically and optically [75]. With that approach, the background gas density and analyte gas concentration can be determined. The limit of detection of 300 ppm for CH_4 in O_2 is comparable to standard QEPAS sensors.

Phase quadrature measurements Another detection scheme with the QTF as part of an oscillator circuit is described by Levy et al. [59]. Similar to Mordmüller et al. [76], the QTF oscillates at its resonance frequency, which is phase shifted and used for laser modulation. In contrast to Mordmüller et al. [76], the measurement quantity is the induced frequency shift by the photoacoustically generated force on the QTF.

The closed-loop design contains a phase shifter before the laser driver, to obtain phase quadrature (i.e., a $\pi/2$ phase difference between the photoacoustic force acting on the QTF and the piezoelectric force produced by vibration of the QTF. The method enables fast measurements (50 ms), despite the high Q-factor of QTFs (the timescale for one measurement is approximately $\tau = Q/\pi f_0 \approx 100\,\mathrm{ms}$, cf. **Paper 4**). As the induced frequency shift is on the order of mHz, any drift of the resonance frequency, e.g. due to temperature or pressure, must be compensated. This is done by a differential detection scheme (i.e., the difference in frequency, for the phase shifter producing a $\pi/2$ and a $\pi/2 + \pi$ phase shift).

CHIRP method The CHIRP method for conventional PAS was introduced by Szakáll et al. [106] and first mentioned for QEPAS by the author of this thesis [17]. The laser diode is amplitude modulated with a CHIRP signal realized as a series of sine waves of equal duration from 32 700 to 32 800 Hz in 1 Hz-steps in one second. The CHIRP and the QEPAS signal are digitized at 250 ksps and an FFT of both signals is calculated. The FFT of the QEPAS response is normalized by the FFT of the CHIRP to obtain the resonance profile of the QTF. The resulting resonance profile can be fitted with a Lorentzian to determine also the Q factor. The amplitude is proportional to the analyte concentration for sufficiently large concentrations (cf. Appendix A.4). This method does not use a LIA, is immune to changes of f_0 and offers a response time below 1 s.

(Resonant) signal amplification

Since QEPAS was first introduced in 2002 [51], a variety of adoptions have been made, to amplify the signal in QEPAS. Many methods are described in the extensive reviews by Patimisco et al. [82, 80]. Figure 2.8 shows a selection of common QEPAS setups to enhance the signal, which are discussed in detail in the following section.

A drawback to the methods (b) to (d), where an acoustic resonator (acoustic micro-resonator or acoustic recovery) is coupled with the mechanical resonator (QTF), is the different dependence on environmental factors, such as temperature and speed of sound (cf. [24,

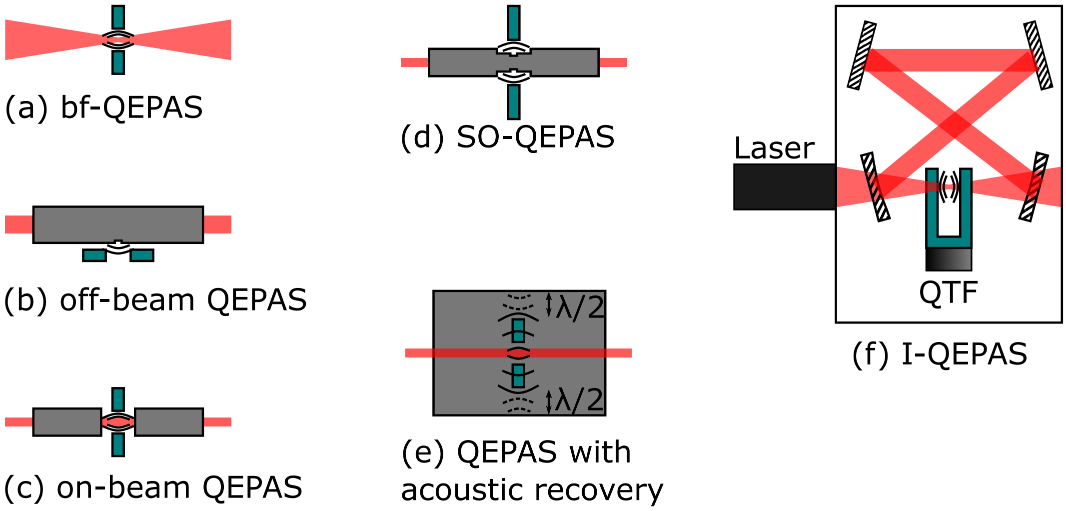
(a) bf-QEPAS

(b) off-beam QEPAS

(c) on-beam QEPAS

(d) SO-QEPAS

(e) QEPAS with acoustic recovery

(f) I-QEPAS

Fig. 2.8 A selection of common QEPAS setups to enhance the signal. All schemes are in top view, with the QTF in turquoise, laser beam in red and acoustic cavities in grey.
(a) bare fork (bf) - QEPAS without signal enhancement. **(b)** off-beam QEPAS (a slit in the acoustic cavity enables acoustic coupling to the QTF). **(c)** on-beam QEPAS. **(d)** single on beam (SO-) QEPAS. **(e)** intracavity (I-) QEPAS with an optical cavity to enhance the laser power.

50, 91], **Paper 4**). Therefore, in contrast to bf QEPAS, these sensors either need different calibration sets for different environmental conditions or an expensive gas conditioning unit. Also the micro resonators used in many of these setups can only be produced and be placed in the QEPAS setup with certain tolerances, which influence the sensor performance [28], thus requiring individual sensor calibration upon application, which leads to higher cost.

Off-beam QEPAS QEPAS setups, where a QTF is combined with an acoustic micro-resonator (amr), such as off-beam QEPAS, are often called spectrophones. The off-beam configuration is shown in Figure 2.8 (b). The excitation laser beam is directed through an amr, which is aligned in the QTF plane. The amr serves as an open-open, pipe-like resonator for the first longitudinal mode, as it is commonly used for conventional PAS. A small slit in the middle of the amr directs the acoustic pressure to a spot centered between the QTF prongs for optimum excitation of the QTF. The off-beam configuration was first mentioned by Liu et al. [62], with an amr of length 8 mm, outer diameter 0.7 mm, inner diameter 0.45 mm and a slit of width 0.15 mm and length 0.4 mm. The signal is by a factor of 15.7 higher than with a bf QEPAS setup. A theoretical treatment for numerically calculating off-beam setups can be found in Yi et al. [123]. Due to the slit in the middle of the longitudinal resonator, the theory of woodwind instruments may be applied for analytical treatments [63], rather than the 'end-correction' equation for pipe-like resonators used in conventional photoacoustic

instruments (cf. section 2.1.2).
Apart from the better signal amplification as compared to bf QEPAS, the light source can have a worse beam quality, as the inner diameter of the amr can be larger than the prong spacing (with an inner diameter of 1.5 mm a signal amplification by 2.8 as compared to bf QEPAS is achieved).

On-beam QEPAS In on-beam QEPAS (sometimes referred to as dual-tube spectrophone), two micro-resonators are aligned perpendicular to the QTF plane (cf. Figure 2.8 (c)). On-beam QEPAS was first described by Kosterev et al. [51], where a signal enhancement by 7.6 as compared to a bf QEPAS setup is achieved. Dong et al. [24] performed a detailed performance evaluation of on-beam resonator geometries. The best signal-to-noise ratio as compared to bf QEPAS was 30. This was achieved at a pressure between 500 and 700 Torr and tubes of length 4.4 mm, which is between $\lambda_s/4$ and $\lambda_s/2$, where $\lambda_s = 10.4\,\mathrm{mm}$ is the acoustic wavelength at a speed of sound $c = 340\,\mathrm{m/s}$. The tubes were positioned at distances of approximately 50 µm from the prongs and had 0.6 mm inner diameter and 0.9 mm outer diameter.
A variant of on-beam QEPAS is the double acoustic micro resonator QEPAS, where two on-beam resonators are placed on top of each other, such that two laser beams can excite the same QTF in on-beam configuration. Since the micro-resonators are not mounted in the vertical position with maximum signal enhancement, the signal-to-noise ratio is lower than for an optimized on-beam configuration. However, the setup allows to measure two gases with the same detector at almost the same time. Dong et al. [26] describes the measurement of H_2O and CO_2 with such a setup.

Custom QTFs So far, QEPAS configurations based on standard QTFs have been discussed. Their small prong spacing (200 to 300 µm) possesses high requirements on the beam quality, since straylight hitting the prongs photothermally excites the prongs to produce a background signal at the laser modulation frequency [81]. In the THz range (optical wavelengths from 60 to 300 µm) explosives, narcotics, and toxic gases show spectral 'fingerprints' and strong absorption bands [14]. However, due to the low spatial beam qualities of THz laser sources [81, 28], custom QTFs with larger prong spacing were developed [14]. Borri et al. [14] used a custom QTF with $f_0 = 4.24673\,\mathrm{kHz}$ and 1 cm prong spacing in bf-configuration to achieve a detection limit of 7 ppm for CH_4 with 4 s integration time and a 3.93 THz (76.3 µm) laser source with 40 µW optical power. It should be noted here, however, that in bf-setups, standard QTFs can have better signal-to-noise ratios than custom QTFs, as a smaller prong spacing is advantageous for sensing the damped cylindrical pressure wave [128].

As was described earlier, the modulation frequency should be high enough to be little susceptible against ambient noise (negligible above approx. 10 kHz [16]), but it should not be too high, in order avoid delayed molecular relaxation (cf. Equation (2.2)). Therefore, custom QTFs are typically designed with a lower resonance frequency than standard QTFs. Custom QTFs allowed new QEPAS operational modes. Eg., the lower resonance frequency allows QEPAS operation at the first overtone mode.

Operation at the first overtone frequency The first overtone mode frequency is approx. 6.3 times higher than the fundamental frequency [81]. According to Patimisco et al. [81], the Q-factor of the fundamental mode is limited by loss mechanisms due to interaction with the air, while the first overtone mode is limited by support losses, due to the fixation of the prongs. Thus, with special QTF designs, the Q-factor can be higher in the first overtone mode than in the fundamental one [81]. The first demonstration of overtone-mode QEPAS was reported by Sampaolo et al. [93]. The QTF with a fundamental mode of approx. 3 kHz had a first overtone frequency of approx. 18 kHz, resulting in a 5 times better signal-to-noise ratio as compared to the fundamental mode of the same QTF, when detecting H_2O [93].
Wu et al. [121] realized a QEPAS setup to simultaneously detect two analytes. Both, the fundamental and the first mode of a custom QTF were excited at the same time with lasers of different wavelengths (one for H_2O, one for C_2H_2). Each laser was positioned at the antinode point of the corresponding mode. The individual QEPAS signals were recovered by using two LIAs, set to the corresponding mode of the QTF vibration.

Single tube on-beam QEPAS The wider prong spacing enables using a single acoustic micro-resonator in on-beam configuration. The so-called single tube on-beam (SO) QEPAS was first described by Zheng et al. [128]. The optimum length of the micro-resonator lay between $\lambda_s/2$ and λ_s. With the SO configuration, the signal-to-noise ratio was by a factor of 128 better than a bf-setup with the same custom QTF. The results were better than that achieved with a standard on-beam configuration.
The SO-QEPAS method was also combined with the first overtone mode, resulting in a signal-to-noise ratio, which is a factor of 380 higher as compared to a bf-setup with the same QTF operated in the fundamental mode [127].
The first overtone mode exhibits two antinodes, which have 180° phase shift. Zheng et al. [126] employed an SO-micro-resonator at each antinode point and excited the first overtone mode by directing a laser through the first micro-resonator, reflect the beam back and direct the phase shifted beam through the second micro-resonator. The resulting signal is more than

three times as high as the signal obtained in an SO-configuration.

Acoustic recovery Duquesnoy et al. [28] described a large custom QTF (prong size of approximately 8 mm × 2 mm × 13.6 mm) with a resonance frequency of 21.23 kHz and a Q-factor of 7600. The QTF is optimized for a high acoustic radiation loss, which is reflected back to the QTF by using an acoustic recovery. The acoustic recovery improves the Q-factor to around 45400. The acoustic recovery consists of a metal cylinder, surrounding the QTF, with a distance of $\lambda/2$ between the outer prong surface and the wall, to resonantly reflect the acoustic waves onto the prong's surface. By additionally implementing an on-beam configuration, an NNEA of $3.7 \times 10^{-9}\,\mathrm{cm^{-1}W/\sqrt{Hz}}$ for CO_2 is achieved.

Intracavity QEPAS Intracavity (I) QEPAS was first reported by Borri et al. [13]. An optical cavity was built in form of a bow-tie by two flat and two concave mirrors (cf. Figure 2.7 (f)). The QTF is placed in the optical resonator to allow multiple gas interactions of the laser beam between the QTF prongs. The high finesse (1500) leads to a power enhancement by approximately 250. Compared to a bf QEPAS setup without optical cavity, the detection limit is improved by this factor of 250. In this setups, it is crucial to fine tune the cavity length to the desired laser wavelength. This is done by mounting one of the flat mirrors on a piezoelectric transducer. In a more recent publication a power enhancement factor of 1276 is reported [117]. A detection limit of 4.8 ppb for NO is achieved with an integration time as low as 30 ms with a 5.263 µm DFB QCL with 133.2 mW.

Aerosol QEPAS So far, this section described the measurement of trace gases. To the best of the author's knowlede, **Paper 5** is the first demonstration of the measurement of a continuous flow of arosol with QEPAS. The bf setup to sense soot will be described in detail in Section 4.

2.1.5 Photothermal interferometry

As stated in the beginning of this chapter, PTI on gases can be performed with a variety of interferometers. Therefore, exemplary, the work by Campillo et al. [18] is described, while an extensive review on photothermal gas detection might be found elsewhere [54]. Also, we note here that the folded Jamin interferometer [73] has been succesful applied to the detection of black carbon with photothermal interferometry [99, 98].
The setup used by Campillo et al. [18] is shown in Figure 2.9. A commercial Fabry–Pérot cavity of length 12 cm was used to perform PTI on NO_2. Both, the excitation beam

($\lambda = 514.5\,\mathrm{nm}$, $P_{exc} = 3\,\mathrm{W}$) and the probe beam ($\lambda = 633\,\mathrm{nm}$) enter the cavity perpendicular to the mirrors. A gas cell is placed inside the cavity and filled with the gas sample.

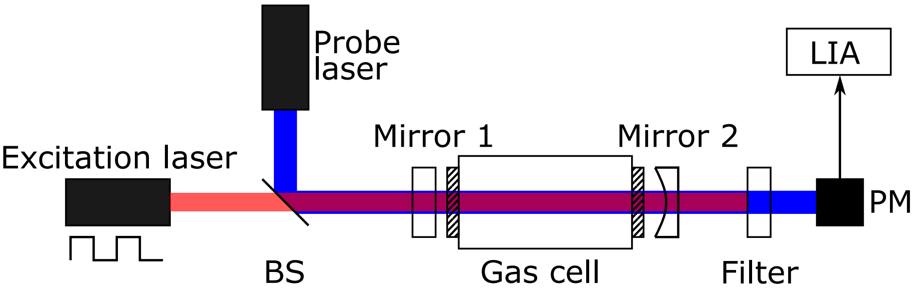

Fig. 2.9 Scheme for photothermal interferometry with a Fabry–Pérot interferometer. BS . . . beam splitter; PM . . . power meter. Simplified drawing of the setup used by Campillo et al. [18].

Periodic absorption of the modulated probe beam and subsequent derelaxation of the NO_2 molecules heats the gas. The periodic change of temperature leads to a periodic change in refractive index Δn, described by the Clausius–Mosotti equation [23], with ΔT temperature rise and T_{abs} absolute temperature of the gas:

$$\Delta n = -(n-1)\frac{\Delta T}{T_{abs}}. \tag{2.3}$$

This change in refractive index is directly proportional to the number of NO_2 molecules in the sample. This change in refractive index can be seen as an intensity change of the probe beam with a power meter. Mirror 2 in Figure 2.9 can be adjusted to adopt the path length within the cavity to operate the Fabry–Pérot interferometer (FPI) at its optimal operation point ϕ_0, i.e. where a change in refractive index leads to a linear change in transmitted intensity. The filter in Figure 2.9 blocks out the excitation beam, such that it is not measured by the power meter. To obtain the optimal operation point of the FPI, a control loop which is modulated at the excitation laser modulation frequency, adjusts the mirror spacing such that ϕ_0 is maintained.

2.2 Theoretical concepts

The following section starts with a brief summary of the theoretical concepts of conventional photoacoustic spectroscopy. Due to the main focus of this work on QEPAS, the main focus is laid on revisiting the analytical QEPAS model described by Petra et al. [85] and adoptions of the MATLAB model available from the same group [84]. Furthermore, an order of magnitude calculation for the detection limit of photothermal interferometry (PTI) is given in the last chapter.

2.2.1 Conventional photoacoustic spectroscopy

This chapter is based on the works by Miklós et al. [71] and Bozóki et al. [16] and describes the signal of an organ-pipe resonator. The first longitudinal mode f_1 of the commonly used organ-pipe resonator, can be estimated as

$$f_1 = \frac{c}{2\,(L+\Delta L)}, \tag{2.4}$$

where c is the speed of sound, L the length of the resonator and ΔL an end correction factor ($\Delta L \approx 0.6R$, with R the resonator radius) [71].

For a monochromatic light source of wavelength λ and no cross-interference to other species, the photoacoustic signal $S(c)$ (in mV) as a function of the analyte concentration c (in $\mathrm{mol\,dm^{-3}}$) is given by [16]

$$S(c) = P \cdot M(\cdot C \cdot \eta \cdot \tilde{\alpha} \cdot c + A_b), \tag{2.5}$$

where P is the exciting light power, M the sensitivity of the microphone (in mV/Pa), C is the cell constant (also called setup constant in [71]), η the efficiency of light conversion into heat, $\tilde{\alpha}$ the optical absorption coefficient of the analyte at λ (in $\mathrm{dm^3mol^{-1}cm^{-1}}$) and A_b the background signal generation efficiency. As noted before, the background signal $P \cdot M \cdot A_b$ as well as the useful signal $P \cdot M \cdot C \cdot \eta \cdot \tilde{\alpha} \cdot c$ are complex quantities with different phases.

The microphone sensitivity M is typically on the order of 10 to 50 mV/Pa for commonly used electret microphones. Also condenser microphones, MEMS microphones and optical microphones are used. The latter offer superb microphone sensitivities (no distinct value can be found in literature), which offer a factor 100 lower detection limit than conventional PAS systems [61] (cf. section 2.1.3).

The cell constant C for a cylindrical resonator is given by [71]

$$C = \frac{(\gamma - 1) \cdot L \cdot Q \cdot p_n(\boldsymbol{r}_M) \cdot F_n}{f_0 \cdot V}, \tag{2.6}$$

where γ is the adiabatic index of the gas, L and V are the length and the volume of the cylinder, Q the Q-factor of the acoustic amplification by the resonator at resonance frequency f_0, $p_n(\boldsymbol{r}_M)$ the eigenmode distribution function at the position of the microphone (usually close to unity, as the microphone is usually placed at a pressure antinode) and F_n the normalized overlap integral (also close to unity). The product $p_n(\boldsymbol{r}_M) \cdot F_n$ is also called the geometrical factor G. The normalized overlap integral F_n is defined as the quotient of the overlap integral and the normalization factor of the nth eigenmode as [71]

$$F_n = \frac{\frac{1}{L}\int g(\boldsymbol{r}) p_n(\boldsymbol{r}) dV}{\frac{1}{V}\int \mid p_n(\boldsymbol{r}) \mid^2 dV}, \tag{2.7}$$

where $g(\boldsymbol{r})$ is the normalized intensity distribution of the excitation laser. The overlap integral thus describes how well the nth eigenmode is excited by the spatial distribution of the laser [71].

2.2.2 Quartz-enhanced photoacoustic spectroscopy

Models for QEPAS have been studied in COMSOL for bf setups [35] and on-beam setups [36]. Also, analytical models for QEPAS with amr [6] and bf setups [85] are described in literature. Here, we will use the analytical model by Petra et al. [85] to describe the bf QEPAS setup used for **Paper 4** and **Paper 5**. The model consists of the following steps: (i) photoacoustic pressure generation, (ii) forced vibration of the prongs due to that pressure and (iii) production of the piezoelectric current due to the prong vibration.

Photoacoustic pressure

The foundation of the QEPAS model by Petra et al. [85] is the description of the pressure $P(r,t)$ by the acoustic wave equation [85]

$$\frac{\partial^2 P(r,t)}{\partial t^2} - c^2 \cdot \Delta P(r,t) = (\gamma - 1)\frac{\partial H(r,t)}{\partial t}, \tag{2.8}$$

with c the speed of sound, γ the adiabatic index (1.4 in air) and $H(r,t)$ the heat power density deposited in the gas by absorption of the laser. Petra et al. [85] neglects delayed molecular relaxation (cf. Equation (2.2)) resulting in the following expression for the heat power density:

$$H(r,t) = \alpha \cdot I(r) \cdot \exp(i\omega t), \tag{2.9}$$

with absorption coefficient α, modulation $\omega = 2\pi \cdot f$ and $I(r)$ the laser power density. If the optical laser power is modulated between zero and P_L and a gaussian beam profile of beam diameter σ is assumed, it is of form $I(r) = \frac{P_L}{2} \cdot \frac{1}{2\pi\sigma^2} e^{\frac{-r^2}{2\sigma^2}}$ [85]. Thus, by taking the derivative $\frac{\partial H}{\partial t}$ and neglecting the phase factor of $\frac{\pi}{2}$, by multiplying $\frac{\partial H}{\partial t}$ by i, Equation (2.8) now reads as

$$\frac{\partial^2 P(r,t)}{\partial t^2} - c^2 \Delta P(r,t) = \underbrace{-\omega \cdot (\gamma - 1) \cdot \alpha \cdot \frac{P_L}{2} \cdot \frac{1}{2\pi\sigma^2}}_{:=M=-Q(r)\cdot c^2 \cdot e^{\frac{r^2}{2\sigma^2}}} \cdot e^{\frac{-r^2}{2\sigma^2}} \cdot \exp(i\omega t). \tag{2.10}$$

The pressure is assumed to be of the form $P(r,t) = p(r)\exp(i\omega t)$ (steady state solution, no dependency on azimuth). A transformation of Equation (2.10) into cylindrical coordinates results in the inhomogeneous Bessel equation of order zero for $p(r)$ [85]

$$\frac{\partial^2 p(r)}{\partial r^2} + \frac{1}{r}\frac{\partial p(r)}{\partial r} + k^2 p(r) = Q(r), \tag{2.11}$$

with $k = \omega/c$.

A solution of Equation (2.11) is of the form (see also Appendix A.5) [85]

$$P(r,t) = \frac{\pi M}{2c^2}\left(f_1(r) - i f_2(r)\right) \cdot \exp(i\omega t) \tag{2.12}$$

where f_1 and f_2 depend on the zeroth order Bessel functions of the first and second kind, $J_0(kr)$ and $Y_0(kr)$ as [85]

$$f_1(r) = \left(-\lim_{r\to\infty} \int_0^r sY_0(ks)e^{\frac{-s^2}{2\sigma^2}} ds + \int_0^r sY_0(ks)e^{\frac{-s^2}{2\sigma^2}} ds \right) \cdot J_0(kr) - \\ - \int_0^r sJ_0(ks)e^{\frac{-s^2}{2\sigma^2}} ds \cdot Y_0(kr) \tag{2.13}$$

$$f_2(r) = \lim_{r\to\infty} \int_0^r sJ_0(ks)e^{\frac{-s^2}{2\sigma^2}} ds \cdot J_0(kr) \tag{2.14}$$

Hence, the amplitude $A(r)$ is given by [85]

$$A(r) = \frac{\pi M}{2c^2} \cdot \sqrt{f_1(r)^2 + f_2(r)^2}. \tag{2.15}$$

In the case of $\sigma << r$, Equation (2.15) can be approximated by [85]

$$A_{approx}(r) = \left| \frac{\pi M}{2c^2k^2} \cdot \frac{(2(k\sigma)^2)^2}{2} \right| \cdot \sqrt{J_0(kr)^2 + Y_0(kr)^2} = \tag{2.16}$$

$$= \omega \cdot (\gamma - 1) \cdot \alpha \cdot \frac{P_L}{2} \cdot \frac{1}{4c^2} \sqrt{J_0(kr)^2 + Y_0(kr)^2}, \tag{2.17}$$

and the amplitude is independent of the beam width. A contour plot of the pressure amplitude is shown in Figure 2.10. The amplitude of the pressure for different beamwidths shown in Figure 2.11(a).

Vibration of the QTF prongs

In Petra et al. [85], the QTF is modelled as two independent cantilevers (prongs), fixed at the bottom. Therefore, it is sufficient to describe the deflection of the right prong and multiply the result by two.

The cantilevers of width W, thickness T and length L are assumed to be acoustically transparent and the acoustic pressure $P(x,y,t)$ results in a force density $f(y,t)$ between the inner and the outer surface of the prong as [85]

$$f(y,t;y_0) = T \cdot [p(r_i) - p(r_o)] \cdot \exp(i\omega t), \tag{2.18}$$

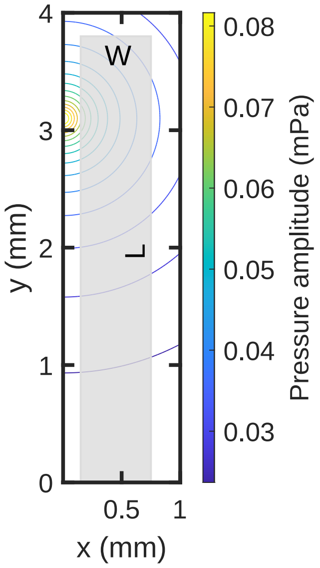

Fig. 2.10 Contour plot of the pressure amplitude with the laser focused at $x = 0\,\text{mm}$ and $y = 3.1\,\text{mm}$. The shape of the QTF prong of width W and length L is drawn in gray.

where $r_i = \sqrt{(\frac{g}{2})^2 + (y - y_0)^2}$ and $r_o = \sqrt{(W + \frac{g}{2})^2 + (y - y_0)^2}$ are the positions at the inner and outer surface of a prong. The deflection $u(y,t)$ of a prong can be described by the Euler-Bernoulli beam theory: [85]

$$\frac{E \cdot I}{\rho \cdot A} \frac{\partial^4 u}{\partial y^4} + 2\beta \frac{du}{dt} + \frac{\partial^2 u}{\partial t^2} = \frac{1}{\rho \cdot A} \cdot f(y,t). \tag{2.19}$$

Here, E is the Young's modulus, I the second moment of area, A the cross-sectional area of the prong (thickness times width), 2β the damping coefficient, and ρ the density of the quartz.

The prong deflection $u(y,t)$ for the first eigenfrequency ($\omega = \omega_1$) is given by [85]

$$u(y,t) = \left| \frac{M_1(y_0)}{2\beta\omega} \right| \cdot \Phi_1(y) \cdot \sin\left(\omega t - \delta_1(y_0)\right), \tag{2.20}$$

with

$$tan(\delta_1(y_0))\Big|_{\omega=\omega_1} = \frac{\Re(M_1)}{\Im(M_1)}, \tag{2.21}$$

$$M_1(y_0) = \frac{1}{\rho \cdot A} \frac{\int_0^L f(y;y_0)\Phi_1(y)dy}{\int_0^L \Phi_1^2(y)dy}, \tag{2.22}$$

and

$$\begin{aligned}\Phi_1(y) =&(cosh(\lambda_1 \cdot L) + cos(\lambda_1 \cdot L)) \cdot (sinh(\lambda_1 \cdot y) - sin(\lambda_1 \cdot y)) - \\ &- (sinh(\lambda_1 \cdot L) + sin(\lambda_1 \cdot L)) \cdot (cosh(\lambda_1 \cdot y) - cos(\lambda_1 \cdot y)),\end{aligned} \tag{2.23}$$

where $\lambda_1 L/\pi \approx 0.59686$ is the first root of $\cosh(\beta_n L)\cos(\beta_n L) + 1 = 0$ [53, 84].

Production of the piezoelectric current

Petra et al. [85] derive the piezoelectric current by combining the mechanical model with the RLC equivalent circuit (**Paper 4**, [108]). The maximum piezoelectric charge by both prongs q is $q = 2 \cdot \alpha_{piezo} \cdot u(L,t)$ where α_{piezo} is the effective piezoelectric coupling constant [85]. The current $I(t)$ is calculated by the derivative $I(t) = \frac{dq}{dt} = 2 \cdot \alpha_{piezo} \cdot \dot{u}(L,t)$. The maximum current is then

$$I(y_0) = 2 \cdot \alpha_{piezo} \cdot \omega \cdot \left| \frac{M_1(y_0)}{2\beta\omega} \right| \cdot \Phi_1(L). \tag{2.24}$$

The effective piezoelectric coupling constant can be derived by equating the maximum kinetic energy from the mechanical model to the energy stored in the RLC equivalence circuit, i.e. $2(1/2m_e)v^2 = LI^2/2$, with $m_e = m/L \int_0^L \Phi_1^2(y)dy/\Phi_1^2(L)$ the effective mass of the prong with mass m, the maximum velocity $v = \dot{u}(L,t)$, and L the inductance. Rearranging this equation gives the proportionality constant α_{piezo} between I and $2v$: [85]

$$I = 2 \cdot \underbrace{\sqrt{\frac{m_e}{2L}}}_{=\alpha_{piezo}} \cdot v. \tag{2.25}$$

Using definitions from the RLC equivalence circuit, α_{piezo} can be written as $\alpha_{piezo} = \sqrt{\frac{m_e\omega}{2QR}}$. Thus, the piezoelectric current from Equation (2.24) can alternatively be written as (with $Q = \omega/2\beta$)

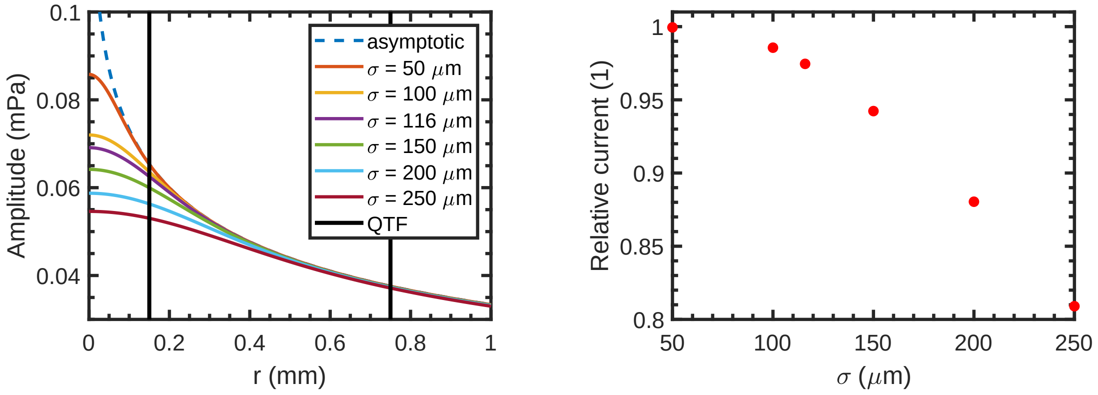

(a) (b)

Fig. 2.11 **(a)** Contour plot of the acoustic pressure amplitude calculated with the model of Petra et al. [85] and shape of the QTF (black) for the setup as described in **Paper 4** and 4650 ppb NO_2. **(b)** Current as a function of the beam diameter relative to the asymptotic case. For the above concentration the current is calculated to be 8.38 pA (with molecular relaxation).

$$I(y_0) = 2 \cdot \sqrt{\frac{Qm_e}{2\omega R}} |M_1(y_0)| \cdot \Phi_1(L). \tag{2.26}$$

Influence of the beam width

To investigate the influence of the beam width, the available MATLAB code [84] was adopted to the setup described in **Paper 4** and a concentration of 4650 ppb. Figure 2.11(a) shows the pressure amplitude as a function of the distance from the laser spot. The smaller the beam diameter σ, the larger the pressure at the inner prong surface. Since this pressure difference drives the prong motion, the beam diameter should be as small as possible. Figure 2.11(b) shows the generated piezoelectric current, relative to the asymptotic case $\sigma << r$. The setup described in **Paper 4** has a beam diameter of 116 µm and thus the signal is approximately 97 % of the maximum possible signal. However, a beam diameter of e.g. 200 µm would decrease the signal to approximately 88 %.

An additional consideration

It has been shown, that relaxation processes can lead to nonlinear photoacoustic signal generation [58]. In the case of a two-level system, the multiplication with an efficiency η as described by Equation (2.2) is sufficient. By consindering η, the source term for the photoacoustic pressure is [11]

$$H'(r,t) = \eta \cdot \alpha \cdot I(r) \cdot e^{-i(\omega t - \phi)}, \tag{2.27}$$

with $\phi = arctan(\omega\tau)$. Thus, to account for delayed molecular relaxation, the current from Equation (2.26) needs to be multiplied by η.

To be able to compare the QEPAS-generated signal to the signal by a conventional PAS setup, the QEPAS signal may be rewritten in the form of Equation (2.5). After including η as described above, the piezoelectrically produced current (Equation 2.24) can be multiplied by the value of the feedback resistor of the transimpedance amplifier R_f. By using the expression for the pressure at the asymptotic case ($\sigma << r$), the voltage produced in QEPAS (without background) can be written as:

$$S_{QE}(c) = P_L \cdot M_{QE} \cdot C_{QE} \cdot \eta \cdot \tilde{\alpha} \cdot c, \tag{2.28}$$

with the tuning fork sensitivity M_{QE} (the voltage produced per force acting on the prong surface) defined as

$$M_{QE} = R_f \cdot \alpha_{piezo} \cdot \frac{1}{\rho W \beta}, \tag{2.29}$$

and the QEPAS 'cell-constant' C_{QE} defined as

$$C_{QE} = (\gamma - 1) \cdot \omega \cdot \frac{1}{8c^2} \cdot \tag{2.30}$$

$$\cdot \left| \Phi_1(L) \frac{\int_0^L \Phi_1(y) \cdot (Y_0(k \cdot r_i(y;y_0)) + iJ_0(k \cdot r_i(y;y_0)) - Y_0(k \cdot r_o(y;y_0)) - iJ_0(k \cdot r_o(y;y_0)))\, dy}{\int_0^L \Phi_1^2(y) dy} \right| . \tag{2.31}$$

For a standard QTF, as it was used for this thesis, the tuning fork sensitivity is calculated to be $M_{QE} = 1254\,\mathrm{mV/Pa}$, which is by a factor 25 to 125 higher than a typical microphone sensitivity used in PAS (cf. Section 2.1.2). In contrast, the constant C_{QE} has a value of $6.25\,\mathrm{Pa\,cm\,W^{-1}}$, which is 320 times lower than the cell constant of a pipe-like resonator PA cell [16]. Thus, the signal produced by QEPAS can be expected to be approximately ten times smaller than in conventional PAS. The PAS setup described by Yin et al. [124] uses a light source of the same wavelength as in **Paper 4** for NO_2 detection. There, a constant of $M \cdot C = 10.7\,\mathrm{V\,cm\,W^{-1}}$ is reported, as compared to our setup with $M_{QE} \cdot C_{QE} = 0.078\,\mathrm{V\,cm\,W^{-1}}$. Since the noise levels are of the same order of magnitude (µV range in [124]; 0.85 µV in our QEPAS setup, as described below) it can be assumed, that the detection limit relative to the laser power is two orders of magnitude better in PAS than in QEPAS. This is indeed the case (QEPAS: 160 ppb with 47 mW average optical power and 1 s integration time; PAS: 54 ppt with 1.3 W average optical power and 1 s integration time [124]).

Fundamental limitations of bf QEPAS with a standard QTF

The piezoelectric signal from the QTF is typically amplified by a transimpedance amplifier (TIA) with feedback resistor R_f. The thermal noise (Johnson–Nyquist noise) $\sqrt{< V_N^2 >}$ in such a setup is comprised of thermal noise of the equivalence resistor of the QTF circuit, R (cf. **Paper 4**) and the noise due to R_f. Since the latter is $\sqrt{\frac{R_g}{R}} \approx \sqrt{\frac{3\,\mathrm{M\Omega}}{100\,\mathrm{k\Omega}}} \approx 6$ times lower, it is usually neglected. The thermal noise is well approximated by [52]

$$\sqrt{< V_N^2 >} = R_f \sqrt{\frac{\Delta f 4 k_B T}{R}}, \tag{2.32}$$

where Δf is the detection bandwidth, k_B is the Boltzmann constant, and T is the temperature.

In order to design a QEPAS sensor, it is of interest to estimate the minimal detectable concentration beforehand. The minimal detectable concentration is the concentration, where the noise from Equation (2.32) equals the signal from Equation (2.28):

$$MDC_{1\sigma} = \frac{\sqrt{\frac{\Delta f 4 k_B T}{R}}}{P_L \cdot M_{QE} \cdot C_{QE} \cdot \eta \cdot \tilde{\alpha}}. \tag{2.33}$$

Comparison to experiment

Noise For the setup used in this thesis ($\Delta f = 0.88\,\mathrm{Hz}$ for 1 s; cf. Section 3, $R_f = 2.9\,\mathrm{M\Omega}$[1] and $T \approx 300\,\mathrm{K}$), the thermal noise is calculated to be $\sqrt{< V_N^2 >} = 1.19\,\mathrm{\mu V}$ after the TIA. The noise after the second amplification stage, which amplifies by 270 is then $V_{2nd} = \sqrt{< V_N^2 >} \cdot 270 = 321\,\mathrm{\mu V}$. This value is of the same order of magnitude as our experimental

---

[1] In **Paper 4** it is discussed that although a feedback resistor of $R_f = 6.8\,\mathrm{M\Omega}$ is used, stray and other capacitances lead to a low-pass behaviour, which could effectively reduce the value of R_f at the resonance frequency of the QTF to $R'_f \approx 2.9\,\mathrm{M\Omega}$.

data in **Paper 5**, where a fundamental thermal noise of 201 µV was measured[2].

QEPAS response Equation (2.28) may also be used to estimate the QEPAS signal at a given concentration. For 4650 ppb NO_2 the absorption coefficient is $\alpha = 5.022 \times 10^{-5}\,\mathrm{cm}^{-1}$ according to the HITRAN database [111]. Then the voltage after the second amplifier would be $U_{2nd} = 6.4\,\mathrm{mV}$ with $\eta \approx 0.79$ (cf. Chapter 3), which is of the same order of magnitude as the experiment, where 6.44 mV have been measured.

Detection limit For the setup described in **Paper 4** the minimal detectable concentration according to Equation (2.33) is 230 ppb which is of the same order of magnitude as the experiment (160 ppb).

For the setup described in **Paper 5** ($P_L = 30\,\mathrm{mW}$, with $\eta = 1$), a specific cross-section for Diesel soot of $\sigma_s \approx 5\,\mathrm{m}^2\,\mathrm{g}^{-1}$ for a wavelength of 850 nm is reported [95]. The minimal detectable concentration (1σ) is determined to be $102\,\mu\mathrm{g}\,\mathrm{m}^{-3}$, which is of the same order of magnitude as the experimentally determined value of $96\,\mu\mathrm{g}\,\mathrm{m}^{-3}$.

2.2.3 Photothermal interferometry

This section describes an order of magnitude calculation for the sensitivity of PTI for the setup described in **Paper 3**.

The phase shift $\Delta\phi$ in an interferometer due to a photothermaly induced refractive index change, for an excitation beam parallel to (and overlaping) the probe beam is given by [99]

$$\Delta\phi = \frac{2\pi l}{\lambda} \frac{(n-1)}{T_0} \frac{\alpha I_{exc}}{\rho C_p f}, \tag{2.34}$$

with l the path length, λ the wavelength of the probe beam, n the refractive index of air, T_0 the absolute temperature, ρ the density of air, C_p the specific heat of air at constant pressure, f the modulation frequency, α the absorption coefficient of the analyte and I_{exc} the excitation laser intensity.

The sensitivity of the FPI is given by the first derivative of the FPI's transmission function

---

[2] The estimation of the QEPAS response relies on the estimation of the equivalence resistance R as described in **Paper 4**. Since its value relies on the measurement of a small capacity, which underlies a large uncertainty, the estimation of the QEPAS signal, the fundamental noise and the detection limits are order of magnitude estimations.

around the inflection point (cf. Appendix A.6), which for the FPI used in **Paper 3** ($R \approx 0.6$) is

$$\delta P = 1.2 \cdot P_{probe} \delta\phi, \tag{2.35}$$

where $\delta\phi$ is the change in phase shift, P_{probe} is the power of the probe beam and δP the change in power due to the phase shift. The detector shot noise $\sqrt{< \Delta P_N^2 >}$ is given by [99]

$$\sqrt{< \Delta P_N^2 >} = \sqrt{\frac{c}{\lambda} 2h\eta_{det} P_{probe} \Delta f}, \tag{2.36}$$

with c the speed of light, h Planck's constant, η_{det} the detector quantum efficiency and Δf the detection bandwidth. Rearranging Equation 2.34 for the absorption coefficient α and plugging in $\delta\phi$ from rearranged Equation (2.35) for $\Delta\phi$, as well as $\sqrt{< \Delta P_N^2 >}$ from Equation (2.36) for δP, yields

$$\begin{aligned} \alpha_{min,1\sigma} &= \frac{\lambda}{2\pi l} \frac{T_0}{(n-1)} \frac{\rho C_p f}{I_{exc}} \frac{1}{1.2 \cdot P_{probe}} \sqrt{\frac{c}{\lambda} 2h\eta_{det} P_{probe} \Delta f} \cdot \eta = \\ &= \frac{1}{2\pi l} \frac{T_0}{(n-1)} \frac{\rho C_p f}{I_{exc}} \frac{1}{1.2} \sqrt{\frac{c\lambda}{P_{probe}} 2h\eta_{det} \Delta f} \cdot \eta \end{aligned} \tag{2.37}$$

for the minimum detectable absorption coefficient. η was added to account for delayed molecular relaxation (cf. Chapter 3 and Appendix A.2). To make the setup from **Paper 3**, with the excitation beam perpendicular to the probe beam comparable to the setup described by Equation (2.37) where the excitation beam is parallel to the probe beam, the length l is adopted. The overlap of the excitation and probe beam in **Paper 3**, modelled here as two cylinders of equal radius r, form a volume of $V_{cut} = r^3 \cdot 16/3$. A cylinder of equal volume has a length of $l = r/\pi \cdot 16/3$ which is used as a cavity length for our order of magnitude calculation. With the values from **Paper 3** ($\lambda = 1550\,\text{nm}$, $r = 102.5\,\mu\text{m}$, $T_0 = 300\,\text{K}$, $n - 1 = 2.92 \times 10^{-4}$, $\rho = 1.205\,\text{kg/m}^3$, $C_p = 1005.4\,\text{J/kK}$, $f = 1.4\,\text{kHz}$, $I_{exc} = 90\,\text{W}\,\text{cm}^{-2}$, $P_{probe} = 1\,\text{mW}$, $\Delta f = 0.44\,\text{Hz}$, $\eta_{det} = 0.6$ [99], $\eta = 0.85$) the minimum absorption coefficient as described by Equation (2.37) corresponds to a minimum detectable concentration of $MDC_{1\sigma} = 21\,\text{ppb}$. Considering that a detector is approximately a factor 10 worse than its quantum efficiency [18], this leads to $MDC_{1\sigma} = 210\,\text{ppb}$, which is a good order of magnitude estimation for the experimental detection limit of 348 ppb.

Furthermore, Equation (2.37) shows that without increasing the laser power, the detection limit can be improved, either by a higher overlap of excitation and probe beam, e.g. by parallel alignment, or higher mirror reflectivity. E.g., $R = 0.95$ leads to a factor 12.7 instead of 1.2 in the denominator and thus an improvement in the detection limit by a factor of ≈ 10.

Chapter 3

NO_2 Sensing concepts

3.1 Introduction

3.1.1 Nitrogen dioxide

NO_2 exhibits strong absorption in the visible range of light (cf. Figure 3.1). In that range, light absorption by NO_2 is caused by electronic transitions to the $^2B_1$ and $^2B_2$ states [39]. Due to the long lifetime of the two excited states ($\approx 50\,\mu s$) and the high density of ro-vibrational states, both the $^2B_2 \leftarrow {}^2A_1$ and $^2B_1 \leftarrow {}^2A_1$ transitions can efficiently produce a photoacoustic signal [102].

For both, the QEPAS and the PTI setup, 450 nm laser diodes were used. This wavelength was chosen due to the high absorption by NO_2 at this wavelength and negligible cross-interference to other gases (cf. Figure 3.1). To overcome possible cross-interference by the broad absorption range of soot a filter can be placed at the sampling inlet.

Although NO_2 exhibits stronger absorption towards 400 nm, wavelengths below approximately 415 nm are less suitable for generating a photoacoustic signal, because a fraction of the photons is lost by promoting photodissociation of NO_2 (e.g. around 35 % at 405 nm excitation wavelength) [88].

For PA NO_2 sensors with excitation wavelengths in the 450 nm range, signal decrease due to vibrational-vibrational relaxation of NO_2 to O_2 ($VV_{NO_2\text{-}O_2}$) has been reported [46]. This effect is particularly relevant when calibrating environmental NO_2 sensors in mixtures with N_2, as the signal would effectively be 15 % lower than at typical O_2 concentrations in air and should therefore be carried out with synthetic air. The correlation is described by Eq. (3.2), where S is the photoacoustic signal, x is the oxygen concentration, and $\frac{k_{O_2-VT}}{k_{N_2-VT}} = 5$

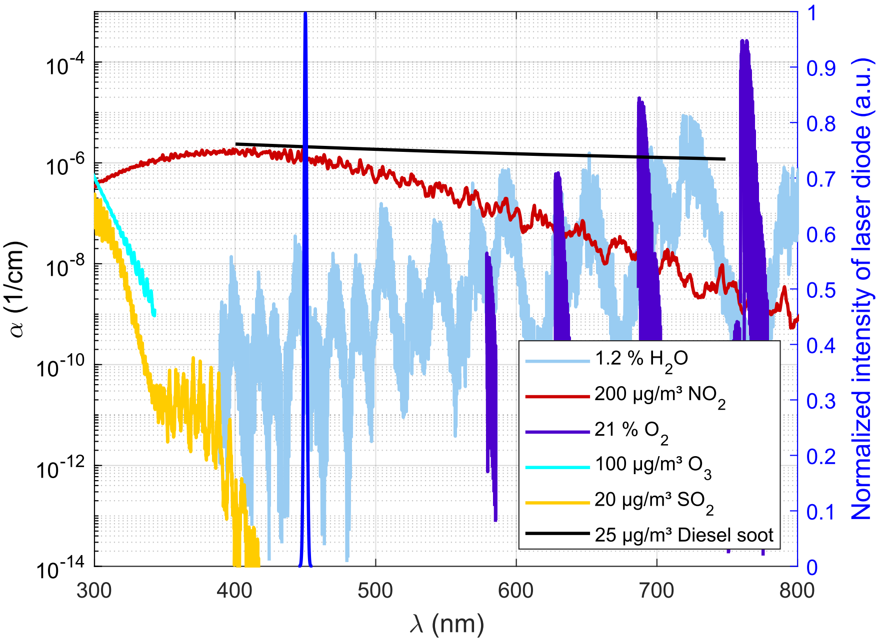

Fig. 3.1 Absorption of different environmental gases between 300 nm and 800 nm according to the HITRAN database [111, 89] and absorption of diesel soot between 400 nm and 750 nm [95]. Concentrations reflect the current WHO recommended limits (NO$_2$: 1-hour mean, O$_3$: 8-hour mean, SO$_2$: 24-hour mean, Diesel soot (PM$_{2.5}$): 24-hour mean) [113]. Laser emission spectrum is shown in blue. Figure from **Paper 4**.

and $\frac{k_{O_2-VV}}{k_{N_2-VT}} = 1.5$ are constants describing the rate of different relaxation pathways [46]. A verification experiment is shown in Appendix A.2.

$$S \propto \frac{(1-x)\cdot k_{N_2-VT} + x\cdot k_{O_2-VT}}{(1-x)\cdot k_{N_2-VT} + x\cdot (k_{O_2-VT} + k_{O_2-VV})} = \tag{3.1}$$

$$= \frac{(1-x) + x\frac{k_{O_2-VT}}{k_{N_2-VT}}}{(1-x) + x(\frac{k_{O_2-VT}}{k_{N_2-VT}} + \frac{k_{O_2-VV}}{k_{N_2-VT}})} \tag{3.2}$$

The factor of 0.85 due to delayed molecular relaxation by O$_2$ is multiplied by an efficiency calculated according to Equation (2.2) with $\tau = 2\,\mu\text{s}$ [46] and $f_0 = 32.768\,\text{kHz}$ to get an efficiency for signal generation with QEPAS of $\eta \approx 0.79$. The factor might be close to 1 if a high concentration of water vapor is present in the gas mixture, which is a promoter of molecular relaxation ([124], **Paper 4**). Due to the low modulation frequency used in PTI, only the VV$_{\text{NO}_2\text{-O}_2}$ relaxation plays a role and the efficiency is $\eta = 0.85$.

3.1.2 Experimental

As the setups for characterization of the PTI and QEPAS setup are fairly similar, a general schematic is shown in Figure 3.2. Gas mixtures are produced with a custom gas diluter. To produce stable gas mixtures at a high dynamic range (1 : 1400) and low uncertainty (1.9% for the lowest concentration, including the uncertainty of the gas mixture), a gas diluter based on binary weighted critical orifices was designed and built as part of this thesis. A detailed discussion and verification can be found in **Paper 2** (see Appendix A.3 for a photograph). The flow rate of the gas mixtures through the cell are controlled by a mass flow controller (MFC; Vögtlin: Model GSC-B) while excess flow is bypassed to a ventilation.

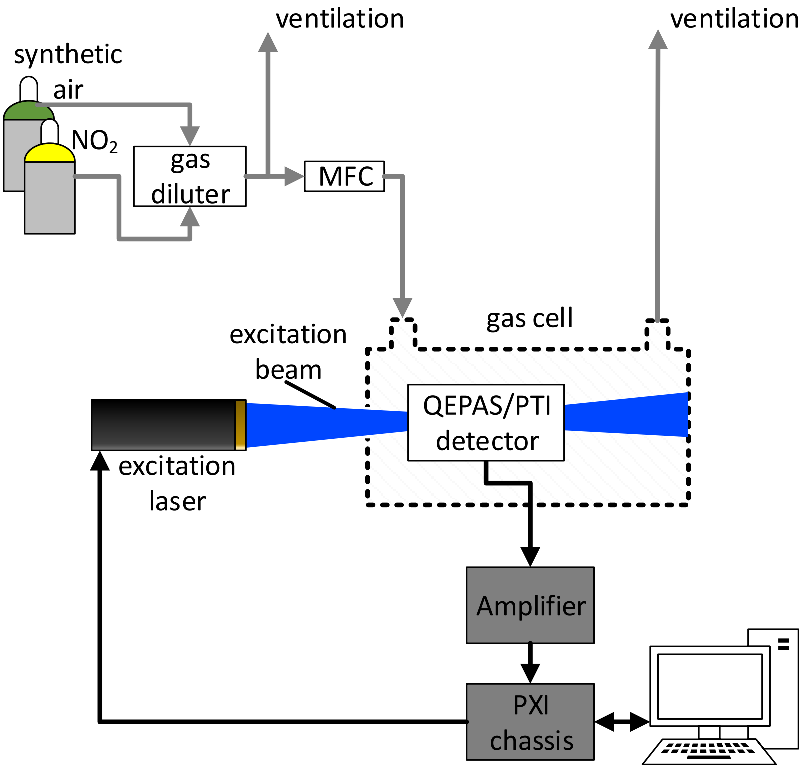

Fig. 3.2 Schematic of the experimental setup for characterizing the PTI and QEPAS setups with NO_2.

For the two setups, blue (450 nm) laser diodes were used (PTI: 40 mW peak optical power, QEPAS: 80 mW peak optical power). The square wave signal for amplitude modulation (50 % duty cycle) is provided by a function generator (National Instruments: Model PXI-5402). The PXI-5402 is contained in a chassis, which also carries a data acquisition card (National Instruments: Model PXI-6281). Both, the PXI-5402 and PXI-6281 share the same synchronization clock, which is necessary to correctly perform the lock-in amplifier calculations. The two-phase lock-in amplifier is realized as a custom LabVIEW application on a PC. Since the DAQ card only has a limited buffer size, and does not allow for continuous acquisition longer than 10 s, data acquisition and modulation is stopped and restarted synchronously after each measurement to obtain the same phase. The data acquisition rate of 250 kSps, together with the 1 s integration time, used for the measurements, leads to a bandwidth of approximately 0.88 Hz (cf. Figure 3.3).

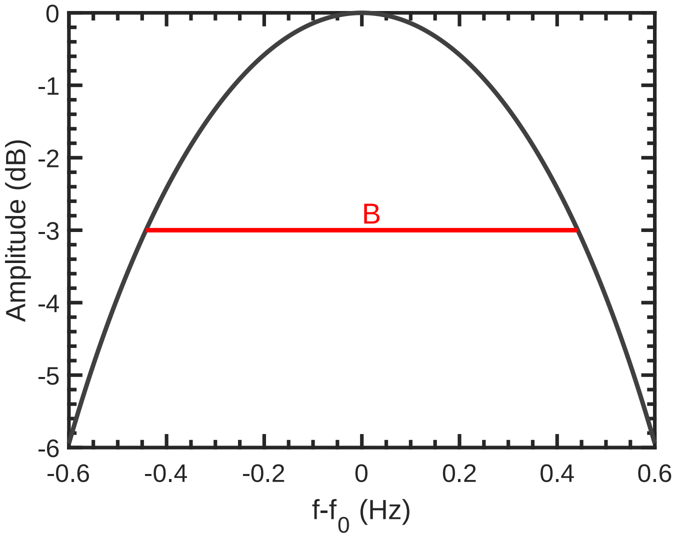

Fig. 3.3 Transfer function of the lock-in amplifier implementation simulated with MATLAB. The bandwidth (B) is approximately 0.88 Hz (−3 dB bandwidth).

3.2 Photothermal sensor

The sensing concept for the photothermal detection of NO_2 is described in **Paper 3**. The cell of the photothermal setup is shown in Figure 3.4. The 450 nm excitation beam (Laser Components GmbH, Olching, Germany: FLEXPOINT® Dot Laser Module) is directed through the fiber-coupled Fabry–Pérot interferometer (FPI) cavity of a commercial optical microphone (XARION Laser Acoustics GmbH, Vienna, Austria: Eta 250 Ultra). The FPI is formed by a machined opening with semitransparent mirror surfaces, each approximately 1.5 mm × 1.5 mm in size, which are facing parallel to each other at a distance of approximately 3.3 mm. The probe beam is horizontally centered to cross the probe laser of the optical microphone

(FWHM $\approx 205\,\mu$m) at the position of maximum intensity, when the overlap of probe- and excitation is a maximum.

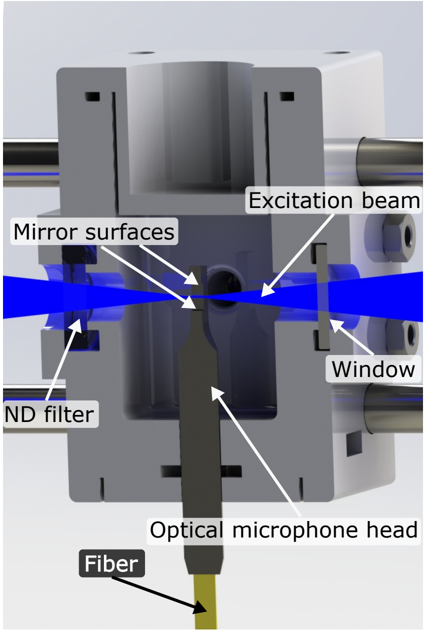

Fig. 3.4 Cut through the 3D-printed cell, carrying the head of the optical microphone. Excitation laser beam is shown in blue. The probe beam is reflected within the microphone cavity between the top and bottom mirror surfaces. The length of the cell is 34 mm. Figure from **Paper 3**.

The sample volume of the 3D-printed cell is smaller than $9\,\text{cm}^3$, but could be ultimately decreased to the volume of the FPI cavity, which is $1.5\,\text{mm} \times 1.5\,\text{mm} \times 3.3\,\text{mm} \approx 7.5\,\text{mm}^3$. Further, chip-level miniaturization of the sensor is possible, offering potential for large-scale production of the sensor.

Best results were achieved with a modulation frequency of 1.4 kHz and a flow rate of 0.5 slpm. Experiments with the gas diluter showed perfect linearity of the sensor (cf. Figure 3.5(a)). The 1σ detection limit is 348 ppb for 1 s averaging time. Allan deviation analysis (cf. Figure 3.5(b)) showed that it can be further improved down to 26 ppb (100 s averaging time). Drift increases noise significantly after 300 s[1]. Using higher laser powers or longer averaging times, enabled by a temperature stabilized laser source, would enable even lower detection limits. Furthermore, the detection limit could be improved with a different design of the cavity (cf. Chapter 2.1.5). A higher reflectivity of the FP mirrors would lead to a higher sensitivity of the interferometer [18]. Additionally, the detection limit could be improved with a design, which allows for a larger overlap of the excitation and the probe beam [18].

---

[1] In **Paper 3** it is shown that the increase in noise is caused by a fluctuation of the laser power.

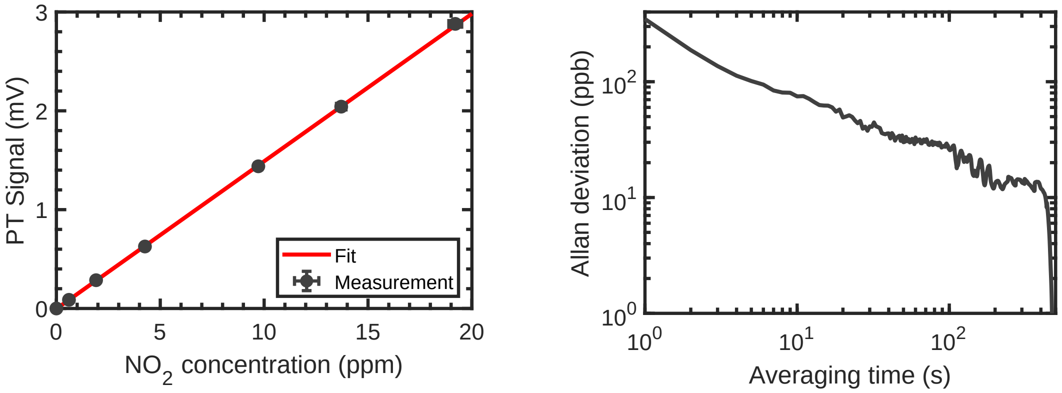

(a)

(b)

Fig. 3.5 **(a)** Linear fit (red) of the background-corrected photothermal signal as a function of the NO_2 concentration. Error bars of the photothermal signals are the standard deviation relative to the mean. Error bars of the concentrations are too small to be visible on this scale. Figure from **Paper 3**. **(b)** Allan deviation[2]of the photothermal signal in units of NO_2 concentration as a function of averaging time. Allan deviation was calculated with MATLAB.

The sensing concept was exposed to sinusoidal vibrations by an electrodynamic shaker, to investigate its robustness to vibration. Peak accelerations of 1.7 g could be applied to the setup, without significantly increasing signal noise. Thus, a sensor based on this technology could be used for mobile gas sensing and exhaust emission measurements. As the sensing concept does not rely on an acoustic resonator, sensing at different frequencies could be used to cancel out the effect by tonal ambient noise in real-world applications.

---

[2] Erroneously, in **Paper 3** the Allan deviation plot of the first submission is shown.

3.3 QEPAS sensor

The sensing concept for NO_2 sensing with bf QEPAS is described in **Paper 4**. The QEPAS cell is shown in Figure 3.6. Optics focus the light of the laser diode (OSRAM: PL 450B) between the prongs of a standard QTF (Fox Electronics: NC38LF). The focus of the laser beam is of 116 µm width. The 3D printed gas cell has a sample volume of dimensions 20.6 mm × 16 mm × 9.7 mm, which can easily be miniaturized to lower values. The cell, which also carries the two stage amplifier, is covered by aluminum tape, which is grounded for electronic shielding. An unshielded version of the cell resulted in signal fluctuations corresponding to ppm concentrations of NO_2. The two-stage amplifier was developed as part of this thesis. Different operational amplifiers were tested in transimpedance and differential voltage amplifier configurations. Best results were achieved with a transimpedance amplifier based on an *LTC6240HV* low noise operational amplifier with a feedback resistor of $R_f = 6.8\,\mathrm{M\Omega}$ with a 0.3 pF capacitor in parallel for stability reasons.

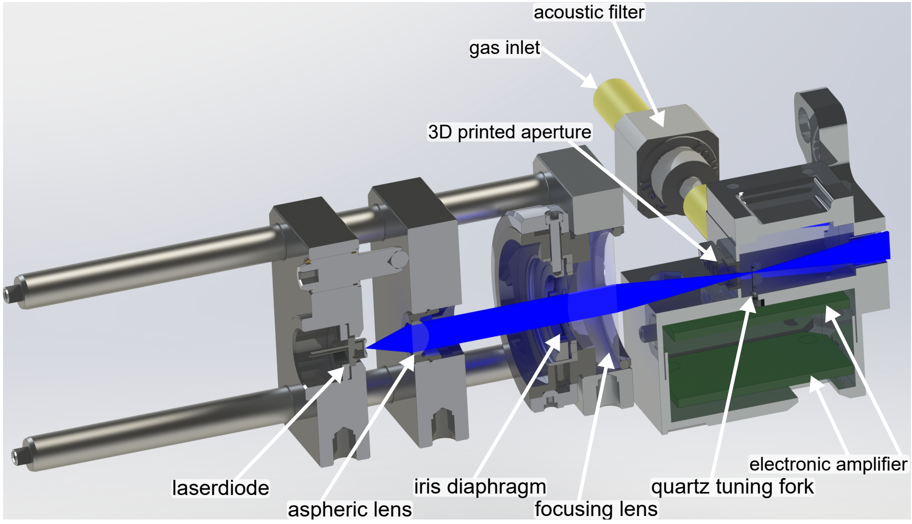

Fig. 3.6 Cut through the optical setup and the 3D-printed cell. Laser beam is shown in blue. The gas outlet is perpendicular to the inlet. Description of the elements can be found in the text. The distance from the laser diode mount to the back of the cell is ≈ 10 cm.

Experiments with the gas diluter showed perfect linearity of the sensor (cf. Figure 3.7(a)). The 1σ detection limit is 160 ppb for 1 s averaging time. Allan deviation analysis (cf. Figure 3.5(b)) showed the use of acoustic filters keeps the noise low and enables measurement times up to 120 s, which improves the detection limit to 21 ppb (120 s measurement time correspond to 80 s averaging time[3]). Similar to PTI, higher laser powers or longer averaging

---

[3] See **Paper 4** for a discussion of measurement time and averaging time of the QEPAS setup.

times, enabled by temperature stabilized laser source, would enable even lower detection limits.

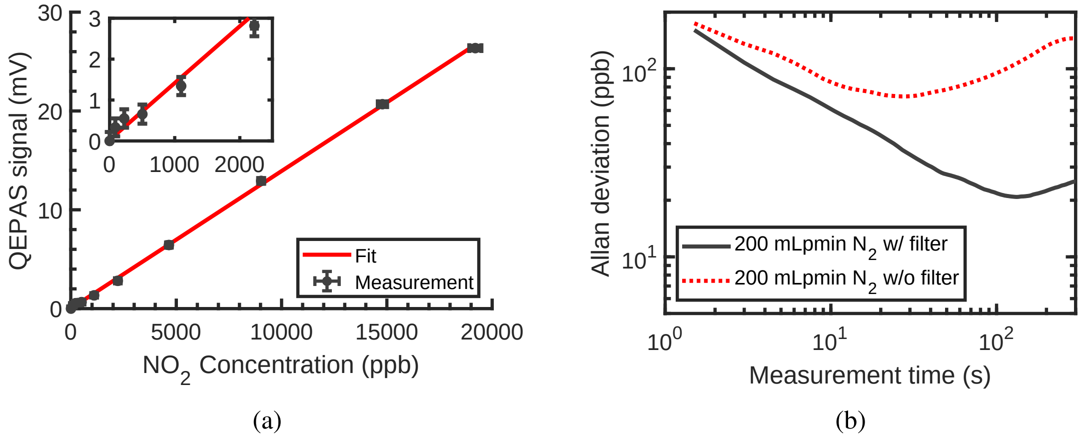

(a) (b)

Fig. 3.7 **(a)** Linear fit (red) of the background corrected photoacoustic signal as a function of the NO$_2$ concentration. Errorbars of the QEPAS signals are the standard deviation of the recorded values. Errorbars of the concentrations show the standard deviation calculated with GUM Workbench. Figure adopted from **Paper 4**. **(b)** Allan deviation of the photoacoustic signal with (w/) and without (w/o) acoustic filters as a function of the measurement time (1.5 s measurement time corresponds to 1 s averaging time). See **Paper 4** for more details. Figure adopted from **Paper 4**.

Photoacoustic sensors are sensitive to changes of temperature, pressure and gas composition. Since a QTF is a mechanical resonator, it is affected differently than an acoustic resonator used in conventional PAS or resonant signal amplificantion setups in QEPAS, such as off-beam QEPAS. In **Paper 4** it is shown that the developed bare fork setup is more robust to changes of environmental conditions such as humidity and temperature than off-beam configurations of QEPAS. Temperature changes can be accounted for with adoption of the laser modulation frequency. Corrections for humidity influences are possible by using a simplified model, taking into account only a humidity sensor reading.

After a temperature change has been detected, the change in resonance frequency should be quickly detected. A fast method to track the frequency change in PAS methods is the CHIRP method, which was presented for QEPAS by the author of this thesis [17]. Within 0.5 s the resonance frequency can be determined with 0.3 Hz standard deviation. Details can be found in Appendix A.4.

3.4 Discussion

Table 3.1 shows a comparison of the two sensing concepts developed in this thesis[4] with other works described in literature. It can be seen, that both developed sensing concepts have a one or two orders of magnitude worse noise normalized equivalent absorption coefficient (NNEA) than the PAS and off-beam (ob) QEPAS concepts reported in literature. However, for averaging times on the order of 100 s, both presented sensing concepts are able to calculate each index class of the common air quality index (cf. Table 1.2), which is sufficient for citizen information purposes. It must be noted here, that assuming the minimum value of the Allan deviation as detection limit is only a theoretical value, which is frequently used in literature. However, as noted by Werle et al. [112] a measuring cycle consists of the measurement of the sample and background signal as well as gas exchange in the cell. Neglecting the gas exchange time due to the small sample volumes, a measurement cycle of twice the sample measurement time should be assumed. Since drift occurs later than 200 s in the PTI concept, 100 s averaging time seems to be justified. In the case of the QEPAS concept, drift causes the detection limit to increase slightly from 21 ppb to 23.5 ppb for twice the sample measurement time (240 s).

In contrast to PAS setups, both, the PTI and bf QEPAS sensing concepts have a high miniaturization potential. This is advantageous in terms of cost, since size typically scales with cost. In contrast to ob QEPAS setups, both presented concepts enable easier laser alignment and are thus more suitable for mass production. To overcome temperature and humidity influences in ob QEPAS, a conditioning system could be used, but at the cost of a larger size, larger power consumption and higher cost, which are undesirable in low-cost sensing. In contrast, as only a single resonator (QTF or FPI) is used, both concepts allow easier adoption to changes of temperature, gas composition or pressure. Relative to the laser power, the PTI setup can reach lower detection limits for similarly long averaging times than the bf QEPAS setup. This is attributed to the well-engineered stabilization control-loop of the commercial optical microphone.

---

[4] In **Paper 3** an NNEA of $7.5 \times 10^{-8}\,\mathrm{W/cmHz^{1/2}}$ is reported because Δf was assumed to be 1 Hz instead of 0.88 Hz.

Table 3.1 Comparison of the two NO_2 sensing concepts developed within this thesis with selected literature values of PTI, PAS and QEPAS. Limits of detection (LOD) are given for synthetic air (S.A.) or nitrogen (N_2) as dilution gas for 1 s and the maximum reported averaging time. Also the noise normalized equivalent absorption coefficient (NNEA) is given.

Work	**Method**	**Diluent**	**1 σ LOD for** 1 s **(ppb)**	**1 σ LOD for max. int. time (ppb)**	**NNEA** ($cm^{-1}W/\sqrt{Hz}$)
Paper 3	PTI	S.A.	348	26 (100 s)	8.0×10^{-8}
Paper 4	bf QEPAS	S.A.	160	21 (80 s)	8.6×10^{-8}
[124]	PAS	S.A.	0.054		1.6×10^{-9}
[90]	PAS	S.A.		0.033 (20 s)	7.0×10^{-10}
[91]	ob QEPAS	S.A.		0.6 (20 s)	2.5×10^{-8}
[129]	ob QEPAS	N_2	1.3		4.2×10^{-9}
[122]	ob QEPAS	N_2	18	4.4 (20 s)	4.1×10^{-9}
[18]	PTI	N_2	700		1.3×10^{-7}

Chapter 4

Black carbon sensing concept

4.1 Introduction

Photoacoustic instruments for soot measurement typically use an intensity modulated light source to transfer energy to soot particles [86]. Wavelength modulation is not possible, due to the broad absorption spectrum of soot, which does not exhibit distinct peaks (cf. Figure 3.1).

Light absorption by the particle leads to a temperature increase of that particle. Subsequently, heat is transferred to the surrounding air, which, due to modulation of the light source, results in an acoustic wave with a frequency that matches the modulation of the light source [74]. For typical soot particles with diameters $d \leq 100\,\mathrm{nm}$, and a conventional photoacoustic cell with 1.5 kHz modulation frequency, the amplitude of the acoustic wave is directly proportional to the absorbed light energy [74].

Energy transferred to the particle leads to (a) conductive dissipation (photoacoustic signal), (b) mass flux due to evaporation (less efficiently producing a photoacoustic signal [74]), and (c) heating and cooling of the particle [22]. The energy flux $E(t,\omega)$ to the particle, due to sinusoidal modulation $E(t,\omega) = E_0\left(e^{-i\omega t}+1\right)$ is thus given by [22]

$$E(t,\omega) = Q(r,T_a) + I(r,T_a)\cdot L + m_a c_{p,a}\frac{\partial T_a}{\partial t}, \tag{4.1}$$

with $Q(r,T_a)$ the conductive dissipation, $I(r,T_a)\cdot L$ the mass flux away from the particle times the latent heat, and $m_a c_{p,a}$ the mass times the specific heat of the particle which multiplied by $\frac{\partial T_a}{\partial t}$ describes heating and cooling of the particle of temperature T_a. The conductive dissipation part is described by [22]

$$Q(r,T_a) = 4\pi r\kappa(T_a - T_\infty), \tag{4.2}$$

with r the particle radius, κ the heat conductivity of the surrounding gas and T_∞ the ambient temperature. The mass flux $I(r,T_a)$ is described by [22]

$$I(r,T_a) = 4\pi rDM_V(x_a - x_\infty), \tag{4.3}$$

with D the diffusion constant of the evaporating species, M_V the molar mass of the evaporating species, and $(x_a - x_\infty)$ the difference in molar concentration of the evaporating species at the surface of the particle and far from the particle.

For the photoacoustic signal of spherical particles, an efficiency, similar to that describing delayed molecular relaxation in gas PAS (cf. Equation (2.2)) can be stated [22]:

$$\eta_a = \frac{1}{\sqrt{(1+f_M)^2 + (2\pi f_0 \tau(r))^2}}, \tag{4.4}$$

where $f_M = \Delta I \cdot L/\Delta Q$ describes the ratio of the oscillating components of latent heat flux (evaporation; mass flux multiplied with latent heat) to sensible heat flux ΔQ (conductive dissipation), and $\tau(r) = r^2\rho_a c_{p,a}/(3\kappa)$ is the time constant due to the thermal inertia of the particle. Here, r is the radius, ρ_a the density and $c_{p,a}$ the heat capacity of the particle, and κ the heat conductivity of the surrounding gas.

Due to the acoustic signal lost by evaporation, Moosmüller et al. [74] suggests to dry the aerosol before measuring it with photoacoustic soot sensors and Arnott et al. [9] recommends to keep relative humidity below 65 %. Furthermore, the properties of different forms of soot may vary, which makes it necessary to use different calibration factors to correctly relate the photoacoustic signal to a mass concentration [38].

4.2 QEPAS sensor

The sensing concept for sensing of soot with bf-QEPAS is described in **Paper 5**. The QEPAS cell for soot measurements, which is milled from aluminum, is shown in Figure 4.1. A 30 mW optical power FLEXPOINT® Dot Laser Module (Laser Components GmbH) with 850 nm wavelength was chosen, as it has minimal spectroscopic cross-interference to any gases possibly contained in ambient or combustion related aerosol. Optics focus the light of the laser between the prongs of the standard QTF (Fox Electronics: NC38FL), which is positioned in a cylindrical sample volume. The aerosol in- and outlet to the cell are positioned perpendicular to the laser beam direction. A design with two opposing in- and outlets was chosen to minimize contamination of the cell windows. Sealing rings ensure a gas tight design, such that the sample can be drawn by connecting a pump to the aerosol outlets.

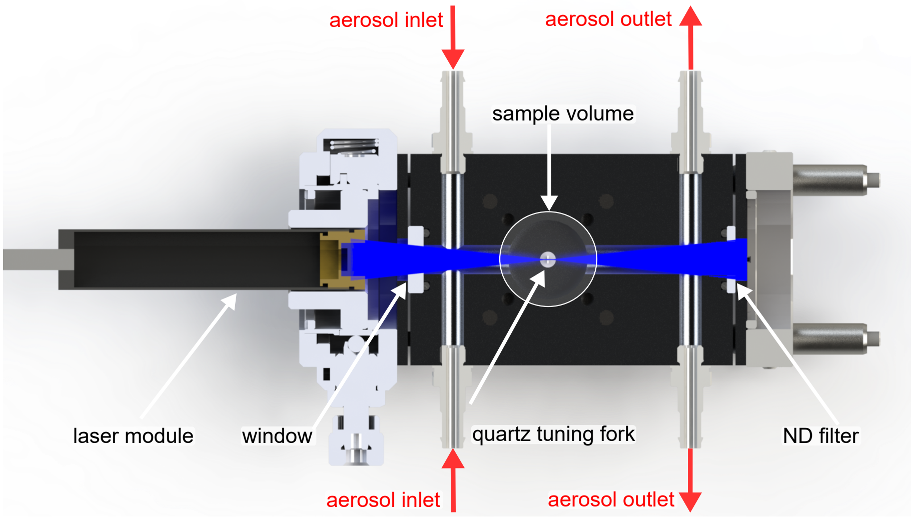

Fig. 4.1 Horizontal cut through the cell. Directions of sample flow are indicated with arrows. Laser beam is shown in blue. The gas outlet is perpendicular to the inlet. Description of the elements can be found in the text. The length of the cell (solid aluminum part) is 65 mm.

The QEPAS signal is amplified with a similar two-stage amplifier as it was developed for **Paper 4**. Also, the lock-in amplifier implementation is the same (cf. Section **Paper 4**). The experimental setup is shown in Figure 4.2. The soot aerosol was generated with a miniCAST soot generator (Jing Ltd: Model 6204 Type B). To generate different soot concentrations a dilution bridge was used, which consists of a HEPA filter in parallel with a needle valve. The aerosol passed through the organ-like cell of a Micro Soot Sensor (MSS; AVL LIST GmbH) at a flow rate of 2 std L min^{-1}. To ensure the QEPAS cell measures the same particles as the MSS, the QEPAS cell was set in series to the PAS cell of the MSS. The flow rate through the QEPAS cell was fixed to 200 std $\mathrm{cm}^3\,\mathrm{min}^{-1}$ by means of a massflow controller (MFC; Vögtlin: Model GSC-B). The aerosol was also characterized using an SMPS (TSI Inc.: Model 3938).

Figure 4.3(a) shows good agreement of the QEPAS signal with the mass concentration of soot measured by the MSS. Each datapoint has a different color, which corresponds to the mobility size distribution shown in the inset of Figure 4.3(a). Throughout the measurements, the geometric mean diameter increased from 49 nm for the lowest concentration to 78 nm

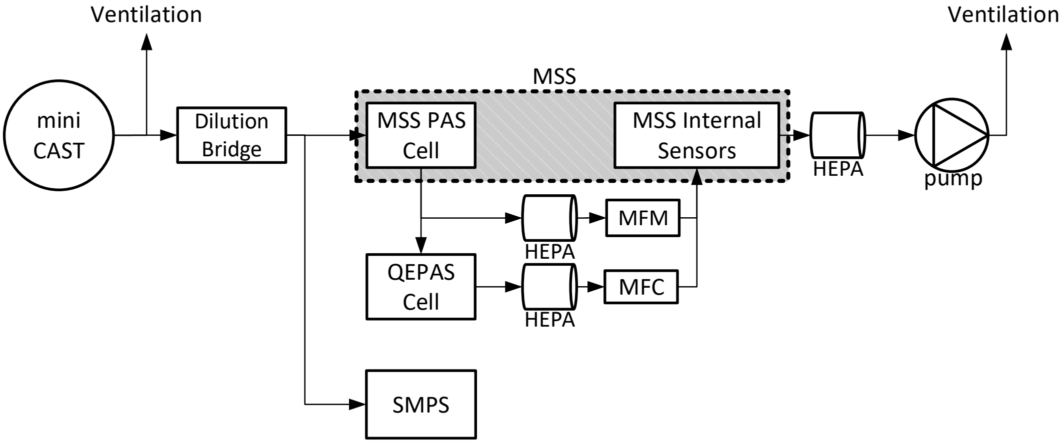

Fig. 4.2 Setup to measure the linearity of the QEPAS cell. Figure from **Paper 5**.

when the dilution bridge was at the lowest dilution and fully open. Allan deviation analysis (Figure 4.3(b)) showed that the 1σ noise can be improved to $\approx 25\,\mu\mathrm{g\,m^{-3}}$ for an averaging time of 19 s (cf. Chapter 3.4 for a discussion on the restrictions imposed by the duration of the measurement cycle).

4.3 Discussion

Commercial photoacoustic based instruments for measuring soot concentrations of vehicle exhaust reach detection limits better than $5\,\mu\mathrm{g\,m^{-3}}$ for 1 s averaging time [10, 38], which is a typical value for ambient air pollution (an average concentration of $6.6\,\mu\mathrm{g\,m^{-3}}$ and peak values of $49\,\mu\mathrm{g\,m^{-3}}$ are reported by Hamasha and Arnott [40]). However, the high cost, size and weight of conventional PAS systems (e.g. AVL Micro Soot Sensor [MSS]: $W \times H \times D = 483\,\mathrm{mm} \times 400\,\mathrm{mm} \times 555\,\mathrm{mm}$, $m \approx 26\,\mathrm{kg}$) has limited its applicability for widespread use in ambient or environmental monitoring. In contrast, the presented sensing concept could enable a reduction of size, mass and price by at least a factor of 50. E.g., within **Master thesis 2** co-supervised by the author of this work, a miniaturized electronic solution containing a lock-in amplifier and microcontroller was developed [49]. **Master thesis 3** showed that similar results as the National Instruments based solution could be achieved with a custom electronic solution, which can fit the palm of a hand.

Finally, it needs to be mentioned that the experiments described above were performed with a low power laser module, resulting in only moderate detection limits. Nevertheless by increasing the laser power to e.g. 500 mW, we expect the limit of detection to be lowered to

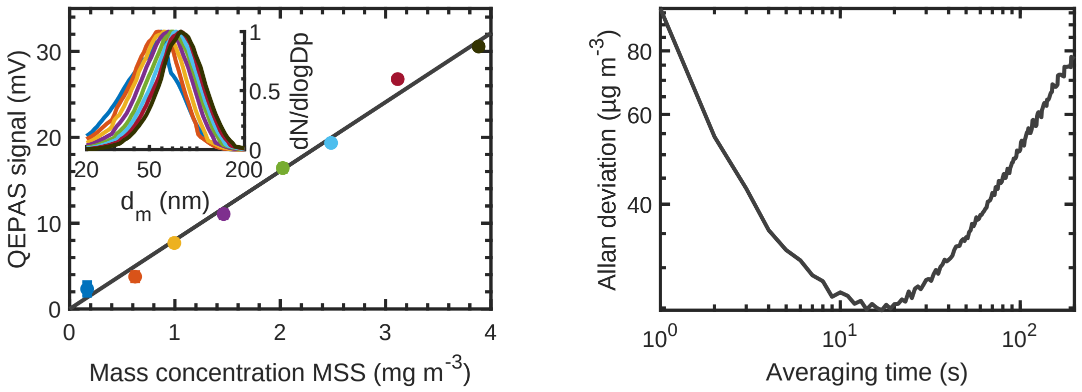

(a)

(b)

Fig. 4.3 **(a)** QEPAS signal in mV as a function of the mass concentration of soot particles measured by the micro-soot sensor (MSS). Error bars in the QEPAS signal represent the standard error relatively to the mean. Error bars for the mass concentrations as measured by the MSS are too small to be visible on this scale. The inset shows the measured and normalized size distributions (mobility diameter d_m) with colors corresponding to each point. The best fit line assumes identical zero offsets at zero. Figure adopted from **Paper 5**. Figure adopted from **Paper 5**. **(b)** Allan deviation of the QEPAS sensor as a function of averaging time when using suction by a nozzle of ambient, filtered air. Figure adopted from **Paper 5**.

4.5 µg m^{-3} for 1 s averaging time without increasing the overall sensor size (cf. Appendix A.1 for a discussion on the higher laser power).

Chapter 5

Conclusions and Outlook

In this thesis, sensing concepts were developed and characterized, which bear the potential of low-cost sensing of air pollutants at sufficient accuracy to measure exceedances of air quality limit values. Due to their potentially small size and cost, such sensors could be used in conjunction with (wireless) sensor networks to enable sensing of pollutants at both, high spatial and temporal resolution.

In the beginning, a review on sensor networks for air pollution was carried out (**Paper 1**). Although a high number of projects for the purpose of pollution monitoring with networks exist, insufficient sensing technology was identified as the bottleneck.

Usually, electrochemical or metal oxide based sensors are used in these projects, which suffer from cross-interference to other analytes, long-term drift and dependence on environmental conditions, thereby having exhibiting strong inter-defice variance. In contrast, optical sensors allow specific sensing of analytes. Due to the versatility and simplicity of optothermoacoustic spectroscopy methods, it was decided to investigate these methods further. To evaluate the developed sensing concepts, a precise gas diluter based on binary weighted critical orifices was designed, built and verified, as described in **Paper 2**. The gas diluter is able to produce gas mixtures at a high dynamic range (1 : 1400) and low uncertainty (1.9% for the lowest concentration, including the uncertainty of the gas mixture).

Two optothermoacoustic sensing concepts for the detection of NO_2 were developed. For the maximum averaging time, both sensing concepts are able to calculate each index class of the common air quality index (cf. Table 1.2), which is sufficient for citizen information purposes. The quartz-enhanced photoacoustic spectroscopy-based sensor, described in **Paper 4**, is robust to changes of environmental conditions such as humidity and temperature. Temperature changes can be accounted for with adoption of the laser modulation frequency and a simple model. Corrections for humidity influences are possible by using a simplified model, taking into account only a humidity sensor reading. Theoretical calculations (cf. Section 2.2.2) show that the detection limit of the QEPAS sensor is close to its minimum possible value. The theoretical model also shows, that better detection limits could be achieved with resonators, which are shaped such that the resonator's eigenmode has a higher overlap integral with the photoacoustically generated wave.

Due to the use of acoustic filters, the measurement time can be as long as 120 s, where a theoretical 1σ detection limit of 21 ppb can be achieved. Further improvement is possible with higher laser powers or stabilized sources, to allow longer averaging times.

The second sensing concept for NO_2, a photothermal interferometry-based approach, is described in **Paper 3**. The sensor consists of a fiber-coupled Fabry–Pérot interferometer, which has shown to be robust against vibration with peak accelerations of 1.7 g. The 1σ detection limit for 100 s is 26 ppb. Similar to the QEPAS concept, higher laser powers and longer averaging times can improve the detection limit. Furthermore, a different design of the cavity, with higher finesse and larger overlap of the excitation and the probe beam would improve the detection limit without increasing the excitation laser power.

One of the advantages of optothermoacoustic methods is their color-blindness, meaning that only the excitation laser wavelength needs to be changed, in order to detect other analytes (pollutants).

The QEPAS sensor was adopted to be able to measure black carbon concentrations (**Paper 5**). A cell, appropriate for the measurement of soot particles was designed. The achieved 1σ detection limit is 25 $\mu g\,m^{-3}$ for an averaging time of 19 s. This is a relatively high value, which might only be measured in heavily polluted areas (peak concentrations of 49 $\mu g\,m^{-3}$ are reported for the city of Irbid, Jordan [40]). However, with 500 mW optical power the limit of detection is expected to be lowered to 4.5 $\mu g\,m^{-3}$ without increasing the overall sensor size. A size dependency of the photoacoustic signal could not be seen, but its study with larger soot particle should be emphasized in future investigations.

The photothermal measurement of aerosols by a Fabry–Pérot interferometer is expected to be feasible, since photothermal interferometry for soot has been demonstrated for a different type of interferometer [99, 98]. However, a sheath flow concept, which is only possible with a larger cavity, would be necessary for the sensor concept discussed in **Paper 3**, in order to avoid degradation of the mirror reflectivity. Size dependency of aerosols could be nicely investigated with a PTI-based approach, as it allows the study of the photothermal signal at different modulation frequencies.

If QEPAS is used in conjunction with a multi wavelength photodiode it would have great potential as a low-cost multi-pollutant air quality sensing technology. Engineering challenges that would arise include the development of a production process, which allows simple mounting of the QTF and automatic beam alignment. This is easiest achievable for the presented bare fork configuration.

More challenges, but even bigger potential is given for a chip-miniaturized PTI sensor. Detection limits relative to the excitation power are expected to be at least an order of magnitude better as compared to QEPAS, if the excitation beam is alligned parallel to the probe beam and the mirror reflectivity is increased.

It is expected, that cities will introduce networks of air quality sensors in conjunction with cameras, to increase the city toll based on the current pollution level and place, i.e., driving a vehicle at peak times when the pollution is high, will be connected to higher cost for the vehicle drivers (cf. [30]). Also, the sensor readings will be provided to the citizens for informational purposes. For this scenario, the presented methods would be ideally suited.

While the measurement of gaseous components is relatively straightforward, for the measurement of aerosol, such as BC, a better understanding of the signal generation will be necessary. Nevertheless, as the awareness for the adverse health effects of ultrafine particles and particularly soot increases, methods to specifically measure those at low cost will be of high interest. For this purpose, further investigation and development of optothermoacoustic methods should be promoted.

References

[1] Abramowitz, M. (1970). *Handbook of mathematical functions*. Washington, D.C., 9 edition.

[2] Agency, E. E. (2014). *Air quality in Europe - 2014 report*.

[3] Airyx GmbH (2019). Datasheet ICAD NO2 NOx NO Monitor.

[4] Alphasense Ltd. (2019). OPC-N3 Particle Monitor Technical Specification.

[5] Amaral, S. S., de Carvalho, J. A., Costa, M. A. M., and Pinheiro, C. (2015). An overview of particulate matter measurement instruments. *Atmosphere*, 6(9):1327–1345.

[6] Aoust, G., Levy, R., Raybaut, M., Godard, A., Melkonian, J.-M., and Lefebvre, M. (2017). Theoretical analysis of a resonant quartz-enhanced photoacoustic spectroscopy sensor. *Applied Physics B*, 123(2):1–11.

[7] Apte, J. S., Messier, K. P., Gani, S., Brauer, M., Kirchstetter, T. W., Lunden, M. M., Marshall, J. D., Portier, C. J., Vermeulen, R. C., and Hamburg, S. P. (2017). High-Resolution Air Pollution Mapping with Google Street View Cars: Exploiting Big Data. *Environmental Science & Technology*, 51(12):6999–7008.

[8] AQMesh Environmental Instruments Ltd (2016). Aqmesh. [online] http://www.aqmesh.com/.

[9] Arnott, W. P., Moosmüller, H., Sheridan, P. J., Ogren, J. A., Raspet, R., Slaton, W. V., Hand, J. L., Kreidenweis, S. M., and Collett Jr., J. L. (2003). Photoacoustic and filter-based ambient aerosol light absorption measurements: Instrument comparisons and the role of relative humidity. *Journal of Geophysical Research*, 108:4034–4044.

[10] AVL List GmbH (2018). Avl Micro Soot Sensor Operating Manual, Rev. 14.

[11] Besson, J.-P. (2006). *Photoacoustic spectroscopy for multi-gas sensing using near infrared lasers*. PhD thesis, ÉCOLE POLYTECHNIQUE FÉDÉRALE DE LAUSANNE.

[12] Bialkowski, S. E., Astrath, N. G. C., and Proskurnin, M. A. (2019). *Photothermal Spectroscopy Methods*. Wiley, 2nd edition.

[13] Borri, S., Patimisco, P., Galli, I., Mazzotti, D., Giusfredi, G., Akikusa, N., Yamanishi, M., Scamarcio, G., De Natale, P., and Spagnolo, V. (2014). Intracavity quartz-enhanced photoacoustic sensor. *Applied Physics Letters*, 104(9):091114.

[14] Borri, S., Patimisco, P., Sampaolo, A., Beere, H. E., Ritchie, D. A., Vitiello, M. S., Scamarcio, G., and Spagnolo, V. (2013). Terahertz quartz enhanced photo-acoustic sensor. *Applied Physics Letters*, 103(2).

[15] Böttger, S., Köhring, M., Willer, U., and Schade, W. (2013). Off-beam quartz-enhanced photoacoustic spectroscopy with LEDs. *Applied Physics B*, 113(2):227–232.

[16] Bozóki, Z., Pogány, A., and Szabó, G. (2011). Photoacoustic instruments for practical applications: Present, potentials, and future challenges. *Applied Spectroscopy Reviews*, 46(1):1–37.

[17] Breitegger, P., Lang, B., and Bergmann, A. (2018). A new Method to Determine the Resonance Frequency in QEPAS. In *2018 Conference on Lasers and Electro-Optics (CLEO)*, pages 1–2, San Jose, CA. OSA.

[18] Campillo, A. J., Petuchowski, S. J., Davis, C. C., and Lin, H. B. (1982). Fabry-perot photothermal trace detection. *Applied Physics Letters*, 41(4):327–329.

[19] Carras, M., Brun, M., Fedeli, J.-M., Coutard, J.-G., Duraffourg, L., Maisons, G., Aoust, G., Nicoletti, S., and Abautret, J. (2018). Quantum Cascade Laser Integration on Silicon for Gas Sensing. In *2018 IEEE Photonics Society Summer Topical Meeting Series (SUM)*, pages 233–234. IEEE.

[20] Castell, N., Dauge, F. R., Schneider, P., Vogt, M., Lerner, U., Fishbain, B., Broday, D., and Bartonova, A. (2017). Can commercial low-cost sensor platforms contribute to air quality monitoring and exposure estimates? *Environment International*, 99:293–302.

[21] CITI-SENSE (2019). Citi-sense social networking platform. [online] http://co.citi-sense.eu.

[22] Cremer, J. W., Covert, P. A., Parmentier, E. A., and Signorell, R. (2017). Direct Measurement of Photoacoustic Signal Sensitivity to Aerosol Particle Size. *Journal of Physical Chemistry Letters*, 8(14):3398–3403.

[23] Davis, C. C. and Petuchowski, S. J. (1981). Phase fluctuation optical heterodyne spectroscopy of gases. *Applied Optics*, 20(14):2539.

[24] Dong, L., Kosterev, A. A., Thomazy, D., and Tittel, F. K. (2010). QEPAS spectrophones: design, optimization, and performance. *Applied Physics B*, 100(3):627–635.

[25] Dong, L., Lewicki, R., Liu, K., Buerki, P. R., Weida, M. J., and Tittel, F. K. (2012). Ultra-sensitive carbon monoxide detection by using EC-QCL based quartz-enhanced photoacoustic spectroscopy. *Applied Physics B: Lasers and Optics*, 107(2):275–283.

[26] Dong, L., Wu, H., Zheng, H., Liu, Y., Liu, X., Jiang, W., Zhang, L., Ma, W., Ren, W., Yin, W., Jia, S., and Tittel, F. K. (2014). Double acoustic microresonator quartz-enhanced photoacoustic spectroscopy. *Optics Letters*, 39(8):2479.

[27] Droplet Measurement Technologies (2019). PAX Photoacoustic Excinctometer Datasheet.

[28] Duquesnoy, M., Aoust, G., Melkonian, J.-M., Lévy, R., Raybaut, M., and Godard, A. (2019). Quartz Enhanced Photoacoustic Spectroscopy Based on a Custom Quartz Tuning Fork. *Sensors*, 19(6):1362.

[29] Elia, A., Lugarà, P. M., Di Franco, C., and Spagnolo, V. (2009). Photoacoustic Techniques for Trace Gas Sensing Based on Semiconductor Laser Sources. *Sensors*, 9(12):9616–9628.

[30] European Commission (2020). CARES: City Air Remote Emission Sensing. [online] https://trimis.ec.europa.eu/project/city-air-remote-emission-sensing.

[31] European Environment Agency (2015). SOER 2015 European briefings Air pollution.

[32] European Environment Agency (2018). Unequal exposure and unequal impacts: social vulnerability to air pollution, noise and extreme temperatures in Europe. Technical report, European Environment Agency, Luxembourg.

[33] European Parliament and Council of the European Union (2008). Directive 2008/50/EC of the European Parliament and of the Council of 21 May 2008 on ambient air quality and cleaner air for Europe.

[34] Faxvog, F. R. and Roessler, D. M. (1979). Optoacoustic measurements of diesel particulate emissions. *Journal of Applied Physics*, 50(12):7880–7882.

[35] Firebaugh, S. L., Roignant, F., and Terray, E. a. (2009). Modeling the Response of Photoacoustic Gas Sensors. *Comsol*, (1).

[36] Firebaugh, S. L., Roignant, F., and Terray, E. A. (2010). Enhancing sensitivity in tuning fork photoacoustic spectroscopy systems. In *2010 IEEE Sensors Applications Symposium (SAS)*, pages 30–35. IEEE.

[37] Gasera Ltd. (2019). Photoacoustic Detector: PA201 Datasheet.

[38] Giechaskiel, B., Maricq, M., Ntziachristos, L., Dardiotis, C., Wang, X., Axmann, H., Bergmann, A., and Schindler, W. (2014). Review of motor vehicle particulate emissions sampling and measurement: From smoke and filter mass to particle number. *Journal of Aerosol Science*, 67:48–86.

[39] Gillispie, G. D. and Khan, A. U. (1976). The electronic structure of NO 2. II. The X 2 B 2 ← ? 2 A 1 and X 2 B 1 ←X 2 A 1 absorption systems. *The Journal of Chemical Physics*, 65(5):1624–1633.

[40] Hamasha, K. M. and Arnott, W. P. (2010). Photoacoustic measurements of black carbon light absorption coefficients in Irbid city, Jordan. *Environmental Monitoring and Assessment*, 166(1-4):485–494.

[41] Hasenfratz, D., Saukh, O., Walser, C., Hueglin, C., Fierz, M., Arn, T., Beutel, J., and Thiele, L. (2015). Deriving high-resolution urban air pollution maps using mobile sensor nodes. *Pervasive and Mobile Computing*, 16(PB):268–285.

[42] Hidalgo, M. D. (2019). Rescatame - pervasive air-quality sensors network for an environmental friendly urban traffic management life08. [online] http://ec.europa.eu/environment/life/project/Projects/index.cfm?fuseaction=home.createPage&s_ref=LIFE08ENV/E/000107&area=2&yr=2008&n_proj_id=3485&cfid=99964&cftoken=663312df0d288b39-D234793A-C9C4-FE9F-153DC2F00E945D0D&mode=print&menu=false.

[43] Horbanski, M., Pöhler, D., Lampel, J., and Platt, U. (2019). The ICAD (iterative cavity-enhanced DOAS) method. *Atmospheric Measurement Techniques*, 12(6):3365–3381.

[44] Huber, J., Ambs, A., and Wöllenstein, J. (2015). Miniaturized photoacoustic carbon dioxide sensor with integrated temperature compensation for room climate monitoring. *Procedia Engineering*, 120:283–288.

[45] Infineon Technologies AG (2019). Environmental Sensors. [online] https://www.infineon.com/cms/en/product/sensor/environmental-sensors-/?redirId=106203.

[46] Kalkman, J. and van Kesteren, H. (2008). Relaxation effects and high sensitivity photoacoustic detection of NO2 with a blue laser diode. *Applied Physics B*, 90(2):197–200.

[47] Kapp, J., Weber, C., Schmitt, K., Pernau, H.-F., and Wöllenstein, J. (2019). Resonant Photoacoustic Spectroscopy of NO2 with a UV-LED Based Sensor. *Sensors*, 19(3):724.

[48] Karlsson, H. and Sinisalo, S. (2017). Air Quality Monitoring with Photoacoustic Spectroscopy. *Optik & Photonik*, 12(1):36–39.

[49] Kerschhofer, A., Breitegger, P., and Bergmann, A. (2018). Laser Driver and Analysis Circuitry Development for Quartz-Enhanced Photoacoustic Spectroscopy of NO2 for IoT Purpose. *Proceedings*, 2(13):1062.

[50] Köhring, M., Böttger, S., Willer, U., and Schade, W. (2013). Temperature effects in tuning fork enhanced interferometric photoacoustic spectroscopy. *Optics Express*, 21(18):20911.

[51] Kosterev, A. A., Bakhirkin, Y. A., Curl, R. F., and Tittel, F. K. (2002). Quartz-enhanced photoacoustic spectroscopy. *Optics Letters*, 27(21):1902.

[52] Kosterev, A. A., Tittel, F. K., Serebryakov, D. V., Malinovsky, A. L., and Morozov, I. V. (2005). Applications of quartz tuning forks in spectroscopic gas sensing. *Review of Scientific Instruments*, 76(4):043105.

[53] Kreyszig, E. (1993). *Advanced engineering mathematics*. John Wiley & Sons Inc, 7th edition.

[54] Krzempek (2019). A Review of Photothermal Detection Techniques for Gas Sensing Applications. *Applied Sciences*, 9(14):2826.

[55] Kuempel, E. D. and Sorahan, T. (2010). Identification of Research Needs to Resolve the Carcinogenicity of High-priority IARC Carcinogens: Views and Expert Opinions of an IARC/NORA Expert Group Meeting. *IARC Technical Publication*, 42:61 – 72.

[56] Kumar, D., Gupta, S., Kumar, S., Sharma, R. C., and Soni, R. K. (2016). Open-path measurement of ozone and methane gases using quartz-enhanced photoacoustic spectroscopy. *Spectroscopy Letters*, 49(7):469–476.

[57] Landrigan, P. J. (2017). Air pollution and health. *The Lancet Public Health*, 2(1):e4–e5.

[58] Lang, B., Breitegger, P., Brunnhofer, G., Valero, J. P., Schweighart, S., Klug, A., Hassler, W., and Bergmann, A. (2020). Molecular relaxation effects on vibrational water vapor photoacoustic spectroscopy in air. *Manuscript submitted for publication.*

[59] Levy, R., Duquesnoy, M., Aoust, G., Melkonian, J. M., and Raybaut, M. (2019). New signal processing for fast and precise QEPAS measurements. *IEEE Transactions on Ultrasonics, Ferroelectrics, and Frequency Control*, PP(c):1–1.

[60] Libelium Comunicaciones Distribuidas S.L. (2019). Libelium - smart city project in salamanca to monitor air quality and urban traffic with waspmote. [online] http://www.libelium.com/smart_city_air_quality_urban_traffic_waspmote/.

[61] Lindley, R. E., Parkes, A. M., Keen, K. A., McNaghten, E. D., and Orr-Ewing, A. J. (2007). A sensitivity comparison of three photoacoustic cells containing a single microphone, a differential dual microphone or a cantilever pressure sensor. *Applied Physics B: Lasers and Optics*, 86(4):707–713.

[62] Liu, K., Guo, X., Yi, H., Chen, W., Zhang, W., and Gao, X. (2009). Off-beam quartz-enhanced photoacoustic spectroscopy. *Optics Letters*, 34(10):1594.

[63] Liu, K., Yi, H., Kosterev, A. A., Chen, W., Dong, L., Wang, L., Tan, T., Zhang, W., Tittel, F. K., and Gao, X. (2010). Trace gas detection based on off-beam quartz enhanced photoacoustic spectroscopy: Optimization and performance evaluation. *Review of Scientific Instruments*, 81(10):4–9.

[64] Liu, L., Mandelis, A., Melnikov, A., Michaelian, K., Huan, H., and Haisch, C. (2016a). Step-Scan T-Cell Fourier Transform Infrared Photoacoustic Spectroscopy (FTIR-PAS) for Monitoring Environmental Air Pollutants. *International Journal of Thermophysics*, 37(7):1–9.

[65] Liu, Q., Cao, Z., Shao, S., Zhu, W., Huang, H., Gao, X., and Li, X. (2016b). Simultaneously Photoacoustic Measurement of Carbon Dioxide and Nitrous Oxide Using a Quantum Cascade Laser. *Journal of Applied Spectroscopy*, 83(4):682–686.

[66] Lung, C., Jones, R., Zellweger, C., Karppinen, A., Penza, M., Dye, T., Hüglin, C., Ning, Z., Leigh, R., Hagan, D., Laurent, O., Carmichael, G., Beig, G., Cohen, R., Cross, E., Gentner, D., Gerboles, M., Khan, S., Mudu, P., Carceller, X. Q., Ruggeri, G., Smith, K., and Tarasova, O. (2018). *Low-cost sensors for the measurement of atmospheric composition: overview of topic and future applications (WMO).* Number May.

[67] McLean, E. A., Sica, L., and Glass, A. J. (1968). INTERFEROMETRIC OBSERVATION OF ABSORPTION INDUCED INDEX CHANGE ASSOCIATED WITH THERMAL BLOOMING. *Applied Physics Letters*, 13(11):369–371.

[68] McNaghten, E. D., Grant, K. A., Parkes, A. M., and Martin, P. A. (2012). Simultaneous detection of trace gases using multiplexed tunable diode lasers and a photoacoustic cell containing a cantilever microphone. *Applied Physics B*, 107(3):861–871.

[69] Mead, M. I., Popoola, O. A. M., Stewart, G. B., Landshoff, P., Calleja, M., Hayes, M., Baldovi, J. J., McLeod, M. W., Hodgson, T. F., Dicks, J., Lewis, A., Cohen, J., Baron, R., Saffell, J. R., and Jones, R. L. (2013). The use of electrochemical sensors for monitoring urban air quality in low-cost, high-density networks. *Atmospheric Environment*, 70:186–203.

[70] Mijling, B., Jiang, Q., De Jonge, D., and Bocconi, S. (2018). Field calibration of electrochemical NO2 sensors in a citizen science context. *Atmospheric Measurement Techniques*, 11(3):1297–1312.

[71] Miklós, A., Hess, P., and Bozóki, Z. (2001). Application of acoustic resonators in photoacoustic trace gas analysis and metrology. *Review of Scientific Instruments*, 72(4):1937–1955.

[72] Mirsense (2019). Compact oem trace gas analyzer based on quantum cascade lasers and photoacoustics.

[73] Moosmüller, H. and Arnott, W. P. (1996). Folded Jamin interferometer: a stable instrument for refractive-index measurements. *Optics Letters*, 21(6):438.

[74] Moosmüller, H., Chakrabarty, R. K., and Arnott, W. P. (2009). Aerosol light absorption and its measurement: A review. *Journal of Quantitative Spectroscopy and Radiative Transfer*, 110(11):844–878.

[75] Mordmueller, M., Schade, W., and Willer, U. (2017). QEPAS with electrical co-excitation for photoacoustic measurements in fluctuating background gases. *Applied Physics B: Lasers and Optics*, 123(8):1–9.

[76] Mordmüller, M., Köhring, M., Schade, W., and Willer, U. (2015). An electrically and optically cooperated QEPAS device for highly integrated gas sensors. *Applied Physics B: Lasers and Optics*, 119(1):111–118.

[77] Mueller, M. D., Hasenfratz, D., Saukh, O., Fierz, M., and Hueglin, C. (2016). Statistical modelling of particle number concentration in Zurich at high spatio-temporal resolution utilizing data from a mobile sensor network. *Atmospheric Environment*, 126:171–181.

[78] Oberdörster, G., Oberdörster, E., and Oberdörster, J. (2005). Nanotoxicology: An emerging discipline evolving from studies of ultrafine particles. *Environmental Health Perspectives*, 113(7):823–839.

[79] Parliament, E. and Union, C. o. t. E. (2015). Comission Directive (EU) 2015/1480.

[80] Patimisco, P., Sampaolo, A., Dong, L., Tittel, F. K., and Spagnolo, V. (2018). Recent advances in quartz enhanced photoacoustic sensing. *Applied Physics Reviews*, 5(1).

[81] Patimisco, P., Sampaolo, A., Zheng, H., Dong, L., Tittel, F. K., and Spagnolo, V. (2017). Quartz-enhanced photoacoustic spectrophones exploiting custom tuning forks: a review. *Advances in Physics: X*, 2(1):169–187.

[82] Patimisco, P., Scamarcio, G., Tittel, F., and Spagnolo, V. (2014). Quartz-Enhanced Photoacoustic Spectroscopy: A Review. *Sensors*, 14(4):6165–6206.

[83] Patrick Arnott, W., Moosmüller, H., Fred Rogers, C., Jin, T., and Bruch, R. (1999). Photoacoustic spectrometer for measuring light absorption by aerosol: instrument description. *Atmospheric Environment*, 33(17):2845–2852.

[84] Petra, N. (2019). Software for Modeling QEPAS and ROTADE Trace Gas Sensors. [online] https://personal.utdallas.edu/~zweck/Resources/QEPAS/index.html.

[85] Petra, N., Zweck, J., Kosterev, A. A., Minkoff, S. E., and Thomazy, D. (2009). Theoretical analysis of a quartz-enhanced photoacoustic spectroscopy sensor. *Applied Physics B*, 94(4):673–680.

[86] Petzold, A. and Niessner, R. (1996). Photoacoustic soot sensor for in-situ black carbon monitoring. *Applied Physics B Laser and Optics*, 63(2):191–197.

[87] Risser, C., Parvitte, B., Vallon, R., and Zeninari, V. (2014). Optimization and complete characterization of a photoacoustic gas detector. *Applied Physics B: Lasers and Optics*, 118(2):319–326.

[88] Roehl, C. M., Orlando, J. J., Tyndall, G. S., Shetter, R. E., Vazquez, G. J., Cantrell, C. A., and Calvert, J. G. (1994). Temperature Dependence of the Quantum Yields for the Photolysis of NO2 Near the Dissociation Limit. *The Journal of Physical Chemistry*, 98(32):7837–7843.

[89] Rothman, L. S., Gordon, I. E., Babikov, Y., Barbe, A., Chris Benner, D., Bernath, P. F., Birk, M., Bizzocchi, L., Boudon, V., Brown, L. R., Campargue, A., Chance, K., Cohen, E. A., Coudert, L. H., Devi, V. M., Drouin, B. J., Fayt, A., Flaud, J. M., Gamache, R. R., Harrison, J. J., Hartmann, J. M., Hill, C., Hodges, J. T., Jacquemart, D., Jolly, A., Lamouroux, J., Le Roy, R. J., Li, G., Long, D. A., Lyulin, O. M., Mackie, C. J., Massie, S. T., Mikhailenko, S., Müller, H. S., Naumenko, O. V., Nikitin, A. V., Orphal, J., Perevalov, V., Perrin, A., Polovtseva, E. R., Richard, C., Smith, M. A., Starikova, E., Sung, K., Tashkun, S., Tennyson, J., Toon, G. C., Tyuterev, V. G., and Wagner, G. (2013). The HITRAN2012 molecular spectroscopic database. *Journal of Quantitative Spectroscopy and Radiative Transfer*, 130:4–50.

[90] Rück, T., Bierl, R., and Matysik, F. M. (2017). Low-cost photoacoustic NO2 trace gas monitoring at the pptV-level. *Sensors and Actuators, A: Physical*, 263(2):501–509.

[91] Rück, T., Bierl, R., and Matysik, F. M. (2018). NO2 trace gas monitoring in air using off-beam quartz enhanced photoacoustic spectroscopy (QEPAS) and interference studies towards CO2, H2O and acoustic noise. *Sensors and Actuators, B: Chemical*, 255(2):2462–2471.

[92] Russell, D. A. (2000). On the sound field radiated by a tuning fork. *American Journal of Physics*, 68(12):1139–1145.

[93] Sampaolo, A., Patimisco, P., Dong, L., Geras, A., Scamarcio, G., Starecki, T., Tittel, F. K., and Spagnolo, V. (2015). Quartz-enhanced photoacoustic spectroscopy exploiting tuning fork overtone modes. *Applied Physics Letters*, 107(23).

[94] Schindler, W., Haisch, C., Beck, H. A., Niessner, R., Jacob, E., and Rothe, D. (2004). A Photoacoustic Sensor System for Time Resolved Quantification of Diesel Soot Emissions. In *SAE 2004 World Congress & Exhibition*, number 724. SAE International.

[95] Schnaiter, M., Horvath, H., Möhler, O., Naumann, K. H., Saathoff, H., and Schöck, O. W. (2003). UV-VIS-NIR spectral optical properties of soot and soot-containing aerosols. *Journal of Aerosol Science*, 34(10):1421–1444.

[96] Scholz, L., Ortiz Perez, A., Bierer, B., Eaksen, P., Wöllenstein, J., and Palzer, S. (2016). Carbon Dioxide Sensor for Mobile Devices. *IEEE Sensors*, 07(9):6–8.

[97] Schriefl, M. A., Bergmann, A., and Fierz, M. (2019). Design principles for sensing particle number concentration and mean particle size with unipolar diffusion charging. *IEEE Sensors Journal*, 19(4):1392–1399.

[98] Sedlacek, A. and Lee, J. (2007). Photothermal interferometric aerosol absorption spectrometry. *Aerosol Science and Technology*, 41(12):1089–1101.

[99] Sedlacek, A. J. (2006). Real-time detection of ambient aerosols using photothermal interferometry: Folded Jamin interferometer. *Review of Scientific Instruments*, 77(6).

[100] Sensirion AG (2019). Breakthrough in CO2 Sensing: First Sensirion Miniaturized CO2 Sensor. [online] https://www.sensirion.com/en/about-us/newsroom/news-and-press-releases/detail/news/breakthrough-in-co2-sensing-first-sensirion-miniaturized-co2-sensor/.

[101] Skrabal, P. M. (2009). *Spektroskopie*. vdf Hochschulverlag AG, 2nd edition.

[102] Slezak, V. (2001). High-precision pulsed photoacoustic spectroscopy in NO2-N2. *Applied Physics B: Lasers and Optics*, 73(7):751–755.

[103] Song, K., Cha, H., Kapitanov, V., Ponomarev, Y., Rostov, A., Courtois, D., Parvitte, B., and Zeninari, V. (2002). Differential Helmholtz resonant photoacoustic cell for spectroscopy and gas analysis with room-temperature diode lasers. *Applied Physics B: Lasers and Optics*, 75(2-3):215–227.

[104] Starecki, T. (2014). Analog Front-End Circuitry in Piezoelectric and Microphone Detection of Photoacoustic Signals. *International Journal of Thermophysics*, 35(11):2124–2139.

[105] Starecki, T. and Wieczorek, P. Z. (2017). A high sensitivity preamplifier for quartz tuning forks in qepas (Quartz enhanced photoacoustic spectroscopy) applications. *Sensors (Switzerland)*, 17(11).

[106] Szakáll, M., Varga, A., Pogány, A., Bozóki, Z., and Szabó, G. (2009). Novel resonance profiling and tracking method for photoacoustic measurements. *Applied Physics B: Lasers and Optics*, 94(4):691–698.

[107] Terry Tetley (2019). Particulate air pollution and health. Presented at the Cambridge Particle Meeting, Cambridge (UK).

[108] Ullah, N., Park, S.-j., Lee, Y. J., and Park, S. (2015). Investigation of the Electrical Model Parameters of Quartz Tuning Forks from a Low-frequency Impedance Analysis Using a Lock-in Amplifier. *New Physics: Sae Mulli*, 65(1):76–80.

[109] Uotila, J. (2009). *Use Of The Optical Cantilever Microphone In Photoacoustic Spectroscopy*.

[110] van den Elshout, S. (2012). CAQI Air quliaty index: Comparing Urban Air Quality across Borders. Technical report, Schiedam.

[111] Vandaele, A., Hermans, C., Simon, P., Carleer, M., Colin, R., Fally, S., Mérienne, M., Jenouvrier, A., and Coquart, B. (1998). Measurements of the NO2 absorption cross-section from 42,000 cm-1 to 10,000 cm-1 (238-1000 nm) at 220 K and 294 K. *Journal of Quantitative Spectroscopy and Radiative Transfer*, 59(3-5):171–184.

[112] Werle, P., Mücke, R., and Slemr, F. (1993). The limits of signal averaging in atmospheric trace-gas monitoring by tunable diode-laser absorption spectroscopy (TDLAS). *Applied Physics B Photophysics and Laser Chemistry*, 57(2):131–139.

[113] WHO (2017). *Evolution of WHO air quality guidelines: past, present and future*.

[114] Wiegleb, G. (2016). *Gasmesstechnik in Theorie und Praxis*. Springer Fachmedien Wiesbaden, Wiesbaden.

[115] Williams, R., Kilaru, V. J., Snyder, E. G., Kaufman, A., Dye, T., Rutter, A., Russell, A., and Hafner, H. (2014). Air Sensor Guidebook.

[116] Winkowski, M. and Stacewicz, T. (2019). Low noise, open-source QEPAS system with instrumentation amplifier. *Scientific Reports*, 9(1):1838.

[117] Wojtas, J., Gluszek, A., Hudzikowski, A., and Tittel, F. (2017). Mid-Infrared Trace Gas Sensor Technology Based on Intracavity Quartz-Enhanced Photoacoustic Spectroscopy. *Sensors*, 17(3):513.

[118] World Health Organisation (2006). *Air quality guidelines for particulate matter, ozone, nitrogen dioxide and sulfur dioxide – Global update 2005*. WHO Press, Geneva.

[119] Wu, H., Dong, L., Zheng, H., Liu, X., Yin, X., Ma, W., Zhang, L., Yin, W., Jia, S., and Tittel, F. K. (2015). Enhanced near-infrared QEPAS sensor for sub-ppm level H2S detection by means of a fiber amplified 1582 nm DFB laser. *Sensors and Actuators B: Chemical*, 221:666–672.

[120] Wu, H., Dong, L., Zheng, H., Yu, Y., Ma, W., Zhang, L., Yin, W., Xiao, L., Jia, S., and Tittel, F. K. (2017a). Beat frequency quartz-enhanced photoacoustic spectroscopy for fast and calibration-free continuous trace-gas monitoring. *Nature Communications*, 8:15331.

[121] Wu, H., Yin, X., Dong, L., Pei, K., Sampaolo, A., Patimisco, P., Zheng, H., Ma, W., Zhang, L., Yin, W., Xiao, L., Spagnolo, V., Jia, S., and Tittel, F. K. (2017b). Simultaneous dual-gas QEPAS detection based on a fundamental and overtone combined vibration of quartz tuning fork. *Applied Physics Letters*, 110(12).

[122] Yi, H., Liu, K., Chen, W., Tan, T., Wang, L., and Gao, X. (2011). Application of a broadband blue laser diode to trace NO2 detection using off-beam quartz-enhanced photoacoustic spectroscopy. *Optics Letters*, 36(4):481.

[123] Yi, H., Liu, K., Sun, S., Zhang, W., and Gao, X. (2012). Theoretical analysis of off beam quartz-enhanced photoacoustic spectroscopy sensor. *Optics Communications*, 285(24):5306–5312.

[124] Yin, X., Dong, L., Wu, H., Zheng, H., Ma, W., Zhang, L., Yin, W., Jia, S., and Tittel, F. K. (2017). Sub-ppb nitrogen dioxide detection with a large linear dynamic range by use of a differential photoacoustic cell and a 3.5 W blue multimode diode laser. *Sensors and Actuators, B: Chemical*, 247:329–335.

[125] Zajarevich, N., Peuriot, A., and Slezak, V. (2016). Characterization of a photoacoustic system through neural networks to determine multicomponent samples. *Infrared Physics & Technology*, 77:485–489.

[126] Zheng, H., Dong, L., Patimisco, P., Wu, H., Sampaolo, A., Yin, X., Li, S., Ma, W., Zhang, L., Yin, W., Xiao, L., Spagnolo, V., Jia, S., and Tittel, F. K. (2017). Double antinode excited quartz-enhanced photoacoustic spectrophone. *Applied Physics Letters*, 110(2).

[127] Zheng, H., Dong, L., Sampaolo, A., Patimisco, P., Ma, W., Zhang, L., Yin, W., Xiao, L., Spagnolo, V., Jia, S., and Tittel, F. K. (2016a). Overtone resonance enhanced single-tube on-beam quartz enhanced photoacoustic spectrophone. *Applied Physics Letters*, 109(11).

[128] Zheng, H., Dong, L., Sampaolo, A., Wu, H., Patimisco, P., Yin, X., Ma, W., Zhang, L., Yin, W., Spagnolo, V., Jia, S., and Tittel, F. K. (2016b). Single-tube on-beam quartz-enhanced photoacoustic spectroscopy. *Optics Letters*, 41(5):978.

[129] Zheng, H., Dong, L., Yin, X., Liu, X., Wu, H., Zhang, L., Ma, W., Yin, W., and Jia, S. (2015). Ppb-level QEPAS NO2 sensor by use of electrical modulation cancellation method with a high power blue LED. *Sensors and Actuators, B: Chemical*, 208(2):173–179.

[130] Zhu, Y., Hinds, W. C., Kim, S., Shen, S., and Sioutas, C. (2002). Study of ultrafine particles near a major highway with heavy-duty diesel traffic. *Atmospheric Environment*, 36(27):4323–4335.

Appendix A

A.1 Limitation in photoacoustics due to laser power

Gas sensor

For a QEPAS gas sensor, the photon flux and thus the laser intensity should not be as high as to deplete the ground state, as otherwise photoacoustic signal generation would be less efficient. For a two-level system of ground state density N and excited state density N', a rate equation can be stated [11]

$$\frac{dN'}{dt} = (N - N')\sigma\phi - N'\sigma\phi - \frac{N'}{\tau}, \tag{A.1}$$

where ϕ is the photon flux by the laser, σ ($\sigma \approx 5 \times 10^{-19}\,\mathrm{cm}^2$ for NO_2 [111]) the absorption cross-section at the excitation wavelength and τ the relaxation time ($\tau = 2\,\mu\mathrm{s}$ for NO_2 [46]). As a worst-case scenario, Equation (A.1) can be set to zero (steady state) and a ratio of excited state density to ground state density can be stated as

$$\frac{N'}{N} = \frac{\phi}{2 + 1/(\sigma\tau)} \approx \phi\sigma\tau. \tag{A.2}$$

For constant illumination by a laser with wavelength λ, power P_L and beam diameter of a gaussian beam of $\sigma_b = 100\,\mu\mathrm{m}$ the photon flux through the area of a circle with diameter σ_b around the focus is

$$\phi = \frac{0.058 \cdot P_L \cdot \lambda \cdot 4}{h \cdot c \cdot \sigma_b^2 \cdot \pi}, \tag{A.3}$$

where c is the speed of light and h is Planck's constant. For $P_L = 80\,\mathrm{mW}$ as it was used in **Paper 4** one calculates $\frac{N'}{N} \approx \frac{1}{10000}$ and thus the ground state is not depleted with the laser used. Even for higher laser powers the ground state would be sufficiently populated.

Black carbon sensor

In incandescence-based techniques, a particle is heated to such high temperatures (several 100 K), that their thermal radiation can be detected to deduce size information [74].
For a photoacoustic black carbon sensor, this would be an unwanted relaxation pathway. The eventual temperature increase of a spherical particle can be calculated as [74]

$$T_\infty = \frac{I_{exc} \cdot Q_{abs} \cdot r}{4 \cdot \kappa_{air}}, \tag{A.4}$$

where Q_{abs} is the aerosol light absorption efficiency and $\kappa_{air} = 0.0257\,\mathrm{W\,m^{-1}\,K}$ is the thermal conductivity of air. Q_{abs} can be calculated with MATLAB[1] with the arguments complex refractive index $m = 1.75 + 0.75i$[74], excitation wavelength ($\lambda = 850\,\mathrm{nm}$) and the radius of the particle r. For the intensity, we use the same assumption as above, i.e. $I_{exc} = \frac{0.058 \cdot P_L \cdot 4}{\sigma_b^2 \cdot \pi}$. For estimating the temperature we use a fairly large size of $r = 100\,\mathrm{nm}$. For the used laser power of $P_L = 30\,\mathrm{mW}$ the temperature increase is $\approx 190\,\mathrm{mK}$. Even for the proposed laser power of $P_L = 500\,\mathrm{mW}$ for a lower detection limit, the temperature increase is less than 3.2 K.

A.2 Delayed molecular relaxation in photoacoustics

Kalkman and van Kesteren [46] describe a decrease in photoacoustic signal as a function of O_2 concentration due to delayed molecular relaxation. We verified these findings by applying different mixtures of NO_2 and O_2 to the QEPAS cell. In particular, 20 ppm NO_2 in synthetic air were mixed with N_2 at different dilution ratios. As the O_2 concentration of the 20 ppm NO_2 gas cylinder is 20.5 %, this point was used as a reference and set to the corresponding value, according to Eq. (3.2). By normalizing the QEPAS signal to the NO_2 concentration and calculating the corresponding O_2 concentrations, the findings by Kalkman and van Kesteren [46] could be confirmed. The results are depicted in red in Fig. A.1 and compared to the theoretical curve from Eq. (3.2) (black).

---

[1] Piotr J. Flatau University of California, San Diego. http://scatterlib.wikidot.com/mie based on "Absorption and Scattering of Light by Small Particles" by Bohren, Craig F., Huffman, Donald R, 1983, Wiley, New York, 530 pages.

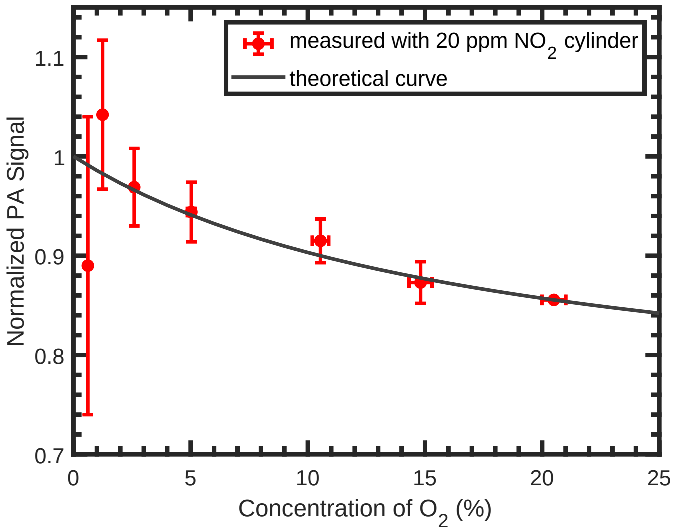

Fig. A.1 Normalized photoacoustic signal as a function of different O_2 concentrations (red) compared to the theoretical curve described by Kalkman and van Kesteren [46]. Errorbars of the normalized PA signals and the concentrations show the standard deviation calculated with GUM Workbench.

A.3 Gas diluter

A detailed description of the gas diluter can be found in **Paper 2**. A photograph of the diluter is shown in Figure A.2.

A.4 CHIRP methodology for QEPAS

Usually a frequency sweep is used to determine the resonance frequency f_0 of the QTF. A frequency sweep might take 100 seconds for a $0.5 Hz$ sweep over a range of $50 Hz$ and an integration time of $1 s$. During this time, no measurements can be performed and it also relies on the presence of the target gas. Our approach is based on the method described by Szakáll et al. [106] for conventional PAS in the presence of a target gas.By modulating the laser with a CHIRP signal over a frequency range, f_0 can be determined in less than 1 s, which is less than the usual integration time of lock-in amplifiers. After applying a simple FFT and a subsequent fit to the response, f_0 and Q can be deduced (cf. Figure A.3(a)).

Table A.1 shows a comparison of different CHIRP durations. It can be seen that a short CHIRP of 0.5 s duration is sufficient to determine the resonance frequency with a standard deviation of 0.3 Hz. It can also be seen, that the CHIRP is not sufficient for the determination

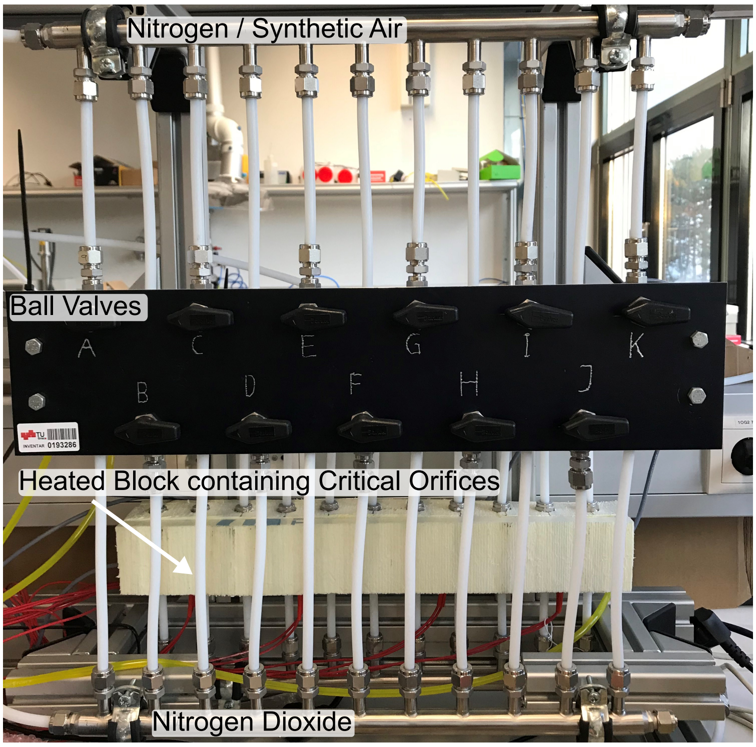

Fig. A.2 Photo of the gas diluter. The length is ≈ 60 cm.

of the quality factor. A signal proportional to the NO_2 concentration could also be measured with the CHIRP (cf. Figure A.3(b)), but only with high uncertainty and concentrations above approximately 2 ppm. Since not much change to be expected, a frequent CHIRP for resonance frequency determination in combination with a LIA is most suitable.

Table A.1 Comparison of CHIRP times. Ten measurements taken for each CHIRP duration. The last row shows the reference values, deduced from a frequency sweep. t_{dur}... duration of the CHIRP/sweep. f_0 ... mean resonance frequency. σ_{f_0} ... standard deviation of resonance frequency. Q ... mean quality factor. σ_Q ... standard deviation of quality factor.

t_{dur}(s)	f_0(Hz)	σ_{f_0}(Hz)	Q	σ_Q
0.5	32.7466	0.3	8729	1215
1	32.7463	0.3	9737	2156
2	32.7466	0.2	9233	1097
4	32.7466	0.2	9201	927
100	32.7466		8138	

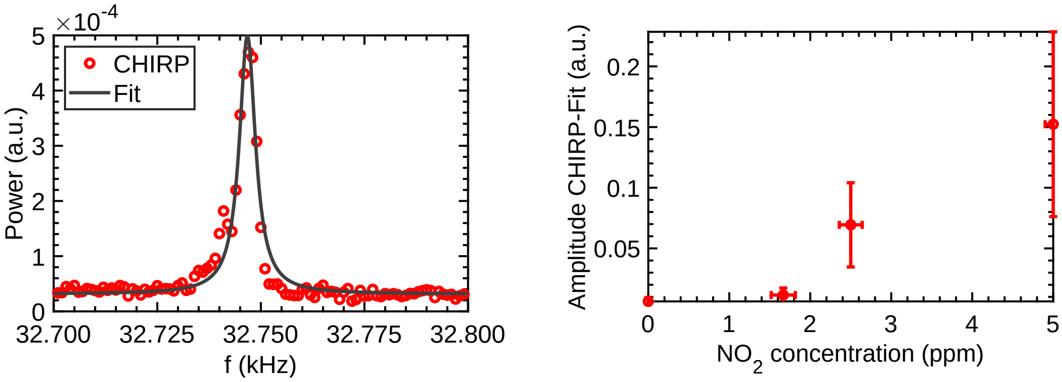

(a) (b)

Fig. A.3 **(a)** Result of a CHIRP of 500 ms duration (red dots) and fit (solid black curve). **(b)** Square-root of fit to CHIRP signal amplitude (in theory proportional to photoacoustic pressure).

A.5 Selected steps in modelling QEPAS

Some steps in the theoretical model by Petra et al. [85] are not straight-forward for a non-mathematician, such as the author of this thesis. These steps are therefore given in this appendix.

A homogeneous solution of the Bessel equation of order zero (Equation (2.11)) is given by a linear combination of the Hankel functions of the first and second kind of order zero [53]

$$p_h(r) = B_1 H_0^{(1)}(kr) + B_2 H_0^{(2)}(kr) \tag{A.5}$$

with

$$H_n^{(1)}(x) = J_n(x) + iY_n(x) \tag{A.6}$$

$$H_n^{(2)}(x) = J_n(x) - iY_n(x), \tag{A.7}$$

where $J_n(x)$ and $Y_n(x)$ are the Bessel functions of the first and second kind. Therefore, a particular solution of the form of

$$p_h(r) = c_1(r)H_0^{(1)}(kr) + c_2(r)H_0^{(2)}(kr) \tag{A.8}$$

has to be found. By the method of variation of constants, the following system of linear equations can be solved for the first derivatives of $c_1(r)$ and $c_2(r)$

$$\begin{pmatrix} H_0^{(1)}(kr) & H_0^{(2)}(kr) \\ H_0^{(1)}(kr)' & H_0^{(2)}(kr)' \end{pmatrix} \begin{pmatrix} c_1(r)' \\ c_2(r)' \end{pmatrix} = \begin{pmatrix} 0 \\ Q(r) \end{pmatrix} \tag{A.9}$$

Using the relation [1]

$$J_\alpha(x)\frac{dY_\alpha}{dx} - \frac{dJ_\alpha}{dx}Y_\alpha(x) = \frac{2}{\pi x} \tag{A.10}$$

for the Wronskian and plugging in the definitions from Equations (A.6) and (A.7), $c_1(r)$ and $c_2(r)$ can be determined as given by Petra et al. [85]

$$c_1(r) = -\frac{i\pi}{4}\int_0^r sH_0^{(2)}(ks)Q(s)ds \tag{A.11}$$

$$c_2(r) = \frac{i\pi}{4}\int_0^r sH_0^{(1)}(ks)Q(s)ds. \tag{A.12}$$

The transition to rewrite the solution in terms of $f_1(r)$ and $f_2(r)$ as

$$P(r,t) = \Big((B_1 + c_1(r))H_0^{(1)}(kr) + (B_2 + c_2(r))H_0^{(2)}(kr)\Big)e^{i\omega t} = \tag{A.13}$$

$$= \frac{\pi M}{2c^2}\left(f_1(r) - if_2(r)\right)e^{i\omega t} \tag{A.14}$$

as well as the real part of the acoustic pressure

$$P(r,t) = A(r)\sin\left(\omega t - \theta(r)\right) \tag{A.15}$$

can be found in the *Numerical Computations (review)* [84].

In the available MATLAB code [84], the MATLAB function *quad* was replaced by *integral*, which enabled replacing an iterative routine for

$$\lim_{r\to\infty}\int_0^r sY_0(ks)e^{\frac{-s^2}{2\sigma^2}}ds$$

and

$$\lim_{r\to\infty}\int_0^r sJ_0(ks)e^{\frac{-s^2}{2\sigma^2}}ds$$

by

$$\int_0^\infty sY_0(ks)e^{\frac{-s^2}{2\sigma^2}}ds$$

and

$$\int_0^\infty sJ_0(ks)e^{\frac{-s^2}{2\sigma^2}}ds,$$

respectively.

A.6 Selected steps in modelling PTI

The transmission T of a Fabry–Pérot interferometer (FPI) with maximum transmission T_{max} is given by [18]

$$T = T_{max} \cdot f(\phi), \tag{A.16}$$

where

$$f(\phi) = (1 + \delta \sin^2(\phi))^{-1}, \tag{A.17}$$

with ϕ the phase delay and $\delta = (F/\pi)^2$. F is the finesse, which is calculated from the reflectivity R of the mirrors as $F = \frac{\pi\sqrt{R}}{1-R}$. The second derivative of Equation (A.17) is

$$f''(\phi) = -\frac{\delta(2(2+\delta)\cos(2\phi)+\delta(-3+\cos(4\phi)))}{2\left(1+\delta\sin^2(\phi)\right)^3}. \tag{A.18}$$

Setting Equation (A.18) to zero gives an equation for the inflection point ($\phi = \phi_0$), which is the optimal operation point of the FPI:

$$\cos(2\phi_0) = \frac{1}{2}\sqrt{9+4/\delta+4/\delta^2} - 1/\delta - 1/2. \tag{A.19}$$

Appendix B

Co-supervised master theses

The following master thesis were supervised by Alexander Bergmann and co-supervised by the author of this thesis.

Master thesis 1. Markus Knoll, "Development of a Low-cost, Wireless, Photoacoustic based NO2 Recognition Sensor for Air Pollution Measurements."

Master thesis 2. Alexander Kerschhofer, "Laser Driver and Lock-In Amplifier Circuit Development for a Nitrogen Dioxide Sensor based on Quartz-Enhanced Photoacoustic Spectroscopy."

Master thesis 3. Martin Lampel, "Development of a Compact and Embedded QEPAS Gas Sensor."

Appendix C

Author's contributions to publications

Publications originated during this thesis

Title	"Air quality and health effects — How can wireless sensor networks contribute? A critical review"
Reference	*International Conference on Broadband Communications for Next Generation Networks and Multimedia Applications, Graz*, 2016
Co-authors	A. Bergmann
Personal contribution	Literature review, writing
Publication status	Published
Related chapter	Chapter 1.2
Title	"Low-Power Wide-Area technologies as building block for smart sensors in air quality measurements"
Reference	*Elektrotech. Inftech.*, 135:416–422, 2018
Co-authors	M. Knoll (1st author), A. Bergmann
Personal contribution	supervision, writing
Publication status	Published
Related chapter	Chapter 1.2
Title	"A new Method to Determine the Resonance Frequency in QEPAS"
Reference	2018 Conference on Lasers and Electro-Optics (CLEO), San Jose, CA
Co-authors	B. Lang, A. Bergmann

Personal contribution	Experimental investigation, data evaluation, writing
Publication status	Published
Related chapter	Chapter 3
Title	"A Precise Gas Diluter Based on Binary Weighted Critical Flows to Create NO2 Concentrations"
Reference	*Proceedings*, 2(13):998, 2018
Co-authors	A. Bergmann
Personal contribution	Design, tests, experiments, data evaluation, writing
Publication status	Published
Related chapter	Chapter 3
Title	"Laser Driver and Analysis Circuitry Development for Quartz-Enhanced Photoacoustic Spectroscopy of NO2 for IoT Purpose"
Reference	*Proceedings*, 2(13):1062, 2018
Co-authors	A. Kerschhofer (1^{st} author), A. Bergmann
Personal contribution	supervision, writing
Publication status	Published
Related chapter	Chapter 3 and 4
Title	"Soot Mass Concentration Sensor using Quartz-Enhanced Photoacoustic Spectroscopy"
Reference	*Aerosol Science and Technology*, 53(9):971–975, 2019
Co-authors	M. Schriefl, R. T. Nishida, S. Hochgreb, A. Bergmann
Personal contribution	QEPAS sensor development, experimental investigation, writing
Publication status	Published
Related chapter	Chapter 4
Title	"Intensity Modulated Photothermal Measurements of NO2 with a Compact Fiber-Coupled Fabry–Pérot Interferometer"
Reference	*Sensors*, 19(15):3341, 2019
Co-authors	B. Lang, A. Bergmann
Personal contribution	Experimental investigation, data evaluation, writing
Publication status	Published
Related chapter	Chapter 3

Title	"Optical Aerosol Sensing – from Air Quality to Global Warming"
Reference	Applied Industrial Optics: Spectroscopy, Imaging and Metrology, 2019
Co-authors	P. Maierhofer (1st author), A. Buchberger, A. Bergmann
Personal contribution	Writing of QEPAS part
Publication status	Published
Related chapter	-
Title	"Towards Low-Cost QEPAS Sensors for Nitrogen Dioxide Detection"
Reference	*Photoacoustics*
Co-authors	B. Schweighofer, H. Wegleiter, M. Knoll, B. Lang, A. Bergmann
Personal contribution	Experimental investigation, data evaluation, writing
Publication status	Accepted
Related chapter	Chapter 3
Title	"Study of molecular relaxation effects on vibrational water vapor photoacoustic spectroscopy in air"
Reference	*Applied Physics B*
Co-authors	B. Lang (1st author), G. Brunnhofer, J. P. Valero, S. Schweighart, A. Klug, W. Hassler, A. Bergmann
Personal contribution	Revision of the manuscript, assistance with experiments
Publication status	Accepted
Related chapter	-

Contribution to scientific conferences

Title	"Air quality and health effects — How can wireless sensor networks contribute? A critical review"
Conference	International Conference on Broadband Communications for Next Generation Networks and Multimedia Applications (CoBCom), Graz (AUT), 2016
Contribution	Oral presentation
Co-authors	A. Bergmann
Title	"Quartz-enhanced photoacoustic spectroscopy for environmental trace gas sensing with WSNWs"
Conference	19th International Conference on Photoacoustic and Photothermal Phenomena, Bilbao (ES), 2017
Contribution	Poster presentation
Co-authors	A. Bergmann
Title	"A new Method to Determine the Resonance Frequency in QEPAS"
Conference	Conference on Lasers and Electrooptics, St. Jose (USA), 2018
Contribution	Oral presentation
Co-authors	B. Lang, A. Bergmann
Title	"Development of a Low-Cost Quartz-Enhanced Photoacoustic Spectroscopy Nitrogen Dioxide Sensor Network for Air Pollution Measurements"
Conference	Transport and Air Pollution Conference, Thessaloniki (GRE), 2019
Contribution	Oral presentation
Co-authors	M.Knoll, A. Bergmann
Title	"Soot Mass Concentration Sensor using Quartz Enhanced Photoacoustic Spectroscopy"
Conference	Cambridge Particle Meeting, Cambridge (UK), 2019
Contribution	Poster presentation
Co-authors	M. Schriefl, R. T. Nishida, S. Hochgreb, A. Bergmann

Appendix D

Articles in this thesis

D.1 Paper 1

Air Quality and Health Effects - How can Wireless Sensor Networks contribute? A critical Review

Philipp Breitegger
Institute of Electronic Sensor Systems
Graz, University of Technology
Graz, Austria
http://ies.tugraz.at/

Alexander Bergmann
Institute of Electronic Sensor Systems
Graz, University of Technology
Graz, Austria
http://ies.tugraz.at/

***Abstract*—Also in western countries, air pollution is a big health risk, additionally resulting in huge economic damage. At present, air pollution is mainly monitored with highly accurate equipment but at extremely low spatial resolution. Overcoming the disadvantage of the low spatial resolution, and building a wireless network of sensors, can open doors to new applications, both to better understand the sources and the health effects of air pollution.**

We review selected state-of-the-art projects to supply the reader with an overview over current applications that were enabled by the use of new sensors, wireless sensor networks (WSNWs) and information technology. We will critically asses the spatial and temporal resolution, the sensor accuracy and the results.

We will show that the crucial step, that is still to be done, is the development of dependable sensors. This can enable the breakthrough of existing applications. By introducing intelligent nodes, the capabilities of the Internet of Things (IoT) can trigger new use cases. We will conclude with an outlook on our future work, by presenting novel applications to better protect citizens from the adverse health effects of air pollution and to better understand those effects. We will show that these applications require dependable sensors and WSNWs.

I. WHY DO WE MONITOR AIR POLLUTION?

Air-pollution, as a result of increased industrialization, urbanization and individual mobility has become a huge health risk in all countries worldwide. The World Health Organization (WHO) estimates that one in eight premature deaths is due to the effects of the air pollutant particulate matter (PM). [1] Following these numbers, WHO recommends limits for harmful pollutants. For NO_2 there are limits for yearly and hourly means, which are depicted in Table I. In contrast to these values, the European Union (EU) allows the hourly limit to be exceeded 18 times a calendar year. [2]

TABLE I
WHO LIMITS FOR NO_2

Yearly limit $[\mu g/m^3]$	**Hourly limit** $[\mu g/m^3]$
40	200

Also, health impacts result in huge economic damage. The yearly costs of air pollution's health impacts are estimated to be EUR $330 - 940$ bn according to Reference [3]. As the numbers from References [1] and [3] show, there is a big potential of increasing quality of life, as well as decreasing economic damage by increasing air quality (AQ). Monitoring air pollution helps in the following four ways.

Firstly, it can be investigated where and under which circumstances high air pollution occurs, so that laws can be enacted to reduce emission. Secondly, only accurate AQ measurements allow enforcement of these laws. Thirdly, citizens' awareness can be raised. Lastly, the research about the adverse health effects of air pollution strongly depends on accurate data about air pollution, to determine the exposure of individuals, which is yet not available at required accuracy.

In this publication, we will focus our research on monitoring NO_X (i.e. the sum of nitric oxide (NO) and nitrogen dioxide (NO_2)), if not otherwise mentioned.

II. HOW CAN WE MONITOR AIR POLLUTION?

The EU is aware of the damage by air pollution and adopted the limits from WHO (EU limits are less stringent) and further released a common air quality index (CAQI) to make it easy for citizens to inform about the harm of a present pollutant concentration. In agglomerations, EU countries are obligated to operating monitoring stations to monitor certain air pollutants, such as particulate matter with a diameter of less than ten micrometers (PM_{10}), ozone (O_3), and NO_2. Those expensive, but very precise monitoring stations perform point measurements at places representative for roadsides and urban background. Due to the high cost of the measurement equipment, the number of monitoring stations in agglomerations is low. As an example, Graz with 280000 inhabitants and a size of $130\,km^2$ is equipped with eight measurement stations. Therefore, models have to be used, to increase the spatial resolution, i.e., to estimate the pollution concentration at unmonitored sites. For that purpose, a spatial distribution is usually calculated with dispersion or land-use-regression (LUR) models, together with the point measurements, and other explanatory variables, such as meteorological data.

Another attempt to increase the spatial resolution of measure-

2016 International Conference on Broadband Communications for Next Generation Networks and Multimedia Applications (CoBCom)
September 14-16, 2016, Graz, Austria
ISBN: 978-1-5090-2270-0

ments (and as a result also resolution and/or the accuracy of model predictions), is an increased number of measurement stations, which, as a result of the high cost, have to be equipped with cheaper measurement equipment (low-cost sensors). These sensors, as a drawback, are usually less accurate. Other research projects aim at increasing the spatial coverage by mounting those sensors on vehicles or letting individuals measure AQ with mobile sensors. Also, mobile sensors can be used to investigate the exposure of individuals.

Although not the focus of this publication, the authors want to mention a drawback of the previously discussed approaches: their strong dependence on the height where sensors are mounted. A method to overcome this disadvantage, is the measurement of the average pollutant concentration of a vertical air column, averaged over the height using optical measurements. This can be done either on ground, or from space. The latter approach is followed by the SENTINEL-5P mission. It aims at achieving a spatial resolution of $7\,km \times 3.5\,km$ [4], with the advantage of monitoring the pollutant concentration of cities, countries and even continents.

In this publication however, we want to investigate the potential of land placed sensors and sensor networks. For an easier understanding, commonly used sensor principles are shortly explained in the following chapter.

A. A Short Overview over Sensor Technologies Presently Used for Monitoring NO_X

Pollution sensors can be based on chemical and physical principles. Chemiluminescence, passive diffusion (PD) and electrochemical (EC) sensors are based on chemical, where absorption spectroscopy is based on physical principles.

1) Chemiluminescence Detectors: CLD are the only detectors certified to be used in the static monitoring stations by the EU (cf. Reference [2]). The measurement principle is based on the radiative reaction of Ozone with nitrogen oxide (NO). This radiation can be detected to measure the amount of NO. NO_2 can be measured by separating NO_2 to get NO by UV light. By that it is possible to measure NO_X and NO, and by subtraction NO_2. [5] The typical temporal resolution is $1\,s$ (cf. Reference [5]). The CLD used in Reference [5] can detect concentrations as low as 0.5 ppb.[6] Long term stability is guaranteed by regular auto-recalibration.

2) Passive Diffusion Samplers: Passive diffusion samplers have been used over a long time. They work on the principle of diffusion, where high concentration goes to a place of low concentration. They consist of glass tubes, that are open on one end and a metal grid coated with an adsorbant for NO_2 on the other side. Via diffusion, NO_2 goes from the open end to the metal grid. It is an integral measurement method, i.e., it measures all NO_2 from the time it was mounted, to the time it gets collected. Typically, it is operated between two and four weeks. After the tubes get collected, NO_2 is extracted again and the cumulative concentration can be determined via spectrophotometry.[7] In Reference [8] several mechanisms are described that may lead to inaccurate results by passive diffusion samplers. However, in Reference [9] passive diffusion samplers were compared on four places against CLD (two of the places were roadside), and good agreement was found.

3) Electrochemical Sensors: Electrochemical sensors consist of at least two electrodes. Gas diffuses into a chamber, which is usually covered by a membrane, to protect from particles entering the chamber. One of the electrodes is coated with a catalyst for the target gas (e.g. NO_2). The reaction at this electrode is balanced by a reaction at the counter electrode, which results in the flow of a current, that can be detected. Ions are exchanged between the electrodes by an electrolyte. Therefore, the size of the electrolyte reservoir determines the lifetime of an EC sensor. Disadvantages of this sensor type are usually its dependence on humidity, temperature and its cross-sensitivity to other gases. Reference [10] reports cross-interferences of NO on NO_2 of 1.2%. NO_2 sensors used in the same project have an approximately $100\,\%$ interference for O_3. According to Reference [10], EC sensors, which are thought to detected gases in the ppm range, can detect in the ppb range if sufficiently calibrated.

4) Optical Sensors: Optical sensors are based on absorption of light by gases. From the ultra-violet to the mid-infrared region, each molecule has a specific absorption spectrum. As absorption cross-sections for many molecules are known, by measuring absorption at specific wavelengths its concentration can be determined by the use of the absorption law of Beer-Lambert. Due to its ab initio nature, this method enables calibration-free concentration determination. Many variants of optical sensors exist. One variant is Differential Optical Absorption Spectroscopy (DOAS). With this method concentrations in the low ppb range can be detected.[11]

III. CURRENT APPLICATIONS

Pollutant sensors accompanied by recent advances in information technology enable a wide variety of applications. Listed below is a short summary of those applications, tested or being carried out by current research projects. Applications may be interconnected (e.g. measuring personal exposure can be utilized for a concentration map).

- Personal exposure
- Cohort studies
- Accurate point measurements in accordance with Reference [2]
- Traffic control, to enforce different strategies based on pollutant levels and other variables
- RDE-measurements, i.e. real driving emissions from cars, on the road
- Concentration maps for cities and agglomerations
- Real-time AQ maps
- Real-time AQ alerts
- Participative sensing, i.e. users measure air pollution and upload the measurements to the cloud
- Pollution-poor route smartphone app for pedestrians and cyclists
- Research in spatial patterns and dispersion of pollutants

- Research on the influence of external variables, e.g. UV radiation or wind, on air pollution

From the above listed applications, we will briefly cover two, that are usually realized without the use of WSNWs, but can be included in WSNW projects:

Measurement of Real Driving Emissions

An example of the measurement of real driving emissions (RDE) with fixed sensors is the Remote Sensing Detector (RSD) Measurements in Zurich. The project has been running since 1997 at a road in Zurich. The absorption spectroscopy (see section II-A4) equipment is placed at the height of the exhaust pipe of cars. It measures, e.g. the NO-concentration of the cars. By that, it is possible to measure the exhaust of cars under real conditions, in contrast to measurements under laboratory conditions. The so measured emissions can be classified as RDE.

There is an additional camera that records the number plate. If the car is registered in Zurich, database access is granted and it is possible to assign the concentration of the pollutant to the type of car. By that, it was shown, that NO and carbon monoxide (CO) emissions by Diesel vehicles only decreased until the EU norm Euro 4 (2006). Euro 5 (2011) was worse and Euro 6 (2015) only showed little improvements.[12]

Cohort Studies

In cohort studies, groups of people who share a common characteristic (e.g. date of birth), but differ in e.g. the exposure to a pollutant are compared to each other to find out how exposure is linked to certain diseases or cause of death. [13] One example is Reference [14], where the proximity to roads of peoples' homes and the yearly average PM_{10} and NO_2 from the nearest measurement station to the home were examined to increase the relative risk of death and diseases.

To give the reader an overview over applications developed by state-of-the-art projects, in the following sections, we will review representative projects, differing in the application, the network structure and the sensor principles.

Maps of Pollutant Concentrations

AQ Measurements can be used to generate maps of pollutant concentrations. If the availability of data is not time critical, it is possible to use passive samplers without network connection and calculate the distribution map in a post-processing step after the data is collected.

A project was conducted by the same group, that performed modelling in the OpenSense project (cf. section III-A4). It similarly aims at calculating the immission based on a LUR model. The model uses prediction variables such as traffic, elevation and sky view factors.

The network consisted of 48 sites, where three passive diffusion samplers (the concentration value for one site is the mean of three measurements) were mounted in the height of two meters. Each site was measured for a period of two weeks 26 times in a row to get data for a whole year. The resulting application is an NO_2 pollution map for the city of Zurich, showing the average concentration in Zurich for the year 2008 at a resolution of $10\,m \times 10\,m$. It revealed, that in that year, $29\,\%$ of the population have their homes and $48\,\%$ of the workplaces where the annual NO_2 concentration was above the Swiss limit of $30\,\mu g/m^3$. It is claimed that the selection of the measurement sites was not ideal, as they did not represent the whole parameter space of the predictor variables. For the future, *a larger number of sites at elevated and heavily trafficked locations* is suggested. [9]

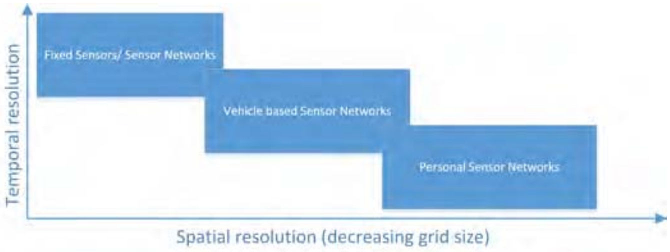

Fig. 1. Classification of WSNWs in terms of their spatial and temporal resolution.

TABLE II
CLASSIFICATION OF THE REVIEWED PROJECTS AND REFERENCES

Classification	Project Name	Reference
Fixed Sensor	Authority	[2]
Fixed SNW	RESCATAME	[15], [16], [17]
Fixed + personal	CamMobSens	[10]
Fixed + personal	CITI-SENSE	[18], [19], [20], [21]
Vehicle mounted	OpenSense	[22]

A. Selected WSNW Projects

Table III gives an overview over the applications that were realized by the reviewed projects. Figure 1 shows the general trend of networks that are used to monitor air quality. Fixed sensor networks usually offer a very good temporal resolution, but suffer from low spatial resolution. Personal SNWs, where sensor nodes are carried by pedestrians, offer a high spatial coverage, but with only few measurement points for one timestamp. Vehicle based sensor networks denote sensors that are mounted on public vehicles, such as buses or trams. Due to the limited routes of public transport, those cannot reach a spatial resolution as high as personal sensor networks, but offer better temporal resolution.

In that sense, the projects we reviewed can be classified as depicted in Table II. We also use this order for our review.

We reviewed representative projects for the aforementioned applications. Table III gives an overview over the applications that were enabled by those projects.

In Figure 2 we have prepared an overview over the state-of-the-art research projects that are reviewed in the following section in the temporal- spatial resolution diagram introduced in Figure 1. Additionally, the accuracy of the utilized sensor technology is indicated with a color code, where green is excellent, yellow is moderate and red is poor.

1) RESCATAME: The project, implemented in the Spanish city Salamanca, is described as a *pervasive air-quality sensors*

TABLE III
APPLICATIONS OF THE REVIEWED PROJECTS

Application	**RESCATAME**	**CamMobSens**	**CITI-SENSE**	**OpenSense**
Personal exposure		×	×	
Cohort studies				
EU Measurements				
Traffic control	×			
RDE-measurements				
Concentration maps			(×)	×
Real-time AQ maps			(×)	
Real-time AQ alerts			(×)	
Participative sensing			×	(×)
Pollution-poor route				×
Research in dispersion		(×)		
Research in external variables				(×)

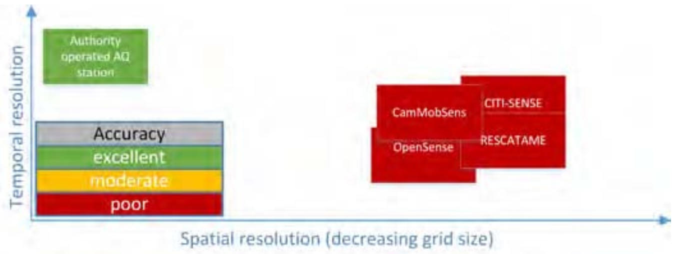

Fig. 2. Reviewed projects in terms of sensor-accuracy, and spatial and temporal resolution.

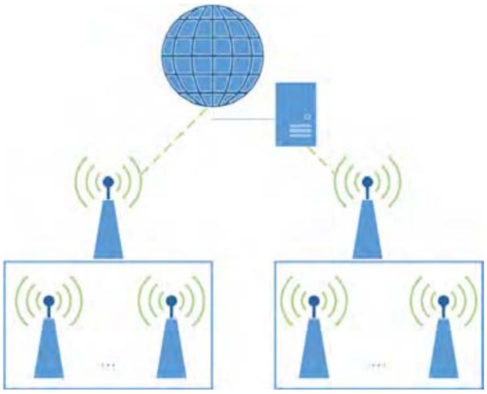

Fig. 3. The network structure in RESCATAME consists of two networks, where the 10 and 25 node send the sensor data to a router, that sends the data to a server.

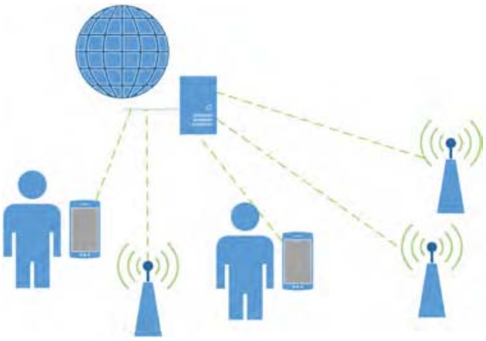

Fig. 4. In CamMobSens mobile and fixed nodes send data to a server via GPRS modules.

network for an environmental friendly urban traffic management in Reference [15]. For the project, sensor nodes in two streets were installed. The first, a ring road, was equipped with 25 nodes at a length of 750 m. The second, a downtown street had 10 nodes installed at 250 m length. The communication structure is depicted in Figure 3. It consists of two networks, where the 10 and 25 node send the sensor data every 10 minutes [15] via ZigBee to a router (called Meshlium), that sends the data via WiFi or GPRS to a server. [16]

Each node contains calibrated sensors for different pollutants, among them are EC NO_2 and a particulate matter sensor. Energy is provided via battery and and a photovoltaic module. The nodes are housed in vandalism proof metal casings where the sensor inlet is positioned at a height of approximately 1.5 m. Within the project, that ran from 2010 to 2012, pollution data was gathered for a year. Unfortunately, the authors of this publication were not able to find out more on the exact outcomes and particularly the success of the project with respect to traffic control, and also the project website was unavailable. Reference [15] shows that a pollution prediction, based on time series analysis [17] for the next hour and three hours was implemented. The application on actions on the traffic however, appears to be rather rudimentary, as the temporary closing of a street by local police officers is suggested as a possible strategy. [15]

2) *CamMobSens:* Within the CamMobSens project, which ran until 2010, mobile as well as static sensor nodes have been deployed in Cambridge, UK. Apart from health benefits, the project investigated EC sensors, intended to measure in the ppm range can be used for ppb measurements by using an advanced calibration algorithm.

The static network (cf. Figure 4) consisted of 46 static nodes (21 of which located in central Cambridge) mounted on lamp-posts in the height of 3 m.[10] Pollutants such as NO and NO_2 were measured with EC sensors. The nodes were powered by batteries, that would allow three months of operation. Measurements were taken every 10 s. Data were sent via GPRS every 2 hours to a web-server and labelled with a GPS and time tag.

The mobile nodes were using EC sensors as well. Data were similarly sent via GPRS (cf. Figure 4) and labelled with a GPS and time tag. Contrary, data acquisition was done every 5 s and upload was done every 30 min.

a) Static: The static nodes were deployed for 2.5 months. Although no applications, such as pollution maps have been created, the nodes reveal the large dependence on the places where they are mounted. This means, that the low number of monitoring stations presently required by the EU is not representative for agglomerations. The measurements also reveal a strong dependence of pollution on the proximity to roads.

b) Mobile: The mobile nodes were used to investigate the exposure of pedestrians, cyclists and vehicle occupants. It is noted, that the latter are exposed to the largest CO and NO concentrations and pedestrians to the highest NO_2 concentration. It was also shown, that the exposure of individuals is not well represented by the authority operated fixed station, by showing that the node of a pedestrian indicated an NO_2 concentration more than four times as high as that of the nearby station. Also, the importance of temporal resolution for individual exposure measurements was highlighted. Mobile nodes, carried in pairs showed the same values when sharing the same time basis. However, with difference in time (even below seconds) the values differed greatly for the same place. As described in section II-A3, EC sensors have a strong dependence on temperature and humidity, and might also suffer from cross-interferences to other gases. The latter was noticed to be $100\,\%$ to O_3 in the case of the NO_2 sensor. With a dedicated O_3 sensor, this could be compensated for, as they tried when locating the node close to an authority operated station that monitored O_3. According Reference [10], gain dependence on temperature and humidity can be neglected for the ppb range. Therefore, they perform a post-processing algorithm depending on these two variables only for the baseline. The algorithm searches for the minimum measurement within a certain time-frame (up to 30 minutes). That is repeated every 24 h.

With this algorithm and the above described sensors, stable operation over eleven months was shown.

The project was continued at Heathrow Airport, as the so called SNAQ (Sensor Network for Air Quality) project, where the same technology of NO and NO_2 sensors was used. Additional sensors, such as for O_3 to be able to reduce the cross interference via post-processing and PM were used.

3) CITI-SENSE: CITI-SENSE is one of five EU FP7 projects on citizens observatories. In nine cities it tested ways of how citizens can participate in environmental governance, e.g. by participative sensing. [18] The project ran from October 2012 to September 2016.

Within CITI-SENSE, air pollution is monitored by citizens indoor in schools and outdoor. [19] For outdoor air pollution measurements, two different products, a mobile as well as static node exist. Users register their device on a website and then upload the sensor readings. Mobile devices communicate with a smartphone app via Bluetooth and use a smartphone as gateway to upload the raw data to a web-server together with the GPS data from the smartphone. The device itself is small enough to be carried e.g. on a belt. The static nodes send data directly via GPRS/UMTS. There are various servers for the two types of nodes, that further send the data to a central CITI-SENSE server. There are many more nodes available, e.g. for sensing noise that also have their independent web-servers. [18]

Both the mobile [20] and the fixed node [21] use EC sensors for NO and NO_2 measurements.

Fig. 5. In CITI-SENSE, fixed nodes send data to a server via GPRS/UMTS. Mobile nodes send data to a smartphone via Bluetooth which sends the data to a server.

The data are used to create applications in the following fields:

- Personal exposure
- Real-Time AQ information via the mobile node on the smartphone
- Hourly AQ maps through data fusion by all available sensor readings and models[23]
- AQ alert services for citizens, depending on the time of day and past measurements (planned) [19]
- Upload via smartphone your perception of AQ and report possible sources

4) OpenSense: OpenSense is a project in Zurich and Lausanne, where sensor nodes were deployed on trams and buses. In our discussion we will only consider the deployment in Zurich, as described in Reference [22]. Additionally, a mobile node for participative sensing was developed within this project. As the node appeared to be at an early development stage and it only included an O_3 sensor, we will not discuss that device in this publication. OpenSense ran from 2010 to 2013 and is now continued as OpenSense2. We will use both names synonymously.

The aim is to use mobile nodes to understand health impacts of air pollution and the generation of air pollution maps. In Zurich, the network consists of ten trams, with sensor nodes mounted on top of them (cf. Figure 6). The inlet is designed, such that it protects from strong air flow. UFP measurements are carried out using a MiniDisc device and data are available for a period of 2.5 years (5 s resolution). NO_2 was added later and data are available for nine months gathered by EC sensors (10 s temporal resolution). Although the integration of an accurate optical sensor, based on a quantum cascade laser for NO_2 is planned, the authors could not find evidence for the operation of that sensor type.

Data are saved with GPS and time-stamp until a connection is

Fig. 6. In OpenSense, data measured by the tram-mounted nodes, are transferred to the server via GSM or WiFi.

available and then sent to a server via GSM or WiFi. Power was supplied via the tram.

By the help of LUR models the UFP measurements are used to derive pollution maps with a spatial resolution of $100\,m \times 100\,m$. According to the authors, the maps deliver a good quality up to weekly temporal resolution. For higher resolutions, such as semi daily, they have to incorporate past measurements with similar environmental conditions, such as NO_X to achieve acceptable results. Based on the UFP maps, the smartphone app *hRouting – The Health-Optimal Route Planner* was developed, which calculates the health optimal route between two locations. Several methods were investigated to increase the quality of sensor measurements. Within OpenSense, a sensor testbed is operated next to an authority operated measurement station for EC sensors. By that, it is possible to get calibration curves for the EC sensors for every week of the year. The measurements are then post-processed by these optimal calibration curves. We assume, although not clear from the publication, that EC sensors were calibrated that way. Also, a multi-hop calibration algorithm is introduced, to recalibrate the sensor nodes, in vicinity of each other, i.e. measurements are as close as 5 min and 50 m to each other. It was performed on real data for temperature, CO, and O_3 measurements. However, it is noted that on-the-fly calibration may be possible in the future, but adding additional challenges, such as the decision which sensor is more accurate. The calibrated sensor readings are getting error bounds attached. This is done by using reference data from the precise measurement stations, and sensor and phenomenon models.

B. Conclusion on Existing WSNW Projects

In this section, we will critically assess the approaches of the previously introduced projects to improve health effects and air quality. We will underline, that EC sensors are only suitable for a small number of applications, and mobile nodes alone are not sufficient for air quality maps of high temporal resolution.

1) RESCATAME: The project reveals that optimizing traffic flow, with air quality being the objective function, requires more than streets being equipped with low-cost sensor nodes. Firstly, higher accuracy sensors than EC sensors can deliver in real-time (i.e. without post-processing) are necessary.

Secondly, to assess the impact of a traffic control strategy, it is necessary to monitor air pollution also in affected parts of a city. By the way the project was implemented, only local air quality improvements were possible to be monitored.

Thirdly, traffic scenarios were not changed automatically but rather different scenarios were tested, e.g. traffic regulations imposed by local police officers. A suggestion by the authors of this publication, would be by changing the time intervals of the traffic lights according to pollutant concentrations or using LED traffic signs where speed limits can remotely be changed.

In terms of the network structure it is the only project, where nodes do not have direct connection to the web server, but communicate via a router. By that, it is possible decrease the price and the energy consumption of the nodes and make scalability feasible.

2) CamMobSens: For dosage-studies, real-time availability is not required. Therefore, the post-processing routine introduced in Reference [10] for EC sensors could have a big potential for this application.

Data gathered by static nodes equipped with EC sensors lack the same disadvantage as in CITI-SENSE and RESCATAME.

3) CITI-SENSE: The biggest disadvantage of CITI-SENSE are inaccurate EC sensors used in the project. Changing to more dependable sensors, would add a large value to the applications. As a review from Oslo [24] shows: *The high variability in individual sensor performance, as well as the variability in the performance depending on weather conditions or changes in emission patterns, etc. makes low-cost platforms difficult to use for applications when high data quality is necessary*

The inaccurate sensor readings of EC sensors can be sufficient for awareness raising, i.e. a rough indication of AQ, e.g. for real-time AQ alerts.

However, for generating real-time AQ maps, the dependability, specifically of an EC sensor is too low. For mobile nodes and participative sensing, the additional problems of low temporal resolution (concentration may vary greatly with time, according to Reference [10]) and limited trust in sensor readings arise. E.g., people might misapply the sensors, or wear them in a place that is not representative. Also, security is an issue, as the Bluetooth-connection could be hacked to send wrong pollution data.

4) OpenSense: Compared to pedestrian and cyclist carried sensors, OpenSense has the advantage of more accurate position data, as the paths taken by the trams are known and GPS can be assisted. On the other hand, it is highly questionable, whether the area where tram tracks are is representative for areas of the $100\,m \times 100\,m$ size, that are used for averaging. Also, the NO_2 sensor readings need post-processing, which does not allow for real-time applications, which would also not be possible owing to the small number of measurements per time. Therefore, the pollution poor route app, developed in this project, would require higher sensor accuracy, and higher spatial and temporal resolution.

The authors consider a map of NO_2 concentration possible, since members of the same group published a $10\,m \times 10\,m$ NO_2 map based on different measurements in Reference [9].

IV. CHANGING THE GAME

The bottlenecks of existing WSNWs are (i) the accuracy of existing low cost sensors and (ii) the type of WSNW (connected to a lack in either spatial or temporal resolution). We will conclude with an outlook on our plan of a WSNW for monitoring AQ.

A. *Sensor Technology*

As indicated in chapter III-B, there is a limited field of health related applications for EC sensors. Accurate results for EC sensors can only be achieved via post-processing. This is acceptable for dosage and epidemiologic cohort studies. The former by either combining AQ maps of good spatial and temporal resolution with GPS data or using mobile nodes carried by individuals. The latter by using AQ maps with daily resolution (e.g. OpenSense) as stressed in Reference [14].Applications, that require real-time availability of sensor data needs a different sensor technology. Of the aforementioned applications these include:

- Traffic control
- Real-time AQ maps
- Real-time AQ alerts
- Pollution-poor route smartphone app for pedestrians and cyclists

Therefore, we emphasize research in the development of optical low-cost sensors. These sensors can also improve applications, where EC sensors are used, by:

- Not having to go through an expensive calibration procedure for each sensor (CITI-SENSE)
- Not having to use sophisticated post-processing algorithms, that may also lead to artefacts.

B. *Type of WSNW*

As highlighted before, mobile nodes alone and participative sensing are not sufficient for the creation of high resolution pollution maps. Disadvantages are the lack of not covering the whole area (OpenSense), limited temporal resolution, or lacking trust regarding the participants (CITI-SENSE).
On the other hand, they can raise citizens awareness and promote involvement. Also, the AQ at places, where citizens dwell, can be investigated with high spatial resolution.
We therefore suggest a combination of fixed and mobile nodes. Fixed nodes deliver a base coverage of an area with real-time availability of AQ data. Additionally to the above advantages, mobile nodes can assist a fixed sensor network, and help for cross-checking fixed measurements. Also, vehicle mounted, highly accurate sensors, such as a tram with CLD detector as in Reference [5] could optionally be used for recalibrating fixed nodes.

Fig. 7. The goal of our project in terms of sensor-accuracy, and spatial and temporal resolution.

C. *Addressing the Blind Spot: Dependable Sensors and Networks*

A sensor that is sharing the low-cost advantage from EC sensors, but not the disadvantage of instability and cross sensitivity will be a game changer. With such a sensor, we believe to cover the blind spot in terms of accuracy, temporal and spatial resolution, not having been addressed by the reviewed projects (cf. Figure 7). With a low-cost dependable sensor and a combination of a fixed sensor network and later mobile nodes, we can contribute to all aforementioned areas of health benefits for citizens:

- research in sources of high pollution
- awareness raising and tools to avoid high pollution
- research about the adverse health effects of air pollution

Upon the development of a dependable low-cost sensor, we will start to create a WSNW of many dependable low-cost nodes, accompanied by a regular, but sparser repetition of more accurate nodes for uncertainty analysis. We start with a hexagonal close packed (hcp) structure (see Figure 8) to minimize the distance to neighbouring sensors and be able to investigate the dispersion of pollution at sub meter scale in three dimensions. The sensors will be placed close to a linear pollution source (i.e. road). Additionally, the WSNW will be equipped with sensors for other variables, such as wind, temperature and UV light, assumed to be influencing the dispersion of pollutants. By increasing the distance between the nodes, we will then try to optimize the spatial resolution with respect to covering enough details of pollution. The coarse hcp structure will be optimized by adding additional nodes, according to experimental design with respect to the specific terrain. Further we will investigate scale invariances in the network.

The next step is to set up a network of fixed nodes with the optimal distance from the experiments described above in a city. To decrease the cost, similar network technologies as used in the RESCATAME-project (e.g. ZigBee) will be used, in order to minimize the number of router-nodes. In a later stage of the project, low-cost, low-energy mobile nodes shall be accommodated into the network, that connect to the fixed nodes for measurement upload and recalibration.
The requirements for the network structure are given by nodes, that communicate to each other and an optimal number of

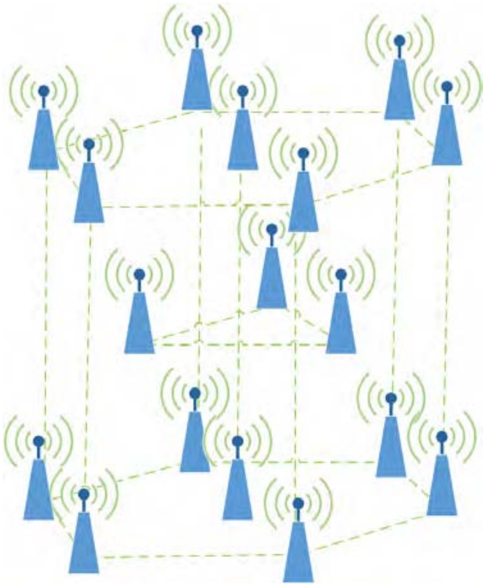

Fig. 8. An hcp network structure is used to minimize the distance to neighbouring sensor nodes.

routers regarding cost efficiency and redundancy. The network has to be dependable at all length scales:

- small distance for dispersion research: competition between the nodes can be problematic
- large distance network: the network must still be dependable: synchronization, redundancy, fault detection, autonomous scanning of the neighborhood and finding the optimal router

V. CONCLUSION

Present WSNWs for monitoring AQ use low-cost sensors to be able to increase the number of nodes. A breakthrough in health-related applications will be reached, if sensor accuracy, temporal and spatial resolution can jointly be improved. Current projects rely on EC sensors, which do not deliver the accuracy necessary to build health-related applications. This bottleneck can be closed by developing low-cost optical sensors.

Spatial and temporal resolution can be increased by combining two types of nodes: (i) fixed higher accuracy nodes for base coverage with uplink and (ii) mobile nodes, that connect with low energy technology to the fixed nodes to upload their data and getting recalibrated.

REFERENCES

[1] (2016, Apr.) Who — ambient and household air pollution and health. [Online]. Available: http://www.who.int/phe/health_topics/outdoorair/databases/en

[2] European Parliament and Council of the European Union, "Directive 2008/50/EC of the European Parliament and of the Council of 21 May 2008 on ambient air quality and cleaner air for Europe," *Official Journal of the European Communities*, pp. 1–43, 2008.

[3] E. E. Agency, *Air quality in Europe*, 2012, no. 9. [Online]. Available: http://www.eea.europa.eu/publications/air-quality-in-europe-2012

[4] E. M. R. Office. (2016) Citi-sense sensor platforms for citizens observatories. [Online]. Available: http://esamultimedia.esa.int/docs/EarthObservation/Sentinel-5p_factsheet_April2016.pdf

[5] S. Umweltforschung, "Messungen der räumlichen Variabilität der Luftqualität in einem Ballungsraum mittels einer Straßenbahn," 2010.

[6] E. P. AG. (2008, Feb.) Eco physics cld 66 leaflet. [Online]. Available: http://www.ecophysics.com/data/leaflets/66-e-v10.pdf

[7] T. D. W. G. o. H. o. D. T. Jaume Targa, Alison Loader. (2008, Feb.) Diffusion tubes for ambient no2 monitoring: Practical guidance for laboratories and users. [Online]. Available: http://laqm.defra.gov.uk/documents/0802141004_NO2_WG_PracticalGuidance_Issue1a.pdf

[8] M. R. Heal and J. N. Cape, "A numerical evaluation of chemical interferences in the measurement of ambient nitrogen dioxide by passive diffusion samplers," *Atmospheric Environment*, vol. 31, no. 13, pp. 1911–1923, 1997.

[9] M. D. Mueller, M. Wagner, I. Barmpadimos, and C. Hueglin, "Two-week NO2 maps for the City of Zurich, Switzerland, derived by statistical modelling utilizing data from a routine passive diffusion sampler network," *Atmospheric Environment*, vol. 106, no. 2, pp. 1–10, 2015. [Online]. Available: http://dx.doi.org/10.1016/j.atmosenv.2015.01.049

[10] M. I. Mead, O. A. M. Popoola, G. B. Stewart, P. Landshoff, M. Calleja, M. Hayes, J. J. Baldovi, M. W. McLeod, T. F. Hodgson, J. Dicks, A. Lewis, J. Cohen, R. Baron, J. R. Saffell, and R. L. Jones, "The use of electrochemical sensors for monitoring urban air quality in low-cost, high-density networks," *Atmospheric Environment*, vol. 70, pp. 186–203, 2013. [Online]. Available: http://dx.doi.org/10.1016/j.atmosenv.2012.11.060

[11] D. P. Peter Woods, Paul Quincey. (2013, Jul.) Description of automated technologies for air pollutants and air quality metrics. [Online]. Available: http://db-airmontech.jrc.ec.europa.eu/download/GASES_MULTIPLE_COMPONENTS_MMTI_DOAS_revised.pdf

[12] M. Goetsch, "Bericht und Auswertung RSD Messungen 2012," 2013. [Online]. Available: http://www.ji.zh.ch/content/dam/baudirektion/awel/luft_asbest_elektrosmog/verkehr/rsd/dokumente/RSD_Bericht_2012.pdf

[13] (2016, May) Cohort study — Wikipedia, the free encyclopedia. [Online]. Available: https://en.wikipedia.org/wiki/Cohort_study

[14] J. Heinrich, E. Thiering, P. Rzehak, U. Krämer, M. Hochadel, K. M. Rauchfuss, U. Gehring, and H.-E. Wichmann, "Long-term exposure to NO2 and PM10 and all-cause and cause-specific mortality in a prospective cohort of women." *Occupational and environmental medicine*, vol. 70, no. 3, pp. 179–86, 2013. [Online]. Available: http://apps.webofknowledge.com/full_record.do?product=UA&search_mode=GeneralSearch&qid=1&SID=V1qvc9o1Ue9MJ9Fk153&page=1&doc=1

[15] (2016, May) Environment - life by theme. [Online]. Available: http://ec.europa.eu/environment/life/project/Projects/index.cfm?fuseaction=home.createPage&s_ref=LIFE08ENV/E/000107&area=2&yr=2008&n_proj_id=3485&cfid=99964&cftoken=663312df0d288b39-D234793A-C9C4-FE9F-153DC2F00E945D0D&mode=print&menu=false

[16] (2016, May) Libelium - smart city project in salamanca to monitor air quality and urban traffic with waspmote. [Online]. Available: http://www.libelium.com/smart_city_air_quality_urban_traffic_waspmote/

[17] F. Garca-Blanch. (2012, Jun.) Citi-sense sensor platforms for citizens observatories. [Online]. Available: http://www.lappeenranta.fi/loader.aspx?id=a226c9ca-f77f-4a2a-8ab8-7c0d7197c0e0

[18] (2016, May) Citi-sense social networking platform. [Online]. Available: http://co.citi-sense.eu

[19] S. A. Alena Bartonova. (2015) Citi-sense information update. [Online]. Available: http://www.citi-sense.eu/Portals/106/Documents/Disseminationmaterial/CITI-SENSE_information_update_15_14.pdf

[20] L. Santiago. (2015) Citi-sense sensor platforms for citizens observatories. [Online]. Available: http://www.gepw8.noa.gr/files/presentations/splinter1/5%20-%20Leonardo%20Santiago.pdf

[21] (2016, May) Aqmesh. [Online]. Available: http://www.aqmesh.com/

[22] D. Hasenfratz, "Enabling Large-Scale Urban Air Quality Monitoring with Mobile Sensor Nodes," Ph.D. dissertation, ETH Zurich, 2015.

[23] W. A. L. Philipp Schneider, Nuria Castell. (2015, Oct.) Making sense of crowdsourced observations: Data fusion techniques for real-time mapping of urban air quality. [Online]. Available: http://congrexprojects.com/custom/15C12/D2_B1_07_1145_Schneider.pdf

[24] (2016, May) Oslo - citizens' observatories with users being parents with children in kindergarten and regular citizens. [Online]. Available: http://co.citi-sense.eu/UsageExamples/Oslo-CitizensObservatorieswithUsersBeingParentswithChildreninKindergartenandRe aspx

D.2 Paper 2

proceedings

Proceedings

A Precise Gas Dilutor Based on Binary Weighted Critical Flows to Create NO_2 Concentrations †

Philipp Breitegger * and Alexander Bergmann

Institute of Electronic Sensor Systems, Graz University of Technology, 8010 Graz, Austria; alexander.bergmann@tugraz.at
* Correspondence: p.breitegger@tugraz.at; Tel.: +43-316-873-3344

† Presented at the Eurosensors 2018 Conference, Graz, Austria, 9–12 September 2018.

Published: 7 December 2018

Abstract: A gas diluter based on critical orifices was built and evaluated. The gas diluter is capable of creating dilution ratios of 1:1400 at a total flow of 6.5 L/min. An extended uncertainty analysis of gas concentrations and dilution ratios according to the Guide to the Expression of Uncertainty in Measurement was conducted. A gas cylinder of 5.16 ppm NO_2 with a relative uncertainty of 1.5% (k = 1) can be diluted down to a concentration of 3.69 ppb NO_2 (dilution ratio of 1:1400) at an uncertainty of 1.9% (k = 1). The results are in good agreement with reference NO_2 measurements, conducted with a chemiluminescence detector (CLD, European reference method EN14211;2005).

Keywords: gas diluter; nitrogen dioxide; metrology

---

1. Introduction

Interests in air quality and exhaust emission measurements have pushed research in new gas sensors. To calibrate and test these sensors, it is necessary to precisely generate gas concentrations over a wide dynamic range. Typical concentrations for environmental NO_2 concentrations are in the range of 0.4 µg m^{-3} (natural background measurements) to 1015 µg m^{-3} (roadside measurements), which requires a dynamic range of more than 1:1000 [1]. Simple solutions, facilitating mass flow controllers, only produce valid dilution ratios down to 1:5 (cf. Ref. [2]). Advanced gas diluters based on capillaries usually do not allow for higher dilution ratios than 1:10. A binary weighted combination of critical orifices, however, allows high dilution rates at low relative errors, as was shown e.g., in Ref. [3].

2. Materials and Methods

Figure 1 shows a schematic drawing of the gas diluter presented in this work. Critical orifices A to K are placed in an aluminum block (grey) and can individually be set to N_2 or NO_2 by ball valves. Orifice diameters are chosen such, that the flow rate through each orifice is doubled compared to the next smaller orifice (numbers next to the letters represent the flow rate relative to orifice A). Only the smallest two orifices (A and B) have the same diameter in order to compare the flow rate through orifices A and B with orifice C. Orifice flows were calibrated by means of a Gilibrator 2 bubble flow meter as a primary standard. Great care was taken to exclusively use gas carrying parts made of PTFE and stainless steel, to enable gas dilution of corrosive gases as well.

Dilution ratios are calculated based on relative flow rates with respect to orifice *A* as described in Ref. [3]. For example, the relative flow rate r_C through orifice *C* is given by Equation (1), where f_A, f_B, and f_C are the measured flow rates through orifices *A*, *B*, and *C*; the flow rate f_{A+B} is the measured flow rate through orifices *A* and *B*, and the relative flow rate r_B is defined as $r_B = \frac{f_B}{f_A}$.

$$r_C = \frac{f_C}{f_{A+B}} \cdot \frac{f_A + r_B \cdot f_A}{f_A} \tag{1}$$

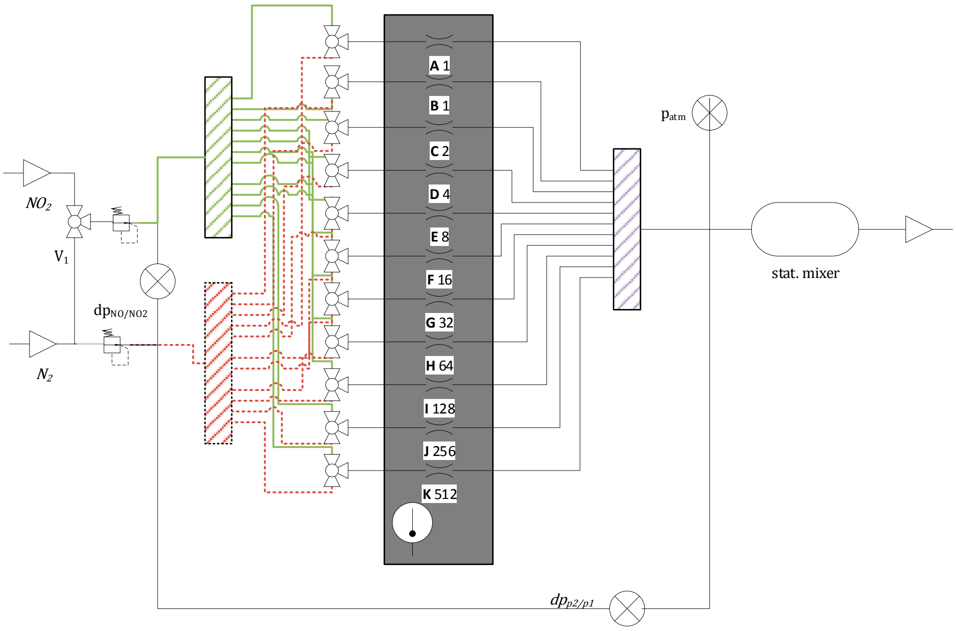

Figure 1. Schematic drawing of the gas diluter. Red dotted lines represent the path of N_2. Green lines represent the path of NO_2. The eleven critical orifices are placed within an aluminum block (grey). Numbers next to the orifice letters represent the flow rate relative to orifice A.

In the same fashion, the remaining relative flow rates can be calculated (cf. Equation (2) for r_D).

$$r_D = \frac{f_D}{f_{A+B+C}} \cdot \frac{f_A + r_B \cdot f_A + r_C \cdot f_A}{f_A} \tag{2}$$

Additionally, all relative flow rates are related to the NO_2 side, as suggested in Ref. [3]. This is done by calculating the average relative flow through each orifice between NO_2 and N_2 side for both sides and additionally weighting the N_2 side with the relation of the maximum total flows

$$\frac{f_{A+\cdots+J,N_2} + f_{K,N_2}}{f_{A+\cdots+J,NO_2} + f_{K,N_2}}.$$

We use eleven orifices with critical flows ranging from 5.833 mL/min to 3.134 L/min. Therefore, a theoretical dilution ratio of 1:1024 is possible. Although precision pressure regulators (LNI Swissgas RP 10) are used on the NO_2 and N_2 side, the upstream pressure is dropping slightly with increasing flow rate. Therefore, all flow rates have to be related to the same upstream pressure. Flow rates can be easily corrected by assuming a linear pressure-flow rate dependency ($\frac{\Delta p}{\Delta F}$), as shown in Equation (3). Each flow rate F_i is related to the upstream pressure at the flow rate through the smallest orifice (F_A), yielding the corrected flow rate F_i' Due to the flow rate corrections the maximum dilution ratio is 1:1400. To compensate the cooling effect as consequence of gas expansion, the critical orifices are embodied in a solid, temperature regulated aluminum block, conditioned at 30 °C.

$$F'_i = F_i \cdot \frac{p_i - F_A \frac{\Delta p}{\Delta F}}{p_i - F_i \frac{\Delta p}{\Delta F}} \tag{3}$$

All pressure sensors are equipped with analog outputs. Data acquisition of the pressure measurements was performed using analog inputs of an NI USB-6009. Atmospheric pressure (p_{atm} in Figure 1) was measured with a MPX5100AP (NXP) absolute pressure sensor. The differential pressure between N_2 and NO_2 ($dp_{NO/NO2}$) was controlled with a TSCSNBN 005 (Honeywell) sensor. The differential pressure between upstream and downstream ($dp_{p2/p1}$) was measured using a 26PCDFA6D (Honeywell) sensor.

3. Results

To validate the gas diluter, 5.16 ppm NO_2 in synthetic air (1.5% relative uncertainty (k = 1), standard gas cylinder) was diluted with N_2 and measured with a CLD (API T200). Uncertainties of NO_2 concentrations were calculated according to the Guide to the expression of uncertainty of measurement for the combined standard uncertainty of uncorrelated input quantities (chapter 5.1 of Ref. [4]), using GUM Workbench Professional Version 2.4 (Metrodata GmbH). The resulting NO_2 concentrations and the corresponding uncertainties are depicted in Table 1. The largest uncertainty contribution stems from the concentration of the NO_2 gas cylinder. This explains the small increase in relative uncertainty with increasing dilution ratio, i.e., decreasing NO_2 concentration.

Table 1. Calculated NO_2 concentrations and uncertainties in parts per billion (ppb) and percent (%).

Concentration [ppb]	Uncertainty, k = 1 [ppb]	Relative Uncertainty, k = 1 [%]
3.69	0.069	1.9
12.2	0.22	1.8
31.4	0.56	1.8
70.6	1.2	1.7
154.2	2.7	1.8
312	5.3	1.7
652	11	1.7
1265	20	1.6
2686	42	1.6

To analyse gas concentrations generated with the gas diluter, the difference between theoretical and measured gas concentrations are depicted as a function of the theoretical gas concentrations in Figure 2. Error bars of the CLD were calculated according to the API T200 specifications [5]. Good agreement was achieved for concentrations up to 652 ppb. As the CLD was spanned with a 836 ppb bottle, measurements above 1000 ppb are extrapolated, explaining the deviation of the 1265 ppb measurement.

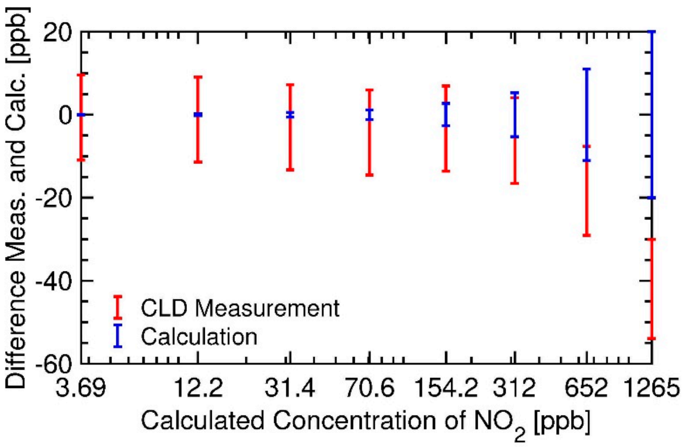

Figure 2. Deviation of the measured from the calculated concentrations (*x*-axis). Calculated (blue) and measured (red) values are shown with corresponding error bars and are baseline corrected to zero.

As a result of the high dynamic range, the flow through the smallest orifice (A) is only $^1/_{500}$ of the largest orifice (K). The timeseries of a measurement where valve A was switched from N_2 to NO_2 (Figure 3), shows that a 30 min waiting time is necessary to obtain stable concentrations.

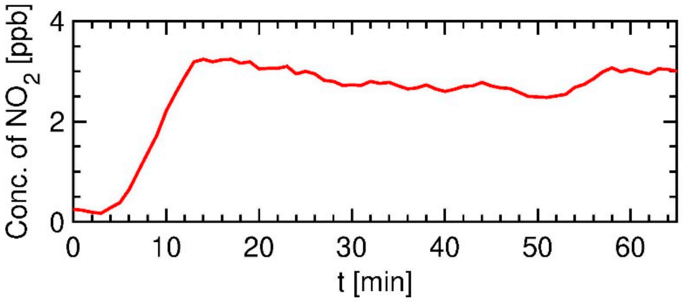

Figure 3. Valve A is switched from N_2 to NO_2. Due to the low flow rate of the smallest orifices, 30 min waiting time is necessary for achieving a stable concentration.

4. Discussion

The gas diluter presented in this work was successfully evaluated by diluting NO_2 with N_2 and measuring the resulting concentrations with an API T200 CLD. All generated concentrations were within the error of the CLD and the gas diluter. However, the high dilution rates of the diluter come with the disadvantage of low gas exchange time.

Funding: This research received no external funding.

Acknowledgments: We thank Metrodata GmbH for the provision of GUM Workbench Professional Version 2.4. We also thank the Institute of Internal Combustion Engines and Thermodynamics (FVT) from TU Graz for providing us a calibrated API T200 chemiluminescence detector and their knowledge of operating it.

Conflicts of Interest: The authors declare no conflict of interest. The founding sponsors had no role in the design of the study; in the collection, analyses, or interpretation of data; in the writing of the manuscript, and in the decision to publish the results.

References

1. World Health Organization. Regional Office for Europe. Nitrogen dioxide. In *Air Quality Guidelines for Europe*; Frank Theakston; World Health Organization, Regional Office for Europe: Copenhagen, Denmark, 2000; p. 175, ISBN 92-890-1358-3.
2. Wiegleb, G. Kalibrierung und Prüfverfahren. In *Gasmesstechnik in Theorie und Praxis*; Springer Fachmedien: Wiesbaden, Germany, 2016; Volume 1, pp. 713–714; ISBN 978-3-658-10687-4.
3. Brewer, P.J.; Goody, B.A.; Gillam, T.; Brown, R.J.C.; Milton, M.J.T. High-accuracy stable gas flow dilution using an internally calibrated network of critical flow orifices. *Meas. Sci. Technol.* **2010**, *21*, 115902, doi:10.1088/0957-0233/21/11/115902.
4. JCGM/WG 1. *Guide to the Expression of Uncertainty in Measurement*, 1st ed.; Bureau international des poids et mesures: Sèvres, France, 2008.
5. The Model T200 Chemiluminescence NO/NO_2/NO_x Analyzer. Available online: http://www.teledyne-api.com/prod/Downloads/SAL000046F%20-%20T200.pdf (accessed on 16 June 2018).

D.3 Paper 3

sensors

Article

Intensity Modulated Photothermal Measurements of NO_2 with a Compact Fiber-Coupled Fabry–Pérot Interferometer

Philipp Breitegger *, Benjamin Lang and Alexander Bergmann

Institute of Electronic Sensor Systems, Graz University of Technology, Graz 8010, Austria
* Correspondence: p.breitegger@tugraz.at; Tel.: +43-316-873-3344

Received: 27 June 2019; Accepted: 27 July 2019; Published: 30 July 2019

Abstract: Sensors for the reliable measurement of nitrogen dioxide concentrations are of high interest due the adverse health effects of this pollutant. This work employs photothermal spectroscopy to measure nitrogen dioxide concentrations at the parts per billion level. Absorption induced temperature changes are detected by means of a fiber-coupled Fabry–Pérot interferometer. The small size of the interferometer enables small detection volumes, paving the way for miniaturized sensing concepts as well as fast response times, demonstrated down to 3 s. A normalized noise equivalent absorption of $7.5 \times 10^{-8}\,\mathrm{cm}^{-1}\mathrm{W}/\sqrt{\mathrm{Hz}}$ is achieved. Additionally, due to the rigid structure of the interferometer, the sensitivity to mechanical vibrations is shown to be minor.

Keywords: nitrogen dioxide; photothermal interferometry; gas sensor; optical microphone

---

1. Introduction

Due to the adverse health effects of NO_2 [1], monitoring ambient NO_2 concentrations as well as NO_2 emissions from vehicles is of interest for citizens, researchers, and legislative purposes [2–5]. WHO recommends an hourly mean of 200 µg m^{-3} (106.4 ppb) and an annual mean of 40 µg m^{-3} (21.3 ppb) not to be exceeded [1]. A variety of sensing principles exist for the sensing of NO_2. For example, electrochemical and metal oxide sensors are low-cost, but lack sensitivity, selectivity, and long-term stability [6]. On the other hand, chemiluminescence detectors are expensive and large in size, but offer reliable measurements and are commonly used to measure NO_2 concentrations for legislative purposes [5]. Further, optical sensors exist, which provide high spectral selectivity by choosing a light source that matches one or more absorption bands of NO_2. Among those are photoacoustic and photothermal sensing concepts.

Photoacoustic spectroscopy uses intensity or wavelength modulated light sources, which match one ore more absorption bands of the gas of interest, exciting transitions into higher molecular energy levels. Subsequent collisional deactivation leads to the production of a fast decaying thermal and a propagating, slowly decaying acoustic wave [7]. The detection of the acoustic wave, usually after acoustically resonant amplification, is utilized in photoacoustic spectroscopy [8–10] and quartz-enhanced photoacoustic spectroscopy [11–14].

This work focuses on an interferometric detection scheme, where the temperature change is measured by a refractive index change, induced by the absorption-based heating. As an excitation source, we use an intensity modulated 450 nm laser. The generated refractive index change is measured by means of a fiber-coupled Fabry–Pérot interferometer as the sensing element. Previous publications have demonstrated noise equivalent absorptions of $1.3 \times 10^{-7}\,\mathrm{cm}^{-1}\mathrm{W}/\sqrt{\mathrm{Hz}}$ with intensity modulation for NO_2 (equal to 700 ppb for 30 mW average laser power) [15] and $1.8 \times 10^{-6}\,\mathrm{cm}^{-1}\mathrm{W}/\sqrt{\mathrm{Hz}}$ [16] or $7.5 \times 10^{-9}\,\mathrm{cm}^{-1}\mathrm{W}/\sqrt{\mathrm{Hz}}$ [17], with wavelength modulation for detection of SO_2. Similar normalized noise equivalent absorptions (NNEAs) can be achieved with microstructured hollow-core fibers in combination with photothermal interferometry [18,19]. The response of hollow-core fiber gas sensors, however, is diffusion limited and response times for long, high-sensitivity fibers are usually limited to several tens of seconds [18,20]. Exceptions with response times down to 3 s and detection limits of $7.4 \times 10^{-5}\,\mathrm{cm}^{-1}$ for methane have been reported for short fibers [18,21], but lacking statements about the laser power coupled into the fiber prohibit a comparison to other methods.

In this work, we demonstrate sensing of NO_2 by photothermal interferometry, utilizing a membrane-free optical microphone as interferometer. The $1\,\sigma$ detection limit for 1 s integration time is 348 ppb, equal to a normalized noise equivalent absorption of $7.5 \times 10^{-8}\,\mathrm{cm}^{-1}\mathrm{W}/\sqrt{\mathrm{Hz}}$. The work is meant to demonstrate the advantages of photothermal interferometry for NO_2, such as miniaturization potential of the sensing volume, fast response times, and a robust setup.

2. Materials and Methods

2.1. Photothermal Interferometry

In this work, photothermal interferometry (PTI) is realized with a fiber-coupled Fabry–Pérot interferometer (FPI). Intensity modulation of the 450 nm excitation laser produces a thermal wave, with a temperature change directly proportional to the concentration of NO_2 [22]. The thermal wave is heavily damped, and is therefore only observed close to the probe beam [7]. The local heating leads to a change in refractive index Δn, described by the Clausius–Mosotti equation [22], with ΔT temperature rise and T_{abs} absolute temperature of the gas:

$$\Delta n = -(n-1)\frac{\Delta T}{T_{abs}}. \tag{1}$$

Due to the constant gas flow through the cell, incremental heating of the gas sample due to the excitation laser can be neglected and constant absolute temperature of the gas can be assumed in our experiments. Hence, the detected change in refractive index is directly proportional to the NO_2 concentration within the FPI cavity.

The FPI used for this work measures the intensity of the reflected probe laser. The reflected intensity I_r is given by [23]

$$I_r = I_i\left(1 - \frac{1}{1 + F\sin^2(\delta/2)}\right), \tag{2}$$

where I_i is the incident intensity and F is the finesse of the mirrors. The phase shift δ depends on the refractive index in the cavity n, the distance between the mirrors d, and the wavelength λ as

$$\delta = \frac{4\pi n d}{\lambda}. \tag{3}$$

Changes in n change the phase shift δ and, thus, the reflected intensity I_r.

2.2. Experimental Setup

For this work, a commercial optical microphone was used as detector, which consists of a fiber-coupled FPI cavity, machined as a rigid structure, which offers low sensitivity to mechanical vibrations [24]. The FPI is formed by a machined opening with semitransparent mirror surfaces, each approximately 1.5 mm × 1.5 mm in size, which are facing parallel to each other at a distance of approximately 3.3 mm. A 1550 nm probe laser of 1 mW optical power is reflected back and forth between the mirrors, and the reflected intensity is measured [24]. The probe laser is of approximately Gaussian shape, with 205 µm full width at half maximum within the cavity, and the reflectivity of the etalon mirrors is in the range of 0.6 [25]. The commercial microphone head comes with protective membranes covering the cavity, which were removed to allow for a free gas exchange and an overlap of the probe and excitation beams (cf. Figure 1).

The optical microphone is placed in a 3D-printed cell with a sample volume smaller than 9 cm^3 (Figure 1). The cell was optimized with multiphysical simulations to suppress unwanted acoustic resonances. The beam of the excitation laser (blue) is focused through a window and horizontally centered to cross the probe laser of the optical microphone at the position of maximum intensity. A neutral density (ND) filter is mounted opposite the window to attenuate the excitation beam. A 40 mW continuous-wave optical power laser module (Laser Components GmbH, Olching, Germany: FLEXPOINT® Dot Laser Module) with 450 nm wavelength serves as excitation laser. At this wavelength, NO_2 yields high absorption with little cross-sensitivity to other gases. Also, this wavelength is above the photodissociation threshold [26].

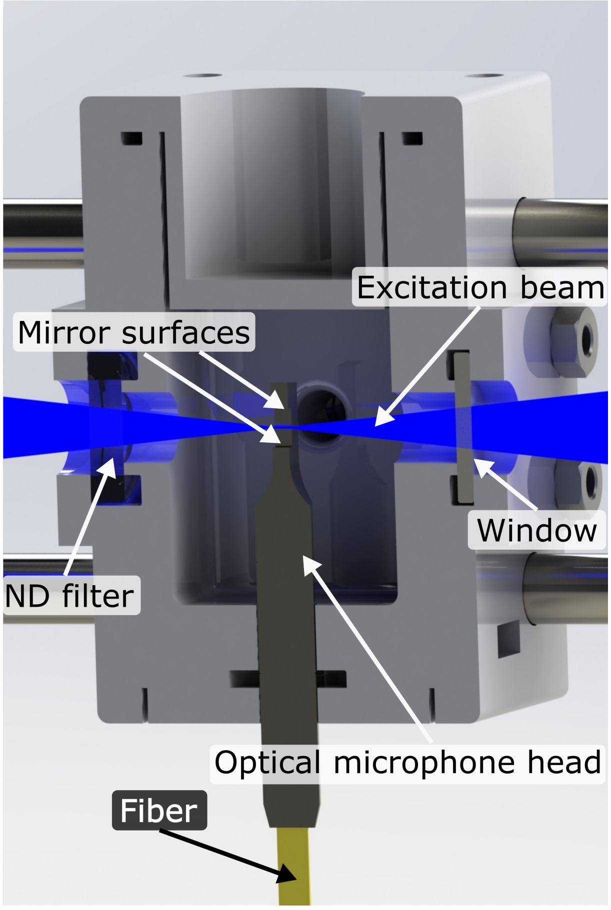

Figure 1. Cut through the 3D-printed cell, carrying the head of the optical microphone. Excitation laser beam is shown in blue. The probe beam is reflected within the microphone cavity between the top and bottom mirror surfaces.

The experimental setup allows to study the sensor response for different concentrations of NO_2, flow rates, and modulation frequencies. This is shown in Figure 2. Gas mixtures were produced with a temperature stabilized custom gas diluter based on binary weighted critical orifices [27], which offer low uncertainties over a broad range of dilution ratios. The NO_2 gas cylinder contains a mixture of NO_2 and synthetic air (Messer Austria GmbH, Gumpoldskirchen, Austria: 19.2 ppm NO_2), which was further diluted with synthetic air (Messer Austria GmbH: Synthetic Air, Scientific). The flow rate to the PTI cell is controlled by a mass flow controller (MFC; Vögtlin, Aesch, Switzerland: Model GSC-B).

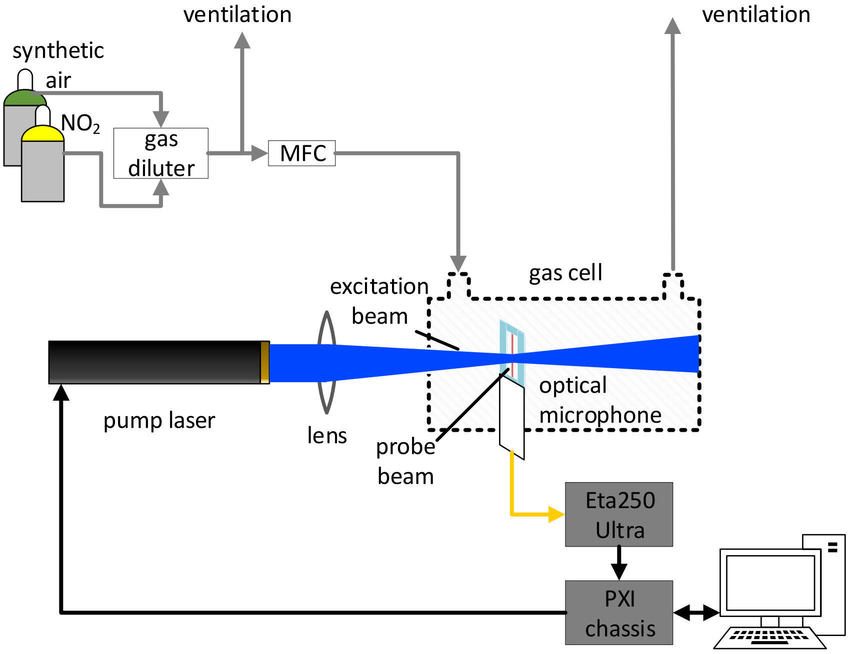

Figure 2. Schematic of the experimental setup for characterizing the photothermal interferometry setup with NO_2. Gas mixtures are created with a gas diluter. The excitation beam is perpendicular to the probe beam and is focused and centered into the cavity of the optical microphone.

The signal from the optical microphone control unit (XARION Laser Acoustics GmbH, Vienna, Austria: Eta 250 Ultra—settings: Cutoff frequency 100 Hz, gain 20 dB) is recorded with a data acquisition card (National Instruments, Austin, TX, United States: Model PXI-6281) at 250 ksps and post-processed on a personal computer (PC). The same chassis carrying the PXI-6281 also houses a function generator (National Instruments: Model PXI-5402). The function generator provides the square-wave modulation signal (duty cycle 50%) for the excitation laser. The PTI signal is filtered with a digital lock-in amplifier, realized in LabVIEW code on a PC, with an integration time of 1 s. Due to the high sampling rate and limited buffer size of the DAQ card, data acquisition and modulation is stopped and restarted after each measurement to obtain a constant phase relation.

To investigate the sensitivity of the FPI and the signal to mechanical vibrations, the sensor was mounted on a platform connected to an electrodynamic shaker (TIRA GmbH, Schalkau, Germany: TIRAvib S502). Applied vertical accelerations and vibration spectral densities were measured with a piezoelectric accelerometer (PCB Piezotronics Inc., Depew, NY, United States: 333B30) placed next to the cell mounting, as shown in Figure 3. In this configuration the operating sensor was exposed to two different broadband quasi-random vibration distributions over the frequency range of 1 Hz to 500 Hz—characteristic for highway truck vibration exposure [28]—to test mobile operation of the PTI sensor. The sensor was exposed to the acceleration spectra at different root mean square accelerations for several minutes and signal noise was recorded at multiple points in time. Additionally, the sensor was accelerated sinusoidally and maximum tolerable vertical accelerations (insignificantly increased signal noise) at a range of frequencies between 10 Hz and 300 Hz were determined. Due to the low anticipated effect on the noise level, the interferometer interrogation unit was not exposed to the vibrations.

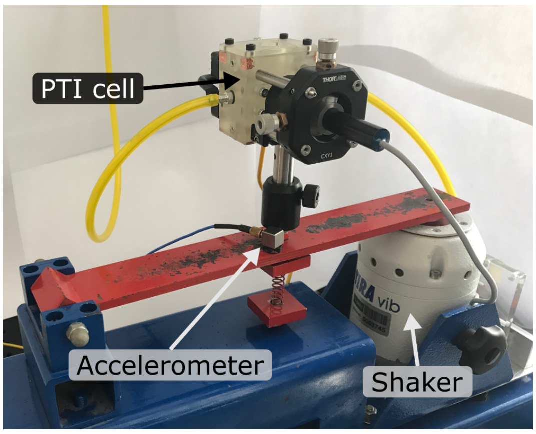

Figure 3. Photograph of the vibration test setup, showing the full photothermal interferometry (PTI) cell with gas lines and laser, mounted on an electrodynamic shaker. The piezoelectric accelerometer, measuring applied accelerations, is placed next to the cell mounting.

3. Results

3.1. Influence of Flow Rate on Sensor Noise

The selection of the flow rate is a balance of response time and detection limit, as higher flow rates offer faster gas exchange rates, but are associated to higher flow noise, which negatively effect the detection limit. Figure 4 shows the noise spectrum of the flow noise, measured by the optical microphone without the excitation laser being switched on. The noise spectrum was calculated as the Welch power spectral density estimate with a 0.5 s Hanning window. The flow rate was varied between 0.2 slpm and 4 slpm. Only a slight increase in noise is seen up to flow rates of 1 slpm, but higher flow rates significantly increase present $1/f^{\alpha}$ noise [29] and are accompanied by flow-rate-dependent tonal noise.

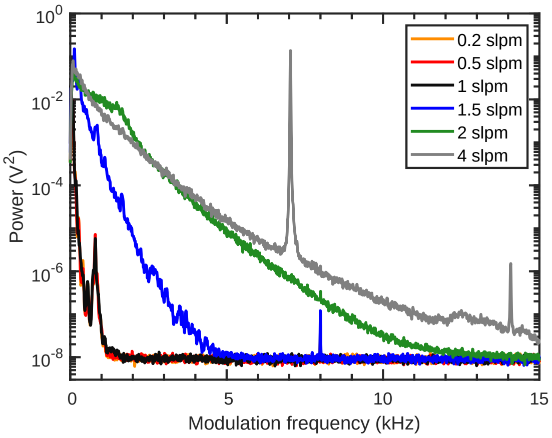

Figure 4. Welch spectra of the background noise without excitation laser at different flow rates. Welch spectra are calculated over 0.1 s windows and averaged over 9 s. The noise spectra of 0.2 slpm and 0.5 slpm are identical and covered by the spectrum at 1 slpm.

Due to the small cell volume of less than 9 cm^3, a flow rate of 0.5 slpm with a nominal gas exchange rate of ≈1 s/cell volume was considered sufficient with a 1 s integration time, and was used in the subsequent measurements.

3.2. Selection of the Optimal Modulation Frequency

From Figure 4, the additional presence of flow-rate-independent noise around 800 Hz is visible, and a higher modulation frequency should be chosen. However, as the photothermal signal is inversely proportional to the modulation frequency [22], a low modulation frequency is desired. Therefore, the signal with 19.2 ppm NO_2 (black circles) and the background noise with synthetic air (blue diamonds) was recorded with the lock-in amplifier for different modulation frequencies (Figure 5a). The inverse signal strength of the photothermal signal can nicely be seen (black circles). To find the optimal modulation frequency, the signal-to-noise ratio (SNR) was calculated (black dots in Figure 5b). Due to the variation in the calculated SNR values, a moving average filter was applied (blue curve) and a modulation frequency of 1.4 kHz, in the region where best results were achieved, was selected.

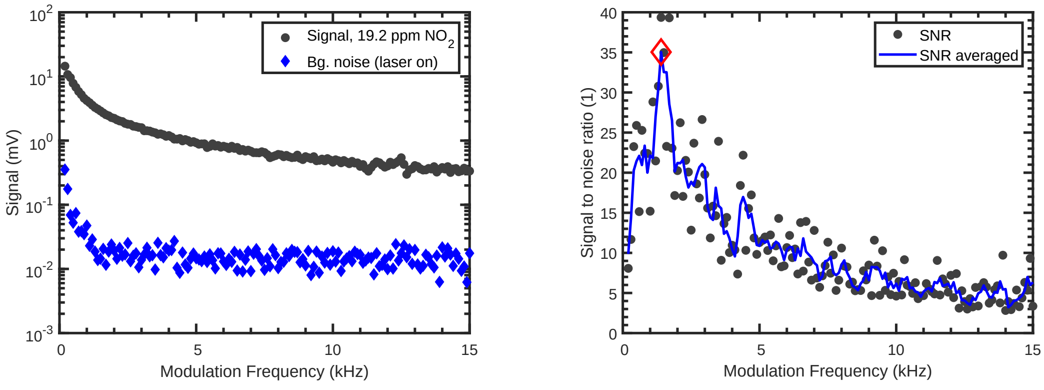

(**a**) (**b**)

Figure 5. Noise investigations of the PTI sensor: (**a**) Signal with 19.2 ppm NO_2 (black circles), background noise for different modulation frequencies with the laser switched on (blue diamonds), measured with lock-in amplifier. Background noise with the laser switched off equals the noise with the modulated laser switched on. (**b**) Signal-to-noise ratio as a function of the modulation frequency. The selected modulation frequency is marked with a red diamond.

3.3. Limit of Detection and Long Term Stability

The linearity of the PTI sensor was confirmed by applying concentrations ranging from 606 ppb to 19.2 ppm NO_2 to the sensor. The PTI signal, as a function of applied NO_2 concentration, is shown in Figure 6. Each data point was averaged for approximately 40 values, i.e., 40 s. All signals are background-corrected with respect to their phase. The sensitivity was determined to be $(0.149 \pm 0.002)\,\mathrm{mV\,ppm^{-1}}$ from a weighted linear regression. The coefficient of determination for the fit is $R^2 = 0.999$.

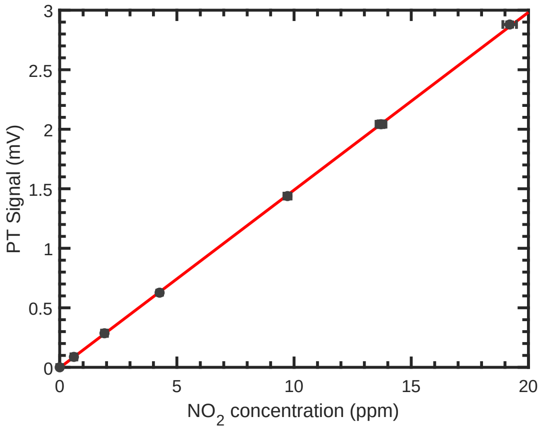

Figure 6. Linear fit (red) of the background-corrected photothermal signal as a function of the NO_2 concentration. Error bars of the photothermal signals are the standard deviation relative to the mean. Error bars of the concentrations are too small to be visible on this scale.

Long-term stability was investigated by calculating the Allan deviation for the signal at constant flow of synthetic air. The corresponding plot is shown in Figure 7. Even though the sensor was mounted on an optical table without vibration isolation, no interferences from mechanical vibrations were observed, due to the rigid structure of the FPI.

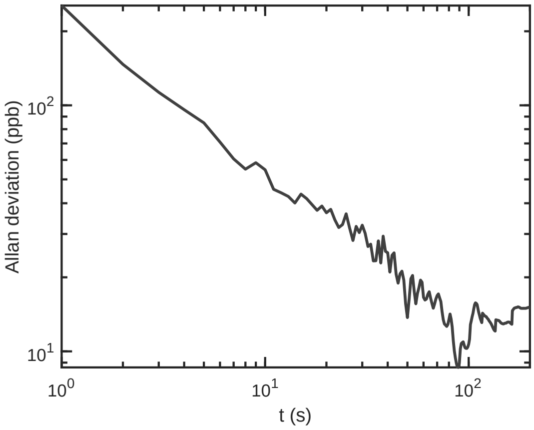

Figure 7. Allan deviation of the photothermal signal in units of NO_2 concentration as a function of averaging time. Allan deviation was calculated with MATLAB.

From Figure 7, it can be seen that the 1σ detection limit is 348 ppb for 1 s averaging time. The detection limit can be further improved to 75 ppb (10 s) and 26 ppb (100 s), by using longer averaging times. The increase in standard deviation after approximately 200 s, and the therefore limited maximum integration time, stems from the laser module, which is not temperature stabilized (cf. Appendix A). This, however, could be easily improved by changing to a temperature stabilized laser. The optical microphone itself uses a feedback current to stabilize the wavelength of the probe laser to maintain a steady operating point, i.e., compensating for slow temperature and pressure changes [24].

The normalized noise equivalent absorption was calculated by assuming a Gaussian wavelength distribution around 450 nm with FWHM of 0.5 nm, and using the corresponding absorption coefficient from the HITRAN database [30]. For 1 s integration time of the lock-in amplifier, this corresponds to an NNEA of $7.5 \times 10^{-8}\,\mathrm{cm}^{-1}\mathrm{W}/\sqrt{\mathrm{Hz}}$.

Low sensitivity of the PTI sensor to mechanical vibrations is essential for mobile applications and is usually hard to achieve for interferometric setups. Results of the vibration analysis, however, suggest low sensitivity of the proposed interferometric sensor concept, due to the rigid structure of the FP cavity. Figure 8a shows the applied acceleration spectral densities in the frequency range of interest and, for comparison purposes, a military standard vibration schedule for highway truck vertical vibration exposure, often used for commercial product testing (MIL-STD-810H, Method 514.8C-I [28]). The peak visible at 50 Hz in both spectra is noise at the power line frequency, amplified by the accelerometer amplifier, and has to be disregarded from the acceleration spectrum. Although a strong mechanical resonance of the setup is excited near 150 Hz for vibrations up to 500 Hz (black curve), the measured signal noise level only increases marginally from 30 µV to 40 µV. During application of the low-frequency vibration spectrum with components up to 100 Hz (yellow curve), no changes in the measured noise level were observed and the noise remained at the background level.

Achieved peak accelerations for sinusoidal vibrations are plotted in Figure 8b together with the measured noise. It can be seen that, for frequencies between 20 Hz and 300 Hz, the PTI sensor was exposed to accelerations at or above 0.5 g up to 1.7 g, with the noise level still well within the 3σ noise band. At 10 Hz, the large motion amplitude of the electrodynamic shaker was causing a repeated mechanical impulse to the PTI setup, and applied peak accelerations were reduced to prevent impulse excitation.

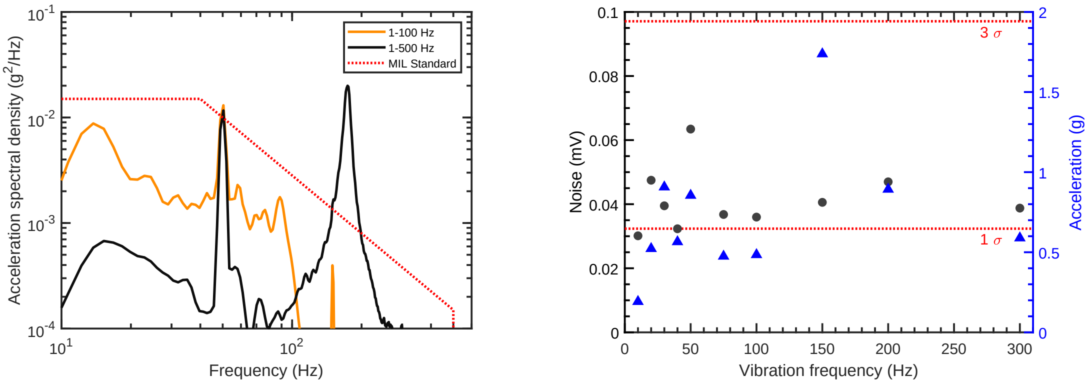

(**a**) (**b**)

Figure 8. Vibration analysis: (**a**) Broadband acceleration spectral densities applied to the measurement setup during operation (yellow and black curves). Military standard vibration schedule for highway truck vertical vibration exposure (MIL-STD-810H, Method 514.8C-I [28]; red dotted line). (**b**) Measured signal noise (black circles) at the applied sinusoidal vertical peak accelerations (blue triangles) for zero air. Horizontal dotted lines mark 1 σ and 3 σ noise levels.

3.4. *Response Time*

As short response times are critical for a wide variety of applications, the response of the proposed PTI sensor to steps in concentration was investigated. Repeated steps from synthetic air (zero concentration) to concentrations of 19.2 ppm NO_2 at 0.5 slpm and 1 s integration time revealed reproducible response times to 90% signal level (τ_{90}) below 3 s; and recovery times to 10% signal level (τ_{10}) below 2 s. An exemplary response curve is shown in Figure 9.

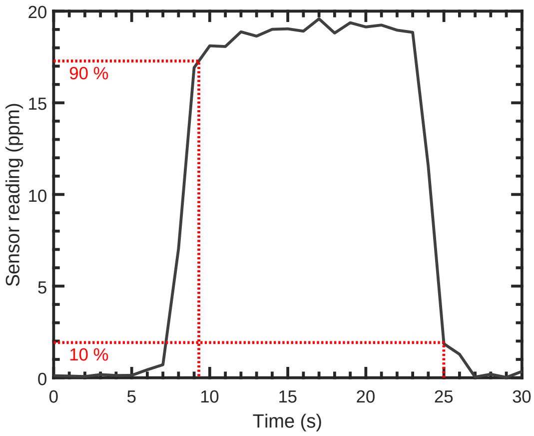

Figure 9. Sensor step response for a step from zero air to a concentration of 19.2 ppm NO_2 and back at 0.5 slpm and 1 s integration time. Response time to 90% (τ_{90}) and recovery time to 10% (τ_{10}) signal level are below 3 s and 2 s, respectively.

4. Discussion and Conclusions

The presented sensor concept, using a compact fiber-coupled Fabry–Pérot interferometer for photothermal spectroscopy, offers a reliable sensing scheme for NO_2 with high spectral selectivity and sensitivity. The NNEA was determined to be $7.5 \times 10^{-8}\,\mathrm{cm^{-1}W/\sqrt{Hz}}$, which is lower than previous PTI implementations [15,16], but can still be improved in future realizations, e.g., by applying a balanced detection scheme [17].

QEPAS implementations reach slightly better NNEAs (e.g., $2.5 \times 10^{-8}\,\mathrm{cm^{-1}W/\sqrt{Hz}}$ [10], $4.2 \times 10^{-9}\,\mathrm{cm^{-1}W/\sqrt{Hz}}$ [13]) and, compared to conventional PAS implementations, the NNEA is up to a factor 100 worse ($7.0 \times 10^{-10}\,\mathrm{cm}^{-1}\mathrm{W}/\sqrt{\mathrm{Hz}}$ [10]). However, the proposed PTI sensor approach offers the possibility for a much smaller detection volume, capable of faster response times and higher miniaturization potential.

The developed, non-optimized cell has a volume smaller than $9\,\mathrm{cm}^3$, for which an integration time of 1 s combined with a flow rate of 0.5 slpm proved to provide a good balance of response time and detection limit. Even though the given cell geometry comprises poorly flushed dead volumes, a response time of $\tau_{90} = 3\,\mathrm{s}$ and a recovery time of $\tau_{10} = 2\,\mathrm{s}$ were achieved. For applications requiring faster response times, a combination of smaller integration time and higher flow rate can be easily realized. Due to the small size of the optical microphone, the cell volume could be ultimately decreased to the dimensions of the FPI cavity, which is $1.5\,\mathrm{mm} \times 1.5\,\mathrm{mm} \times 3.3\,\mathrm{mm} \approx 7.5\,\mathrm{mm}^3$, without major drawbacks. This is highly advantageous when compared to microstructured hollow-core fiber-based PTI approaches, where long fibers are needed to reach comparable NNEAs. To fully demonstrate the miniaturization potential of the presented method, future research should focus on the downscaling of the cell down to the FPI cavity volume.

On the other hand, applications like environmental monitoring require lower detection limits, at averaging times of up to one hour [5]. In this case, a stabilized laser source could be used, which would enable longer averaging times to improve the detection limit. Additionally, higher laser power could be used to improve the detection limit, as the photothermal signal scales directly with the laser power.

A low sensitivity of the PTI sensor to mechanical vibrations was demonstrated with broadband vibrations in a frequency range similar to vehicular vibration profiles. Although the applied vibration power was below the specified root mean square acceleration of $g_{rms} = 1.04\,\mathrm{g}$ in the cited military vibration test standard, future commercial application possibilities in mobile gas sensing should be realizable with minor improvements in setup stability. This is underlined by the fact that, for sinusoidal vibrations, peak accelerations of 1.7 g could be applied to the described setup, without significantly increasing signal noise.

Although an expensive lab grade optical microphone was used for the proof of principle experiments, chip-level miniaturization of the sensor is possible, offering interesting potential for large-scale production of the sensor. Possible fields of application include exhaust gas and emission measurements. Furthermore, measurement of different gases can easily be achieved by using excitation lasers of different wavelengths.

Author Contributions: Conceptualization, P.B. and B.L.; methodology, P.B. and B.L.; software, P.B.; validation, P.B., B.L., and A.B.; formal analysis, P.B. and B.L.; investigation, P.B. and B.L.; resources, P.B., B.L., and A.B.; data curation, P.B. and B.L.; writing—original draft preparation, P.B.; writing—review and editing, P.B., B.L., and A.B.; visualization, P.B. and B.L.; supervision, A.B.; project administration, A.B.

Funding: This research received no external funding.

Acknowledgments: The authors would like to thank Wolfgang Rohringer and Balthasar Fischer from XARION Laser Acoustics GmbH for the constructive discussions. Open access publication is supported by the TU Graz Open Access Publishing Fund.

Conflicts of Interest: The authors declare no conflict of interest.

Abbreviations

The following abbreviations are used in this manuscript:

PTI	photothermal interferometry
PAS	photoacoustic spectroscopy
QEPAS	quartz-enhanced photoacoustic spectroscopy
ksps	kilosamples per second
NNEA	noise normalized equivalent absorption

Appendix A. Drift of the Laser Power

To investigate whether drift is dominated by fluctuations of the laser power, an Allan deviation analysis was carried out. As can be seen in Figure A1, a drift of the laserpower is appearing at the same timescale as the drift of the FPI sensor (around 200 s), which indicates that drift is caused by fluctuations of the laser power.

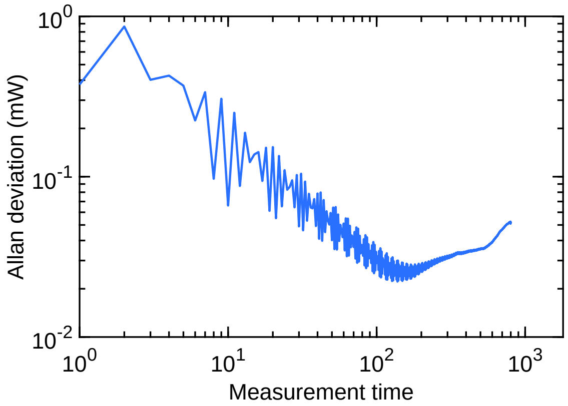

Figure A1. Allan deviation of the laser power as a function of the averaging time.

References

1. World Health Organisation. *Air Quality Guidelines for Particulate Matter, Ozone, Nitrogen Dioxide and Sulfur Dioxide—Global Update 2005*; WHO Press: Geneva, Switzerland, 2006.
2. Wild, R.J.; Dubé, W.P.; Aikin, K.C.; Eilerman, S.J.; Neuman, J.A.; Peischl, J.; Ryerson, T.B.; Brown, S.S. On-road measurements of vehicle NO2/NOx emission ratios in Denver, Colorado, USA. *Atmos. Environ.* **2017**, *148*, 182–189, doi:10.1016/j.atmosenv.2016.10.039. [CrossRef]
3. Hagemann, R.; Corsmeier, U.; Kottmeier, C.; Rinke, R.; Wieser, A.; Vogel, B. Spatial variability of particle number concentrations and NOx in the Karlsruhe (Germany) area obtained with the mobile laboratory 'AERO-TRAM'. *Atmos. Environ.* **2014**, *94*, 341–352.10.1016/j.atmosenv.2014.05.051. [CrossRef]
4. Mead, M.I.; Popoola, O.A.M.; Stewart, G.B.; Landshoff, P.; Calleja, M.; Hayes, M.; Baldovi, J.J.; McLeod, M.W.; Hodgson, T.F.; Dicks, J.; et al. The use of electrochemical sensors for monitoring urban air quality in low-cost, high-density networks. *Atmos. Environ.* **2013**, *70*, 186–203.10.1016/j.atmosenv.2012.11.060. [CrossRef]
5. European Parliament, Council of the European Union. Directive 2008/50/EC of the European Parliament and of the Council of 21 May 2008 on ambient air quality and cleaner air for Europe. *Off. J. Eur. Union* **2008**, *L 152*, 1–44.
6. Castell, N.; Dauge, F.R.; Schneider, P.; Vogt, M.; Lerner, U.; Fishbain, B.; Broday, D.; Bartonova, A. Can commercial low-cost sensor platforms contribute to air quality monitoring and exposure estimates? *Environ. Int.* **2017**, *99*, 293–302.10.1016/j.envint.2016.12.007. [CrossRef] [PubMed]
7. Miklós, A.; Hess, P.; Bozóki, Z. Application of acoustic resonators in photoacoustic trace gas analysis and metrology. *Rev. Sci. Instrum.* **2001**, *72*, 1937–1955.10.1063/1.1353198. [CrossRef]
8. Kalkman, J.; van Kesteren, H. Relaxation effects and high sensitivity photoacoustic detection of NO2 with a blue laser diode. *Appl. Phys. B* **2008**, *90*, 197–200.10.1007/s00340-007-2895-0. [CrossRef]
9. Yin, X.; Dong, L.; Wu, H.; Zheng, H.; Ma, W.; Zhang, L.; Yin, W.; Jia, S.; Tittel, F.K. Sub-ppb nitrogen dioxide detection with a large linear dynamic range by use of a differential photoacoustic cell and a 3.5 W blue multimode diode laser. *Sens. Actuators B Chem.* **2017**, *247*, 329–335.10.1016/j.snb.2017.03.058. [CrossRef]
10. Rück, T.; Bierl, R.; Matysik, F.M. Low-cost photoacoustic NO2 trace gas monitoring at the pptV-level. *Sens. Actuators A Phys.* **2017**, *263*, 501–509.10.1016/j.sna.2017.06.036. [CrossRef]
11. Kosterev, A.A.; Bakhirkin, Y.A.; Curl, R.F.; Tittel, F.K. Quartz-enhanced photoacoustic spectroscopy. *Opt. Lett.* **2002**, *27*, 1902–1904.10.1364/OL.27.001902. [CrossRef]

12. Yi, H.; Liu, K.; Chen, W.; Tan, T.; Wang, L.; Gao, X. Application of a broadband blue laser diode to trace NO2 detection using off-beam quartz-enhanced photoacoustic spectroscopy. *Opt. Lett.* **2011**, *36*, 481–483.10.1364/OL.36.000481. [CrossRef] [PubMed]
13. Zheng, H.; Dong, L.; Yin, X.; Liu, X.; Wu, H.; Zhang, L.; Ma, W.; Yin, W.; Jia, S. Ppb-level QEPAS NO2 sensor by use of electrical modulation cancellation method with a high power blue LED. *Sens. Actuators B Chem.* **2015**, *208*, 173–179.10.1016/j.snb.2014.11.015. [CrossRef]
14. Rück, T.; Bierl, R.; Matysik, F.M. NO2 trace gas monitoring in air using off-beam quartz enhanced photoacoustic spectroscopy (QEPAS) and interference studies towards CO2, H2O and acoustic noise. *Sens. Actuators B Chem.* **2018**, *255*, 2462–2471.10.1016/j.snb.2017.09.039. [CrossRef]
15. Campillo, A.J.; Petuchowski, S.J.; Davis, C.C.; Lin, H.B. Fabry-perot photothermal trace detection. *Appl. Phys. Lett.* **1982**, *41*, 327–329.10.1063/1.93524. [CrossRef]
16. Waclawek, J.P.; Bauer, V.C.; Moser, H.; Lendl, B. 2f-wavelength modulation Fabry-Perot photothermal interferometry. *Opt. Express* **2016**, *24*, 28958–28967.10.1364/OE.24.028958. [CrossRef]
17. Waclawek, J.P.; Kristament, C.; Moser, H.; Lendl, B. Balanced-detection interferometric cavity-assisted photothermal spectroscopy. *Opt. Express* **2019**, *27*, 12183–12195.10.1364/OE.27.012183. [CrossRef]
18. Yang, F.; Jin, W.; Lin, Y.; Wang, C.; Lut, H.; Tan, Y. Hollow-core microstructured optical fiber gas sensors. *J. Lightwave Technol.* **2016**, *35*, 3413–3424. [CrossRef]
19. Krzempek, K. A Review of Photothermal Detection Techniques for Gas Sensing Applications. *Appl. Sci.* **2019**, *9*, 2826.10.3390/app9142826. [CrossRef]
20. Wynne, R.M.; Barabadi, B.; Creedon, K.J.; Ortega, A. Sub-Minute Response Time of a Hollow-Core Photonic Bandgap Fiber Gas Sensor. *J. Lightwave Technol.* **2009**, *27*, 1590–1596.10.1109/JLT.2009.2019258. [CrossRef]
21. Hoo, Y.L.; Liu, S.; Ho, H.L.; Jin, W. Fast response microstructured optical fiber methane sensor with multiple side-openings. *IEEE Photonics Technol. Lett.* **2010**, *22*, 296–298.10.1109/LPT.2009.2039016. [CrossRef]
22. Davis, C.C.; Petuchowski, S.J. Phase fluctuation optical heterodyne spectroscopy of gases. *Appl. Opt.* **1981**, *20*, 2539–2554.10.1364/AO.20.002539. [CrossRef] [PubMed]
23. Hecht, E. *Optics, Global Edition*, 5th ed.; Pearson: London, UK, 2017.
24. Preisser, S.; Rohringer, W.; Liu, M.; Kollmann, C.; Zotter, S.; Fischer, B.; Drexler, W. All-optical highly sensitive akinetic sensor for ultrasound detection and photoacoustic imaging. *Biomed. Opt. Express* **2016**, *7*, 4171–4186.10.1364/BOE.7.004171. [CrossRef] [PubMed]
25. Fischer, B.; Wintner, E. Sound Recording by Laser Interferometry. In Proceedings of the Conference on Lasers and Electro-Optics/International Quantum Electronics Conference, Baltimore, MD, USA, 31 May–5 June 2009; OSA: Washington, DC, USA, 2009; p. JWA64.10.1364/CLEO.2009.JWA64. [CrossRef]
26. Roehl, C.M.; Orlando, J.J.; Tyndall, G.S.; Shetter, R.E.; Vazquez, G.J.; Cantrell, C.A.; Calvert, J.G. Temperature Dependence of the Quantum Yields for the Photolysis of NO2 Near the Dissociation Limit. *J. Phys. Chem.* **1994**, *98*, 7837–7843.10.1021/j100083a015. [CrossRef]
27. Breitegger, P.; Bergmann, A. A Precise Gas Dilutor Based on Binary Weighted Critical Flows to Create NO2 Concentrations. *Proceedings* **2018**, *2*, 998.10.3390/proceedings2130998. [CrossRef]
28. *Mil-STD-810H: Department of Defense Test Method Standard for Environmental Engineering Considerations and Laboratory Tests*; US Department of Defense (DoD): Washington, DC, USA, 2019.
29. Herault, J.; Pétrélis, F.; Fauve, S. $1/f^{\alpha}$ Low Frequency Fluctuations in Turbulent Flows. *J. Stat. Phys.* **2015**, *161*, 1379–1389.10.1007/s10955-015-1408-5. [CrossRef]
30. Vandaele, A.; Hermans, C.; Simon, P.; Carleer, M.; Colin, R.; Fally, S.; Mérienne, M.; Jenouvrier, A.; Coquart, B. Measurements of the NO2 absorption cross-section from 42,000 cm^{-1} to 10,000 cm^{-1} (238–1000 nm) at 220 K and 294 K. *J. Quant. Spectrosc. Radiat. Transf.* **1998**, *59*, 171–184.10.1016/S0022-4073(97)00168-4. [CrossRef]

D.4 Paper 4

Towards Low-Cost QEPAS Sensors for Nitrogen Dioxide Detection

P. Breitegger[a,*], B. Schweighofer[b], H. Wegleiter[b], M. Knoll[a], B. Lang[a], A. Bergmann[a]

[a] *Institute of Electronic Sensor Systems, Graz University of Technology, 8010 Graz, Austria*
[b] *Institute of Electrical Measurement and Measurement Signal Processing, Graz University of Technology, 8010 Graz, Austria*

Abstract

Increasing awareness of the adverse health effects of air pollution leads to a demand of low-cost sensors for the measurement of pollutants such as NO_2. However, commercially available low-cost sensors lack accuracy and long-term stability, and suffer from cross-sensitivity to other gases. These drawbacks can be overcome by the method of quartz-enhanced photoacoustic spectroscopy (QEPAS). In QEPAS modulated light is absorbed by the NO_2 molecules, which results in the production of a sound wave. The sound wave is detected by resonance of a quartz tuning fork, which results in a measurable electric signal. Due to the small size of the tuning forks, the gas sensing element can be smaller than $1\,\mathrm{cm}^3$. We present the first bare fork QEPAS setup for the ppb-level detection of NO_2, which is ideally suited for environmental trace gas detection without the need of using micro-resonators. Micro-resonators are commonly used to amplify photoacoustic signals. However, micro-resonators have different dependencies on environmental conditions than tuning forks, which makes them difficult to operate in changing conditions. In contrast, our bare fork QEPAS setup is more robust and easily adopted by the use of a low-cost temperature and humidity sensor. By using acoustic filters the integration time could be increased to offer higher sensitivity at a continuous flow rate of $200\,\mathrm{std\,cm^3\,min^{-1}}$. The 1σ noise equivalent concentration is determined to 21 ppb NO_2 in synthetic air for 120 s measurement time, allowing detection which satisfies international health and safety standards thresholds.

Keywords: bare fork quartz-enhanced photoacoustic spectroscopy (QEPAS); acoustic filters; quartz tuning fork; NO_2 detection; environmental conditions; drift stability

---

1. Introduction

Despite adverse health effects, premature deaths and high costs of air pollution, citizens even in the EU are still exposed to pollutant concentrations exceeding the EU and WHO reference concentrations [1]. Among the pollutants of highest interest is nitrogen dioxide (NO_2). WHO recommends an hourly mean of $200\,\mu\mathrm{g\,m^{-3}}$ (106.4 ppb) and an annual mean of $40\,\mu\mathrm{g\,m^{-3}}$ (21.3 ppb) not to be exceeded [2].

At present, air pollution monitoring is carried out at low spatial resolution due to high costs of highly accurate measurement equipment [3]. To achieve higher spatial resolution, a denser sensor network of low-cost sensors is required. The detection of NO_2 in sensor networks is usually done by electrochemical-based sensors. These sensors are low-cost but lack long-term stability and suffer from cross sensitivity to other gases [4]. Therefore, our approach for sensing NO_2 is based on quartz-enhanced photoacoustic spectroscopy (QEPAS) [5] to overcome the aforementioned drawbacks.

Photoacoustic spectroscopy (PAS) uses the effect of sound generation at frequency f by modulating a light source at the same frequency. When the wavelength of the light source is chosen such that it matches an absorption line of the analyte, which does not interfere with other analytes in the gas mixture, PAS delivers a sound signal that is directly proportional to the analyte concentration [6]. By using acoustic resonators the signal is further amplified. Recently, a photoacoustic (PA) setup for NO_2 detection has been validated to sense environmental NO_2

---

[*] Corresponding author

concentrations with good agreement to an environmental monitoring station [7]. However, conventional PAS setups have relatively large footprints because the detection bandwidth of available microphones is limited to several kHz, which further leads to acoustic resonators in the cm range. For example, the size of the 1.75 kHz PA resonator in Yin et al. [7] was approximately 120 mm × 40 mm × 40 mm. However, sensor sizes of approximately 50 mm × 50 mm × 30 mm [8] are favored for environmental sensors, as size usually scales with cost.

In contrast to conventional PAS, QEPAS applies piezoelectric quartz tuning forks (QTFs) as acoustic transducers. The transducers usually have resonance frequencies around 32.768 kHz which correspond to acoustic wavelengths of approximately 10.5 mm with a typical length of the QTF's prongs being 3.8 mm. In addition, since QTFs are mechanical resonators, they have quality (Q) factors greater than 8000 which provides excellent amplification. In contrast, the Q factor of the setup by Yin et al. [7] is 25. As piezoelectric QTFs are mass produced for the use as clocks in quartz watches they are available for prices in the cent range. Additionally, QEPAS setups offer high background noise immunity, e.g. QEPAS yielded an improvement in noise immunity by a factor of 46 compared to a conventional PAS setup in traffic noise simulations [9].

For the detection of NO_2, a number of low-cost light sources in the visible (VIS) range of light are available. Due to the absorption spectrum of NO_2, which has a broad absorption spectrum in the visible range, however without pronounced absorption peaks, modulation of the light source has always be done by amplitude modulation. QEPAS setups for NO_2 detection usually rely on light sources with a peak emission around 450 nm. At this wavelength, NO_2 yields high absorption and photodissociation of NO_2 is not promoted [10]. Further, this wavelength yields negligible cross-interference to other gases (cf. Figure 1). To overcome possible cross-interference by the broad absorption range of soot (cf. [11]) a filter can be placed at the sampling inlet.

To date QEPAS sensors for NO_2 have relied on off-beam (ob) configuration in which the laser is directed through a micro-resonator, with the first longitudinal mode sharing the same resonance frequency as the QTF. A small slit in the middle of the micro-resonator is directed between the QTF's prongs, which allows the QTF to sense the amplified acoustic wave. This configuration has two advantages: First, the acoustic signal is additionally amplified by a factor of 15 as compared to bare QTF setups [16]. Second, the beam quality can be worse than for bare QTF setups, due to the larger diameter of the micro-resonator (e.g. 1.6 mm in Rück et al. [9]) as compared to the distance between the prongs of commercial QTFs (approximately 300 µm in this publication). However, ob-QEPAS has one disadvantage, especially relevant for ambient measurements: The micro-resonator and QTF are affected differently by environmental conditions such as temperature, pressure and gas composition. Therefore, the resonance frequency of the two resonators shift differently with changing conditions, resulting in huge variations of the combined amplification. This detuning effect was seen by Rück et al. [9], where the sensor signal rose by 35 % when increasing relative humidity from 0 to 80 %.

A limit of detection of at least 106.4 ppb NO_2 is required to detect the exceedance of hourly mean thresholds, which was achieved by the previous QEPAS setups. Detection limits of 600 ppt NO_2 [9], 1.3 ppb NO_2 [17], and 4.4 ppb NO_2 [18] are reported for ob-QEPAS configurations.

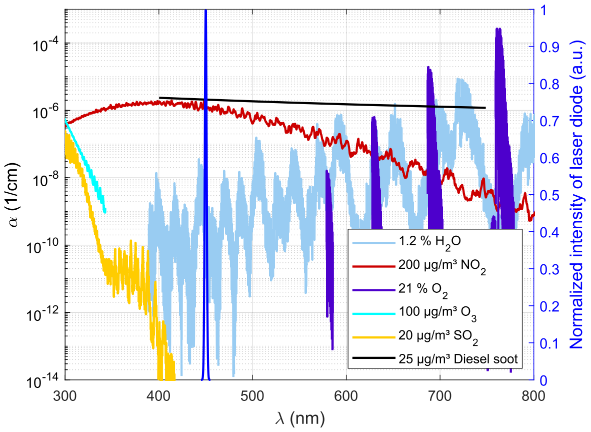

Figure 1: Absorption of different environmental gases between 300 nm and 800 nm according to the HITRAN database [12, 13] and absorption of diesel soot between 400 nm and 750 nm [14]. Concentrations reflect the current WHO recommended limits (NO_2: 1-hour mean, O_3: 8-hour mean, SO_2: 24-hour mean, Diesel soot ($PM_{2.5}$): 24-hour mean) [15]. Laser emission spectrum is shown in blue.

However, ob- configurations suffer from their high dependency on environmental conditions. Therefore, we employ bare fork (bf) QEPAS for detection of NO_2 to demonstrate limits of detection appropriate for environmental monitoring. In this configuration, the Q factor is insensitive to temperature, pressure and changes of gas composition when compared with off-beam methods, thereby providing opportunity for corrections of the resonance frequency. This will be highlighted by discussing models for the tuning fork and micro-resonators. The integration time could be increased to previously unattained values by the use of acoustic filters, which also reduce gas flow noise.

2. Material and methods

A cut through the cell and focusing optics is shown in Figure 2. A laser diode (OSRAM: PL 450B) is used as excitation light source. The laser diode mount passively cooles the laser diode. The collimation and focusing optics is mounted in a cage system. The laser diode is collimated by an aspheric lens (Thorlabs: A220TM-A) and stray-light is removed from the collimated beam with an iris diaphragm, which is set to approximately 900 µm. The beam is focused into the gas cell and between the prongs of the QTF (Fox Electronics: NC38LF) with a $f = 30\,\mathrm{mm}$ focusing lens. To remove stray-light more effectively, a 3D printed aperture of approximately 500 µm is placed at the front of the cell. The focus of the laser beam, which is of 116 µm width (cf. Appendix A), is adjusted to pass the prongs of the QTF approximately 0.7 mm from the top of the prongs for a strong signal (cf. [5]). The 3D printed gas cell has a sample volume of dimensions $20.6\,\mathrm{mm} \times 16\,\mathrm{mm} \times 9.7\,\mathrm{mm}$, which can easily be miniaturized to lower values. The cell, which also carries the two stage amplifier, is covered by aluminum tape, which is grounded for electronic shielding. An unshielded version of the cell resulted in signal fluctuations corresponding to ppm concentrations of NO_2. All 3D printed parts are printed with a stereolithographic 3D printer (FORMLABS: Form 2) with 25 µm resolution.

The experimental setup is shown in Figure 3. Gas mixtures are passed to the QEPAS cell at a flow rate of 200 std $\mathrm{cm}^3\,\mathrm{min}^{-1}$, controlled by a mass flow controller (MFC; Vögtlin: Model GSC-B). Acoustic filters at the in- and outlet of the cell improve noise and drift characteristics (cf. Section 4.2).

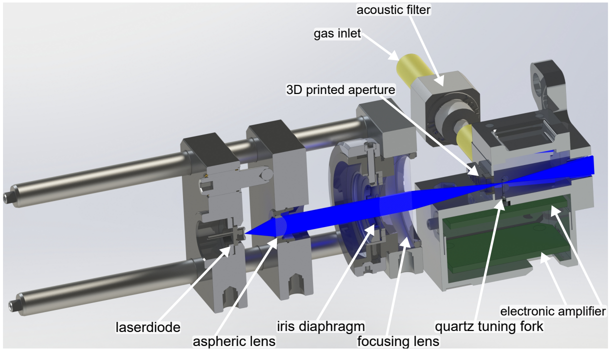

Figure 2: Cut through the optical setup and the 3D-printed cell. Laser beam is shown in blue. The gas outlet is perpendicular to the inlet. Description of the elements can be found in the text. The distance from the laser diode mount to the back of the cell is ≈ 10 cm.

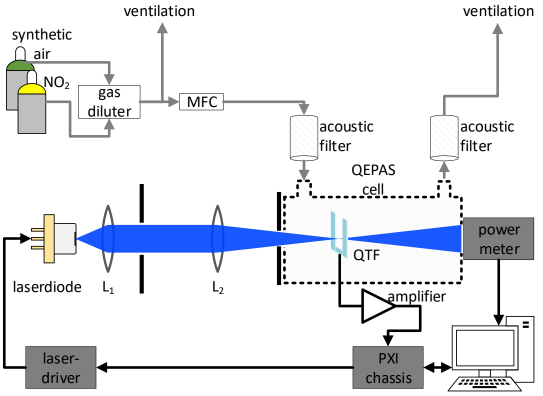

Figure 3: Schematic of the experimental setup for characterizing the response to NO_2. L_1, aspheric lens; L_2, focusing lens; QTF, quartz tuning fork.

The signal from the QTF is amplified with a custom two-stage amplifier. The signal is acquired with a data acquisition (DAQ) card (National Instruments: Model PXI-6281) at 250 kSps and post-processed on a personal computer (PC). The same chassis carrying the PXI-6281 also houses a function generator (National Instruments: Model PXI-5402). The function generator provides the square wave modulation signal (50 % duty cycle) for the laser driver (Thorlabs: ITC4001). The laser modulation results in an average optical power of approximately 46.9 mW (±3% at 450 nm), measured by means of a power meter (Thorlabs: Model S120C). This is slightly higher than the expected half nominal cw optical power of 40 mW. The amplified QTF-signal is filtered with a lock-in amplifier, which is realized as a custom LabVIEW application on a PC. The integration time is set to 1 s. Due to the limited buffer size of the DAQ card, data acquisition and modulation is stopped and restarted after each measurement to obtain the same phase. Since the QTF is excited from zero at each measurement, the build up phase and release time, which result from the high Q factor of the resonator have to be removed from the measurement. The timescale can be calculated as $\tau = Q/\pi f_0 \approx 100\,\mathrm{ms}$. To reduce uncertainties in the measurement, the first 0.5 s of the measurement are removed and therefore, the measurement time is extended by 0.5 s compared to the integration time.

All measurements were performed at atmospheric pressure. Gas mixtures were produced with a temperature stabilized custom gas diluter based on binary weighted critical orifices [19], which offers low uncertainties at high dilution ratios. The NO_2 gas cylinder contains a mixture of NO_2 and synthetic air (Messer Austria GmbH: 19.2 ppm NO_2). This mixture was further diluted with synthetic air (Messer Austria GmbH: Synthetic Air, Scientific).

3. Influence of gas composition on the photoacoustic signal

Effects of different environmental conditions must be considered during calibration of QEPAS sensors for ambient measurements. Changes in environmental conditions affect the resonance frequency and the Q-factor of a QTF. E.g., for $Q = 8000$, a resonance frequency shift of 1 Hz results in a 10 % signal drop. As will be shown, temperature has the biggest influence on the QTF by affecting its resonance frequency. Expected pressure changes in environmental sensing only have a minor effect on resonance frequency and Q-factor. Humidity promotes a faster relaxation of the excited states, resulting in a humidity-enhanced signal [6]. An excitation frequency adjustment based on a temperature sensor and a signal adjustment based on a humidity sensor can be implemented in a bf-QEPAS setup.

In contrast, ob-QEPAS setups strongly depend on temperature, humidity and the speed of sound of the gas mixture, which also changes with humidity [9, 20]. As the resonance frequencies of the micro-resonator and QTF shift differently with changing conditions, the combined Q-factor varies greatly and cannot easily be described, making ob-QEPAS less suitable for low-cost environmental sensors than bf-QEPAS. This is summarized in Table 1 and shown in the next sections, e.g. by considering typically expected variations of temperature and pressure in environmental sensing.

Table 1: Summary of the influences of temperature (T), pressure (p), and humidity (H) of the resonance frequency f_0, the quality factor Q and the photoacoustic signal S. The sign before the slash defines how much the quantity is affected (+ ... not, o ... little, - ... much), the second defines how easy a correction can be done (+ ... easy, o ... with effort, - ... not possible), e.g. for bf-QEPAS, the temperature influence on the resonance frequency f_0 is little (o) and can easily be corrected (+).

	bare fork			**off-beam**		
	Q	f_0	S	Q	f_0	S
T	+/n.a.	o/+	o/+	-/o	-/o	o/+
p	o/+	o/+	+/n.a.	o/+	o/+	+/n.a.
H	+/n.a.	+/n.a.	-/+	-/-	-/-	-/-

3.1. Temperature

To investigate the temperature dependence of a QTF's resonance frequency, heated gas was applied to the bf-QEPAS sensor. The temperature was measured by means of a temperature sensor (Sensirion AG: SHT31), which was mounted into the cap of the bf-QEPAS sensor. After the temperature in the cell remained at a stable value, a series of eight sweeps was performed with synthetic air and 19.2 ppm NO_2, respectively. The resonance frequencies were determined by fits to these sweeps and are depicted in Figure 4. The temperature dependence is evident and justifies that the resonance frequency should be determined after a change in temperature is detected. The QTF used for this work is specified for operation between $-20\,^\circ\mathrm{C}$ and $60\,^\circ\mathrm{C}$ [21], but temperatures below and above this range are also possible for quartz [22]. Since the noise in QEPAS is proportional to $\sqrt{T}$ (cf. Equation (5)), the sensitivity is assumed to improve with decreasing temperature.

Figure 5 displays the background corrected signal with NO_2. The signal decreases to 14 % of the original signal if the resonance frequency is not adopted after a temperature increase of 10 °C. In

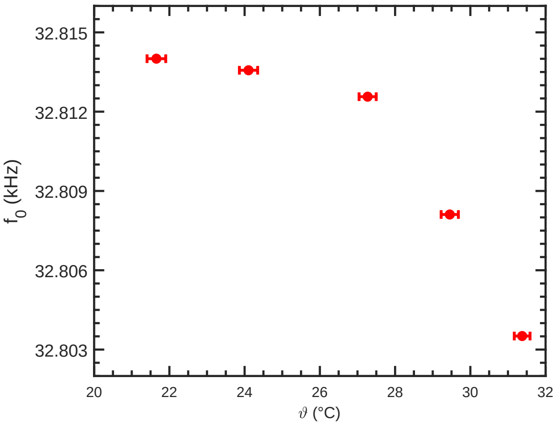

Figure 4: Temperature dependence of the resonance frequency.

contrast, by applying a resonance correction, the signal has a maximum deviation of 8 %. Deviations from 100 % are caused by the $1/c^2 \propto 1/T$ dependence of the QEPAS pressure [23], which can easily be corrected by taking into account the actual temperature of the gas. A dependence of the Q factor on temperature could not be observed.

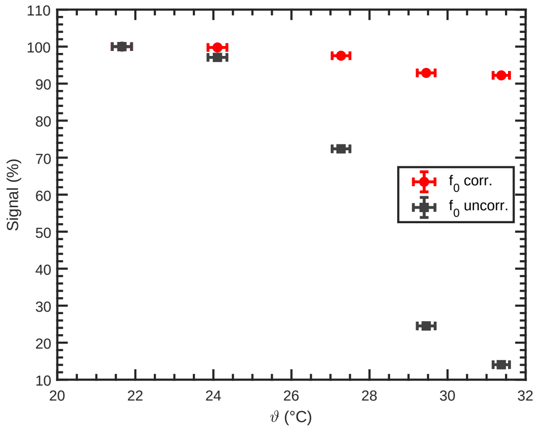

Figure 5: Measured signal with 19.2 ppm NO_2 in % of the signal measured at 21.6 °C as function of temperature. Signal with frequency adoption (red); Signal without frequency adoption (black).

However, in ob-QEPAS micro-resonators are used to acoustically amplify the PA signal. Micro-resonators are open ended acoustic resonators. The resonance frequency f_{mr} of the fundamental longitudinal oscillation is given by [9]

$$f_{mr} = \frac{c_s}{2L_{res}}, \tag{1}$$

where L_{res} is the resonator length and c_s the speed of sound. According to the ideal gas law, c_s depends on the temperature T as $\sqrt{T}$. Therefore the resonance frequency of QTF and micro-resonator shift contrary with respect to T. A temperature change from 25 °C to 35 °C increases the micro-resonator's resonance frequency by roughly 550 Hz, which shifts the resonance curve with respect to that of the QTF, where the resonance frequency would decrease by roughly 10 Hz, resulting in a tremendous change of the combined Q-factor and thus the signal strength. E.g., a doubling of the combined Q-factor of an ob-QEPAS setup by a temperature increase from approximately 315 K to 345 K is reported by Köhring et al. [20] - an issue which is avoided in the present bf-QEPAS setup.

3.2. Pressure

A pressure change influences the resonance frequency and the Q-factor of the QTF. Kosterev et al. [24] described the dependence of the QTF's resonance frequency on the pressure, $f_{res}(p)$, by

$$f_{res}(p) = f_{vac} - \frac{df_{res}}{dp}p, \tag{2}$$

where f_{vac} is the resonance frequency in vacuum and $\frac{df_{res}}{dp} = 7.2 \times 10^{-3}\,\mathrm{Hz\,mbar^{-1}}$. For a pressure change from 970 mbar to 1013.25 mbar, the resonance frequency would change by 0.3 Hz, resulting in a minor signal drop of 1 % if not corrected. The pressure dependence of the Q-factor of a QTF of the same dimensions as it was used for this publication can be described in form of [24]

$$Q(p) = \frac{Q_{vac}}{1 + Q_{vac}ap^b}, \tag{3}$$

where $a = 2.8 \times 10^{-6}$ and $b = 0.47$. For the same pressure change as above, Q would decrease by 2 %, resulting in a signal drop of 2 %. However, as both expressions are known, corrections can easily be implemented in bf-QEPAS.

To study the dependence of a micro-resonator's resonance frequency on pressure, the speed of sound in Equation (1) can be rewritten by using the ideal gas law to $c_s = \sqrt{\gamma\frac{p}{\rho}}$, with p the pressure, ρ the density and γ the adiabatic index. As p and ρ are directly proportional via the ideal gas law, the resonance frequency of the micro-resonator is independent of the pressure.

3.3. Humidity

The dependence η of the photoacoustic signal on the relaxation time τ and the modulation frequency f_0 from the exited states can be described by Equation 4 [6]:

$$\eta = \frac{1}{\sqrt{1 + (2\pi f_0 \tau)^2}}. \tag{4}$$

For NO_2, $\tau < 4\,\mu s$ is reported [25], which already affects the signal strength for the modulation frequency of $f_0 \approx 32.8\,kHz$. Adding water vapor has been shown to speeding up the delayed molecular relaxation also for NO_2 and modulation frequencies of 1.75 kHz [7].

The effect of humidity on the photoacoustic signal is analyzed by applying different mixtures of NO_2 and humidified air to the QEPAS cell. In order to prevent a reaction between NO_2 and H_2O, NO_2 was added after the humidifier. The concentrations were adjusted with two MFCs (Vgtlin: Model GSC-B), which were calibrated by bubble flow meters (Gilian: Gilibrator 2). Relative humidity was measured by means of a humidity sensor (Sensirion: SHT31). Relative humidity ranged from 3.3 % RH (water concentration of 0.08 %) to 64 % RH (water concentration of 1.52 %). The temperature in the cell was 24 °C. Sensor signals are normalized by the corresponding NO_2 concentrations and referenced to the 3.3 % RH humidity measurement (19.2 ppm NO_2 from the gas cylinder). The corresponding plot is depicted in Figure 6, where a signal enhancement, due to added humidity can clearly be seen. An improvement of uncertainty at high humidities could be achieved by using MFCs calibrated for lower flow rates.

The increase might be approximated by $S_N = a \cdot x + b$, where S_N is the normalized QEPAS signal, x the relative humidity concentration in percent, and $a = 0.98$ and $b = 0.005$ are fit parameters. This signal enhancement is likely to be caused by a drop in relaxation time of the excited state as seen for other molecules such as CO_2, HCN and CH_4 for added humidity [26, 27, 28].

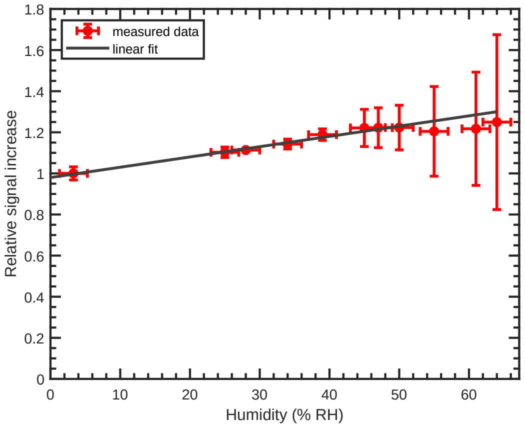

Figure 6: Relative QEPAS signal with respect to the humidity in the reference gas cylinder as a function of relative humidity (red) and linear fit (black). Errorbars at high humidities result from the high uncertainty at low flow rates of the MFCs used.

Finally, no changes of resonance frequency or quality factor were found. Thus, the sensor reading of the bf-QEPAS sensor can easily be corrected by the above equation and the use of a humidity sensor reading. In contrast, signal enhancement due to humidity in an ob-QEPAS setup leads to a detuning between QTF and micro resonator [9]. This is caused by the fact that the resonance frequency of a micro resonator is depending on the speed of sound (cf. Equation (1)), which depends on the adiabatic index as $\sqrt{\gamma}$. In contrast, the resonance frequency of the QTF is independent of the speed of sound. Thus, the combination of the two effects does not allow for straight-forward signal corrections in ob-QEPAS.

4. Noise analysis

To investigate the individual noise contributions and possible improvements of the setup, the fundamental noise of the QTF is investigated. Then, Allan deviation is calculated to investigate sources of noise and drift.

4.1. Thermal noise and amplification topology

The noise in QEPAS is fundamentally limited by the thermal noise of the QTF. To investigate the thermal noise, the electronic amplification circuit must be characterized first. In this work, the QTF signal was amplified by a custom circuit consisting of a transimpedance amplifier (TIA) and a non-inverting amplifier with an amplification of 270. The TIA topology (Figure 7) uses a *LTC6240HV* low noise operational amplifier with a feedback resistor of $R_f = 6.8\,\mathrm{M\Omega}$ with a 0.3 pF capacitor in parallel for stability reasons.

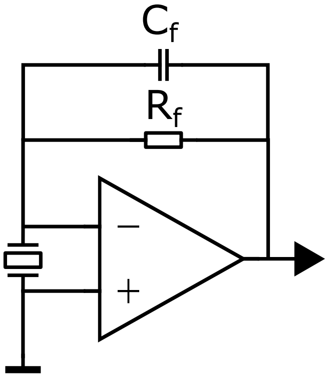

Figure 7: Schematic drawing of the TIA topology used for this work.

As discussed by Starecki and Wieczorek [29], a TIA behaves like a low-pass at high frequencies. For the given configuration, stray and other capacitances C_s are estimated to be 1.5 pF. This results in a cut-off frequency of $f_{co} = \frac{1}{2\pi R_f C_s} \approx 16\,\mathrm{kHz}$. The corresponding amplification at the resonance frequency is therefore roughly 43 % of its value at low frequencies. Since noise is attenuated by the same factor, the signal-to-noise ratio remains unchanged but it needs to be considered by performing the consecutive calculations with a reduced feedback resistor $R'_f = R_f \cdot 0.43 \approx 2.9\,\mathrm{M\Omega}$. This behaviour is important and usually neglected for estimating the thermal noise of the QTF. The thermal noise of the QTF also depends on the resistance of its Butterworth-Van Dyke equivalence circuit [30] as shown in Figure 8. Here, R is the resistance, L is the inductance, C_m is the motional capacitance, and C_p is the parasitic capacitance.

The thermal noise in the TIA topology, $\sqrt{< V_N^2 >}$, is given by [31]

$$\sqrt{< V_N^2 >} = R'_f \sqrt{\frac{\Delta f 4 k_B T}{R}}. \quad (5)$$

In this equation, R'_f is the reduced feedback resistor, Δf is the detection bandwidth, k_B is the Boltzmann constant, and T is the temperature. It is therefore crucial to determine R to evaluate the fundamental noise floor.

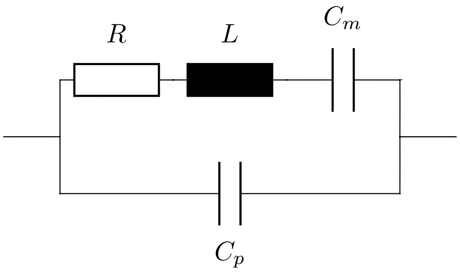

Figure 8: Butterworth-Van Dyke equivalence circuit of a QTF.

In this work, R was determined by thermally exciting the QTF with the laser and fitting the real- and imaginary part of the response signal to the admittance as described by the electric equivalence circuit (Appendix B). The resistance R was determined to 85.7 kΩ, resulting in a thermal noise after the TIA of 1.29 µV.

The actual noise of the circuit was measured by investigating the average noise of the QTF signal at the resonance frequency with the laser switched off (Figure B.14). There, the noise after the TIA equates to 1.48 µV. Considering the manufacturing uncertainties of the electric components, the noise of the operational amplifier, as well as the estimation of the stray capacitances, the electronic noise of the circuit is close to its optimum value, leaving little space for improvement of the TIA.

4.2. Contribution of noise sources

Allan deviation was calculated to investigate sources of noise and drift for different configurations. In Figure 9, Allan deviation is plotted as a function of the measurement time. The integration of the acquired data is simply performed by averaging the values over the measurement period. One data measurement cycle for 1 s averaging time is 1.5 s, due to the previously mentioned 0.5 s startup time. In the Allan deviation plots, the measurement cycles (1.5 s) are simply strung together to give the measurement time. Consequently, using a certain averaging time is supposed to yield even a lower noise than the corresponding Allan deviation in Figure 9 suggests. To give an example, an averaging time of 10.5 s corresponds to the Allan deviation of 15 s in Figure 9. This is due to the fact that the 0.5 s start up of the QFT is required only once for a specific averaging time.

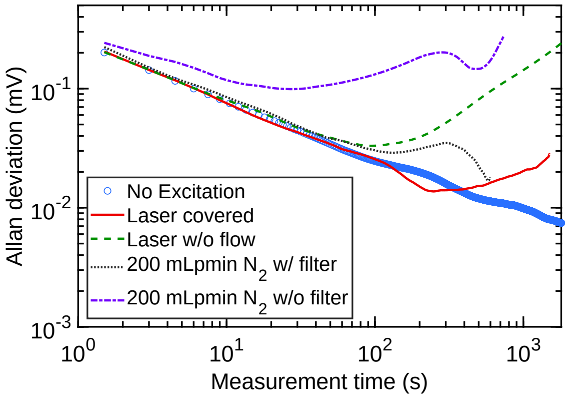

Figure 9: Allan deviation of the photoacoustic signal at different configurations as a function of the measurement time. Allan deviation was calculated with MATLAB[2].

The fundamental deviation due to thermal noise (blue) is 201 µV for 1 s averaging time (1.5 s measurement time) and continuously decreasing with increasing averaging time without a drift being visible within the highest averaging time.
Neither switching the covered laser on (red), nor uncovering the laser (green) significantly increases the deviation. However, drift occurs after 225 s measurement time for the covered laser and decreases to 120 s for the uncovered laser due to a drift of the laser power (cf. Figure C.15).
Flow noise, due to the gas flow (purple) would increase the deviation to 242 µV for 1 s averaging time and the maximum averaging time would be limited to 24 s due to drift. In contrast, due to the acoustic filters (black) the 1 s deviation is reduced to 223 µV and drift is improved to the level determined by the laser drift (120 s measurement time), yielding a value of 29 µV for the corresponding averaging time of 80 s. This allows for much longer averaging times as compared to other QEPAS setups for NO_2 (20 s [18] and 10 s [9]), which allows to achieve low limits of detection by increasing the integration time.

4.2.1. Acoustic filter design

Due to its high resonance frequency and quadrupole characteristics, QEPAS is little susceptible to external noise [9]. However, to additionally suppress flow noise, noise from outside the cell, and diminish drift, a two stage acoustic filter was designed and 3D printed. Two two-stage filters are used in the setup, one at the inlet and one at the outlet.
The two filters are expansion chamber mufflers of length ¼ λ_0 (2.6 mm) and ¾ λ_0 (7.8 mm), where $\lambda_0 = \frac{c_0}{f_0}$ is the wavelength corresponding to the resonance frequency f_0 of the QTF. Diameters are chosen such that only plane waves can propagate (6 mm and 10 mm, respectively). The combined transmission loss, calculated with the help of COMSOL Multiphysics, is plotted in Figure 10. As can be seen, the transmission loss is better than 38 dB in the range of the resonance frequency.

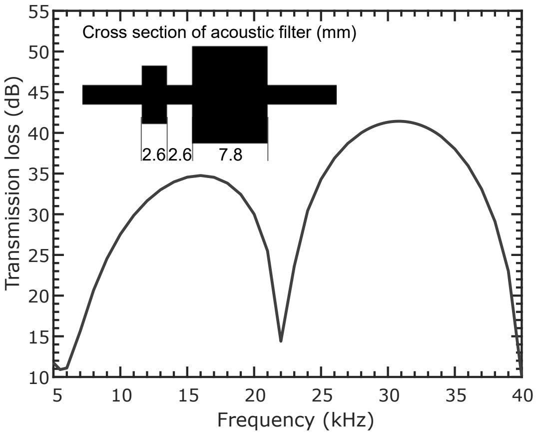

Figure 10: Transmission loss of the two stage acoustic filter. Inset shows the cross section and dimensions of the acoustic filter.

Further, an eigenfrequency analysis and a frequency sweep over the expected modulation frequency range from 32 kHz to 33.6 kHz was carried out to design the cell such that no unwanted constructive or destructive interferences appear within the cell.

5. Linearity, stability and limit of detection

Figure 11 shows the QEPAS signal as a function of the NO_2 concentration which was varied between

---

[2] Author : E. Ogier, Version : 1.0, Release : 28th mar. 2016, MATLAB, calculation: classical type, Title: AVAR

87 ppb and 19.2 ppm. Each datapoint was averaged for approximately 80 values. All signals are background corrected with respect to their phase. The linear regression for the photoacoustic signal S as a function of concentration c equates to $S = b \cdot c + a$, where the slope $b = (1.39 \pm 0.02)\,\mu\mathrm{V\,ppb}^{-1}$ and intercept $a = (26 \pm 95)\,\mu\mathrm{V}$. The coefficient of determination for the fit is $R^2 = 0.999$.

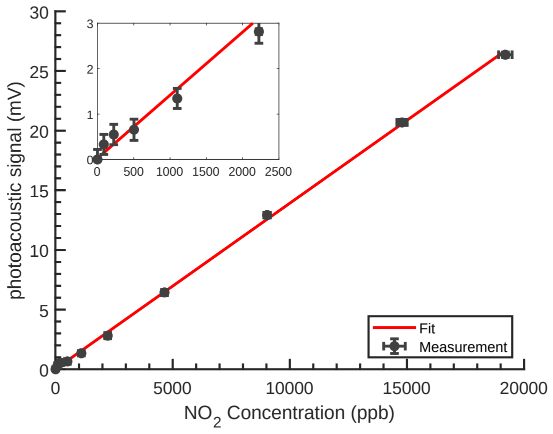

Figure 11: Linear fit (red) of the background corrected photoacoustic signal as a function of the NO_2 concentration. Errorbars of the PA signals are the standard deviation of the recorded values. Errorbars of the concentrations show the standard deviation calculated with GUM Workbench. The linear curve fit was conducted in MATLAB[4].

By using the standard deviation of the noise with acoustic filters from the previous chapter, the noise equivalent concentration (NEC) for $1\,\sigma$ and 1 s integration time is determined to 160 ppb NO_2 in synthetic air. This is a factor of 7.7 higher than in Yi et al. [18], when normalizing their value to synthetic air as described in the previous chapter. For the longest possible measurement time, according to the noise analysis, we achieve a normalized NEC of 21 ppb for 120 s which is a feasible value for environmental trace gas detection, since the typical averaging time in environmental monitoring is 1 h [3].

6. Discussion

Compared to off-beam configurations, the present system is more robust to changes of environmental conditions such as humidity and temperature. Temperature changes can be taken into account by adjusting the laser modulation frequency and a simple model. Corrections for humidity influences are possible by using a simplified model, taking into account only a humidity sensor reading. Hence, with the simple bf-QEPAS setup and simple models, the overall measurement uncertainty can be reduced significantly making it suitable for environmental trace gas measurements.

In contrast to ob-QEPAS, where production tolerances of micro-resonators would make calibration in a wide parameter space, spanned by temperature, humidity and NO_2 concentration necessary, simply one linearity curve is sufficient in bf-QEPAS. The dependence of ob-QEPAS on temperature is difficult to compensate due to the different dependencies of micro-resonator and the QTF. A rising temperature leads to a smaller resonance frequency of the micro-resonator, while the resonance frequency of the QTF shows a parabolic behaviour with respect to the temperature. Thus, for ob-QEPAS a sample gas conditioning system is necessary to overcome these influences at the cost of size, power consumption and price, which are undesirable in low-cost sensing.

Due to its simple setup, bf-QEPAS has the potential to be mass-produced. In an automated process, the optimal focus point between the prongs can be found with a power meter or a beam profiler positioned at the back of the cell in bf-QEPAS. In contrast, ob-QEPAS relies on positioning of a collimated beam to the microresonator, but also on precise positioning of the micro-resonator to the QTF. It is expected that with little engineering effort, a miniaturization of a bf-configuration to a size of approximately 50 mm × 50 mm × 30 mm seems feasible.

7. Conclusion and outlook

The presented QEPAS setup is able to reach a 1σ detection limit of 21 ppb NO_2 in synthetic air for 120 s measurement time.

By using the Butterworth-Van Dyke equivalent model, the noise of the preamplifier was determined to be close to the fundamental thermal noise level. The noise level due to acoustic noise could be reduced by using acoustic filters. The use of such acoustic filters is also expected to be advantageous

---

[4] Author: Travis Wiens, Version: 1.0.0.0, Release: 2010, Title: Linear Regression with Errors in X and Y

for environmental trace gas sensing, where traffic noise is likely to have a higher contribution than the flow noise. Further, the use of acoustic filters minimizes drift, which allows for measurement times up to 120 s, thereby enabling low detection limits at relatively low laser powers.

In future, the lock-in amplifier as well as the laser driver will be replaced by a low-cost, custom developed electronic solution built around a micro-controller to have a complete low-cost NO_2 sensor platform. By overcoming the limitation of limited continuous measurements of the present setup, the averaging time can be increased to 120 s, to reach even lower limits of detection. Further, it is assumed that drift of the laser diode can be compensated in software, by monitoring the temperature, the power, or the current of the laser diode. In addition, a mechanical coupling between the optical components and the QTF is planned, to provide stability against external vibrations. To enable lower detection limits at low timescales, the laser diode could be operated in pulsed mode (cf. [32]), as pulsed operation produces a $\pi/2$ times higher photoacoustic signal [33].

Acknowledgements

The authors would like to thank Robert T. Nishida (Department of Engineering, University of Cambridge) for constructive criticism of the manuscript.

Conflicts of interest

The authors declare no conflict of interest.

References

[1] C. Guerreiro, A. González Ortiz, F. de Leeuw, V. Mar, A. Colette, Air quality in Europe 2018 report, Tech. Rep., Luxembourg, doi:10.2800/777411, 2018.

[2] World Health Organisation, Air quality guidelines for particulate matter, ozone, nitrogen dioxide and sulfur dioxide Global update 2005, WHO Press, Geneva, ISBN 92 890 2192 6, 2006.

[3] European Parliament, Council of the European Union, Directive 2008/50/EC of the European Parliament and of the Council of 21 May 2008 on ambient air quality and cleaner air for Europe, 2008.

[4] N. Castell, F. R. Dauge, P. Schneider, M. Vogt, U. Lerner, B. Fishbain, D. Broday, A. Bartonova, Can commercial low-cost sensor platforms contribute to air quality monitoring and exposure estimates?, Environment International 99 (2017) 293–302, ISSN 18736750, doi:10.1016/j.envint.2016.12.007.

[5] A. A. Kosterev, Y. A. Bakhirkin, R. F. Curl, F. K. Tittel, Quartz-enhanced photoacoustic spectroscopy, Optics Letters 27 (21) (2002) 1902, ISSN 0146-9592, doi:10.1364/OL.27.001902.

[6] Z. Bozóki, A. Pogány, G. Szabó, Photoacoustic instruments for practical applications: Present, potentials, and future challenges, Applied Spectroscopy Reviews 46 (1) (2011) 1–37, ISSN 05704928, doi:10.1080/05704928.2010.520178.

[7] X. Yin, L. Dong, H. Wu, H. Zheng, W. Ma, L. Zhang, W. Yin, S. Jia, F. K. Tittel, Sub-ppb nitrogen dioxide detection with a large linear dynamic range by use of a differential photoacoustic cell and a 3.5 W blue multimode diode laser, Sensors and Actuators, B: Chemical 247 (2017) 329–335, ISSN 09254005, doi:10.1016/j.snb.2017.03.058.

[8] Sensirion, Datasheet SPS30 Particulate Matter Sensor for Air Quality Monitoring and Control, URL `www.sensirion.com`, 2018.

[9] T. Rück, R. Bierl, F. M. Matysik, NO2 trace gas monitoring in air using off-beam quartz enhanced photoacoustic spectroscopy (QEPAS) and interference studies towards CO2, H2O and acoustic noise, Sensors and Actuators, B: Chemical 255 (2) (2018) 2462–2471, ISSN 09254005, doi:10.1016/j.snb.2017.09.039.

[10] C. M. Roehl, J. J. Orlando, G. S. Tyndall, R. E. Shetter, G. J. Vazquez, C. A. Cantrell, J. G. Calvert, Temperature Dependence of the Quantum Yields for the Photolysis of NO2 Near the Dissociation Limit, The Journal of Physical Chemistry 98 (32) (1994) 7837–7843, ISSN 0022-3654, doi:10.1021/j100083a015, URL `http://pubs.acs.org/doi/abs/10.1021/j100083a015`.

[11] P. Breitegger, M. A. Schriefl, R. T. Nishida, S. Hochgreb, A. Bergmann, Soot mass concentration sensor using quartz-enhanced photoacoustic spectroscopy, Aerosol Science and Technology (2019) 1–5ISSN 0278-6826, doi:10.1080/02786826.2019.1635677, URL `https://www.tandfonline.com/doi/full/10.1080/02786826.2019.1635677`.

[12] A. Vandaele, C. Hermans, P. Simon, M. Carleer, R. Colin, S. Fally, M. Mérienne, A. Jenouvrier, B. Coquart, Measurements of the NO2 absorption cross-section from 42,000 cm-1 to 10,000 cm-1 (238-1000 nm) at 220 K and 294 K, Journal of Quantitative Spectroscopy and Radiative Transfer 59 (3-5) (1998) 171–184, ISSN 00224073, doi:10.1016/S0022-4073(97)00168-4, URL `https://linkinghub.elsevier.com/retrieve/pii/S0022407397001684`.

[13] L. S. Rothman, I. E. Gordon, Y. Babikov, A. Barbe, D. Chris Benner, P. F. Bernath, M. Birk, L. Bizzocchi, V. Boudon, L. R. Brown, A. Campargue, K. Chance, E. A. Cohen, L. H. Coudert, V. M. Devi, B. J. Drouin, A. Fayt, J. M. Flaud, R. R. Gamache, J. J. Harrison, J. M. Hartmann, C. Hill, J. T. Hodges, D. Jacquemart, A. Jolly, J. Lamouroux, R. J. Le Roy, G. Li, D. A. Long, O. M. Lyulin, C. J. Mackie, S. T. Massie, S. Mikhailenko, H. S. Müller, O. V. Naumenko, A. V. Nikitin, J. Orphal, V. Perevalov, A. Perrin, E. R. Polovtseva, C. Richard, M. A. Smith, E. Starikova, K. Sung, S. Tashkun, J. Tennyson, G. C. Toon, V. G. Tyuterev, G. Wagner, The HITRAN2012 molecular spectroscopic database, Journal of Quantitative Spectroscopy and Radiative Transfer 130 (2013) 4–50, ISSN 00224073, doi:10.1016/

j.jqsrt.2013.07.002.

[14] M. Schnaiter, H. Horvath, O. Möhler, K. H. Naumann, H. Saathoff, O. W. Schöck, UV-VIS-NIR spectral optical properties of soot and soot-containing aerosols, Journal of Aerosol Science 34 (10) (2003) 1421–1444, ISSN 00218502, doi:10.1016/S0021-8502(03)00361-6.

[15] WHO, Evolution of WHO air quality guidelines: past, present and future, ISBN 978 92 890 5230 6, URL `http://www.euro.who.int/pubrequest%0Ahttp://www.euro.who.int/__data/assets/pdf_file/0019/331660/Evolution-air-quality.pdf`, 2017.

[16] K. Liu, J. Li, L. Wang, T. Tan, W. Zhang, X. Gao, W. Chen, F. K. Tittel, Trace gas sensor based on quartz tuning fork enhanced laser photoacoustic spectroscopy, Applied Physics B 94 (3) (2009) 527–533, ISSN 0946-2171, doi:10.1007/s00340-008-3233-x.

[17] H. Zheng, L. Dong, X. Yin, X. Liu, H. Wu, L. Zhang, W. Ma, W. Yin, S. Jia, Ppb-level QEPAS NO2 sensor by use of electrical modulation cancellation method with a high power blue LED, Sensors and Actuators, B: Chemical 208 (2) (2015) 173–179, ISSN 09254005, doi:10.1016/j.snb.2014.11.015.

[18] H. Yi, K. Liu, W. Chen, T. Tan, L. Wang, X. Gao, Application of a broadband blue laser diode to trace NO2 detection using off-beam quartz-enhanced photoacoustic spectroscopy, Optics Letters 36 (4) (2011) 481, ISSN 0146-9592, doi:10.1364/OL.36.000481.

[19] P. Breitegger, A. Bergmann, A Precise Gas Dilutor Based on Binary Weighted Critical Flows to Create NO2 Concentrations, Proceedings 2 (13) (2018) 998, ISSN 2504-3900, doi:10.3390/proceedings2130998.

[20] M. Köhring, S. Böttger, U. Willer, W. Schade, Temperature effects in tuning fork enhanced interferometric photoacoustic spectroscopy, Optics Express 21 (18) (2013) 20911, ISSN 1094-4087, doi:10.1364/OE.21.020911.

[21] Fox Electronics, Datasheet Tuning Fork Crystal, URL `https://foxonline.com/wp-content/uploads/pdfs/KT15{_}KT26{_}KT38.pdf`, 2019.

[22] Y. Saigusa, Quartz-Based Piezoelectric Materials, in: Advanced Piezoelectric Materials, Elsevier Ltd., 2 edn., ISBN 9780081021354, 197–233, doi:10.1016/b978-0-08-102135-4.00005-9, URL `http://dx.doi.org/10.1016/B978-0-08-102135-4.00005-9`, 2017.

[23] N. Petra, J. Zweck, A. A. Kosterev, S. E. Minkoff, D. Thomazy, Theoretical analysis of a quartz-enhanced photoacoustic spectroscopy sensor, Applied Physics B 94 (4) (2009) 673–680, ISSN 0946-2171, doi:10.1007/s00340-009-3379-1, URL `http://link.springer.com/10.1007/s00340-009-3379-1`.

[24] A. A. Kosterev, F. K. Tittel, D. V. Serebryakov, A. L. Malinovsky, I. V. Morozov, Applications of quartz tuning forks in spectroscopic gas sensing, Review of Scientific Instruments 76 (4) (2005) 043105, ISSN 0034-6748, doi:10.1063/1.1884196.

[25] J. Kalkman, H. van Kesteren, Relaxation effects and high sensitivity photoacoustic detection of NO2 with a blue laser diode, Applied Physics B 90 (2) (2008) 197–200, ISSN 0946-2171, doi:10.1007/s00340-007-2895-0.

[26] G. Wysocki, A. A. Kosterev, F. K. Tittel, Influence of molecular relaxation dynamics on quartz-enhanced photoacoustic detection of CO2 at $\lambda = 2\ \mu$m, Applied Physics B: Lasers and Optics 85 (2-3) (2006) 301–306, ISSN 09462171, doi:10.1007/s00340-006-2369-9.

[27] A. A. Kosterev, T. S. Mosely, F. K. Tittel, Impact of humidity on quartz-enhanced photoacoustic spectroscopy based detection of HCN, Applied Physics B: Lasers and Optics 85 (2-3) (2006) 295–300, ISSN 09462171, doi:10.1007/s00340-006-2355-2.

[28] A. A. Kosterev, Y. A. Bakhirkin, F. K. Tittel, S. McWhorter, B. Ashcraft, QEPAS methane sensor performance for humidified gases, Applied Physics B: Lasers and Optics 92 (1) (2008) 103–109, ISSN 09462171, doi:10.1007/s00340-008-3056-9.

[29] T. Starecki, P. Z. Wieczorek, A high sensitivity preamplifier for quartz tuning forks in qepas (Quartz enhanced photoacoustic spectroscopy) applications, Sensors (Switzerland) 17 (11), ISSN 14248220, doi:10.3390/s17112528.

[30] N. Ullah, S.-j. Park, Y. J. Lee, S. Park, Investigation of the Electrical Model Parameters of Quartz Tuning Forks from a Low-frequency Impedance Analysis Using a Lock-in Amplifier, New Physics: Sae Mulli 65 (1) (2015) 76–80, ISSN 0374-4914, doi:10.3938/NPSM.65.76.

[31] P. Patimisco, G. Scamarcio, F. Tittel, V. Spagnolo, Quartz-Enhanced Photoacoustic Spectroscopy: A Review, Sensors 14 (4) (2014) 6165–6206, ISSN 1424-8220, doi:10.3390/s140406165.

[32] A. Stylogiannis, L. Prade, A. Buehler, J. Aguirre, G. Sergiadis, V. Ntziachristos, Continuous wave laser diodes enable fast optoacoustic imaging, Photoacoustics 9 (2018) 31–38, ISSN 22135979, doi:10.1016/j.pacs.2017.12.002, URL `http://dx.doi.org/10.1016/j.pacs.2017.12.002`.

[33] R. Bartlome, M. Kaučikas, M. W. Sigrist, Modulated resonant versus pulsed resonant photoacoustics in trace gas detection, Applied Physics B: Lasers and Optics 96 (2-3) (2009) 561–566, ISSN 09462171, doi:10.1007/s00340-009-3572-2.

Appendix A. Beam Profile of the Focused Beam

The 2D projection of the focused laser spot was measured by means of a beam profiler (Thorlabs: BC106N-VIS/M). The horizontal and vertical ellipse diameters are 116 µm and 282 µm, respectively.

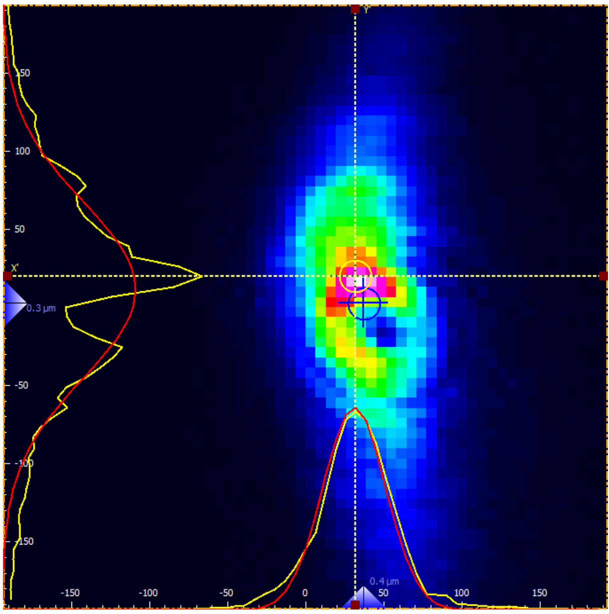

Figure A.12: 2D projection of the focused laser spot.

Appendix B. Determination of the Thermal Noise

A QTF can be electrically modelled by a Butterworth-Van Dyke circuit (Fig. 8) [30]. To determine the resistance R, we proceeded as follows: (i) de-focus the laser to hit the prongs and thermally excite the QTF, which produces a current, proportional to the admittance of the QTF (ii) sweep through the frequencies of interest, and fit the imaginary and real part of the response signal to the imaginary and real part of the admittance of the Butterworth-Van Dyke circuit, (iii) as the driving voltage, which equals to the thermal excitation is not known, the capacitance C_p is measured, and (iv) inserted as a scaling factor to determine all relevant values.

The real and imaginary parts of the admittance Y are given by Eqs. (B.1) and (B.2). In addition to the equations from Ullah et al. [30], a parallel admittance Y_p was added to Eq. (B.1) for baseline correction.

$$Re(Y) = Y_p + \frac{1}{R} \cdot \frac{\omega^2 \cdot \omega_m^2}{(Q \cdot (\omega^2 - \omega_m^2))^2 + \omega^2 \cdot \omega_m^2} \tag{B.1}$$

$$Im(Y) = \omega \cdot C_p \cdot \\ \cdot \frac{\omega^4 - \omega^2 \cdot (\omega_p^2 + \omega_m^2 \cdot (1 - 1/Q^2)) + \omega_m^2 \cdot \omega_p^2}{((\omega^2 - \omega_m^2)^2 + \omega^2 \cdot \omega_m^2/Q^2)} \tag{B.2}$$

In these equations, $\omega = 2\pi f$, $\omega_m = \frac{1}{\sqrt{LC_m}}$, $\omega_p = \frac{1}{\sqrt{L\frac{C_m C_p}{C_m + C_p}}}$, and $Q = \frac{\omega_m L}{R}$.

The corresponding measurements display the real- and imaginary part of the photoacoustic signal, which is proportional to the admittance. Corresponding fits are displayed in Fig. B.13.

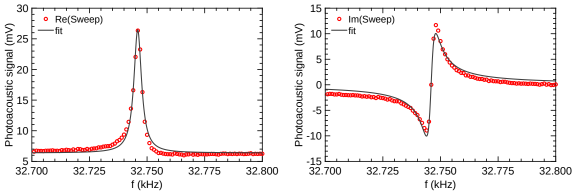

(a) (b)

Figure B.13: Real 13(a) and imaginary 13(b) parts of the photoacoustic signal (black), proportional to the real and imaginary part of the admittance (fit in red).

The capacitance C_p was measured from an open QTF of the same model by means of a precision LCR Meter (KEYSIGHT E4980AL), resulting in a value of 1.86 pF.

From ω_p and ω_m of the fits, C_m is calculated via $C_m = ((\frac{\omega_p}{\omega_m})^2 - 1) \cdot C_p$. By knowing C_m, L is calculated from ω_m. Finally, R is calculated from ω_m, L, and Q as 85.7 kΩ.

To compare the theoretical noise to the actual noise of the circuit, the average noise spectrum of the QTF signal with the laser switched off was investigated (Fig. B.14). As the signal was acquired after the second amplifier, it has to be divided by the amplification of the second amplifier, resulting in a noise of 1.48 µV.

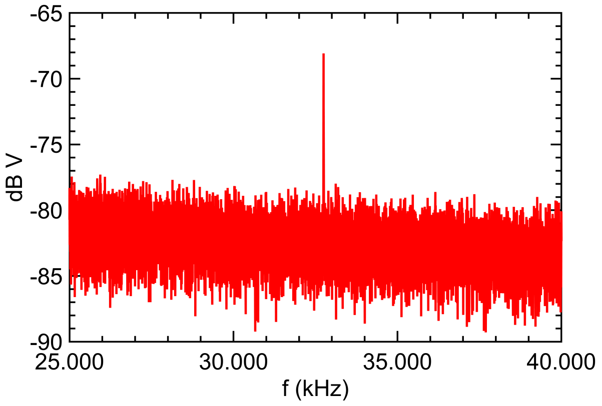

Figure B.14: FFT of the average noise floor of the QTF after the second amplifier (factor of 270 higher than the value after the transimpedance amplifier) with the laser switched off. The noise peak at the resonance frequency is $-68\,\mathrm{dBV}$, equivalent to $0.4\,\mathrm{mV}$.

Appendix C. Drift due to the Laserpower

To investigate whether drift is dominated by fluctuations of the laser power, an Allan deviation analysis, based on the same time resolution as the noise analysis, was carried out. As can be seen in Fig. C.15, a drift of the laserpower is appearing at the same timescale (around 120 s), which indicates that drift is caused by fluctuations of the laserpower.

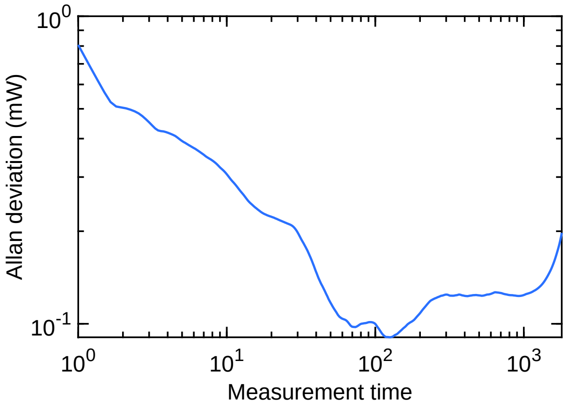

Figure C.15: Allan deviation of the laserpower as a function of the averaging time.

D.5 Paper 5

Aerosol Science and Technology

ISSN: 0278-6826 (Print) 1521-7388 (Online) Journal homepage: https://www.tandfonline.com/loi/uast20

Soot mass concentration sensor using quartz-enhanced photoacoustic spectroscopy

Philipp Breitegger, Mario A. Schriefl, Robert T. Nishida, Simone Hochgreb & Alexander Bergmann

To cite this article: Philipp Breitegger, Mario A. Schriefl, Robert T. Nishida, Simone Hochgreb & Alexander Bergmann (2019) Soot mass concentration sensor using quartz-enhanced photoacoustic spectroscopy, Aerosol Science and Technology, 53:9, 971-975, DOI: 10.1080/02786826.2019.1635677

To link to this article: https://doi.org/10.1080/02786826.2019.1635677

AEROSOL SCIENCE AND TECHNOLOGY
2019, VOL. 53, NO. 9, 971–975
https://doi.org/10.1080/02786826.2019.1635677

AEROSOL RESEARCH LETTER

OPEN ACCESS

Soot mass concentration sensor using quartz-enhanced photoacoustic spectroscopy

Philipp Breitegger[a], Mario A. Schriefl[a], Robert T. Nishida[b], Simone Hochgreb[b], and Alexander Bergmann[a]

[a]Institute of Electronic Sensor Systems, Graz University of Technology, Graz, Austria; [b]Department of Engineering, University of Cambridge, Cambridge, United Kingdom

ARTICLE HISTORY Received 21 January 2019; Accepted 9 June 2019

EDITOR Hans Moosmüller

1. Introduction

Photoacoustic spectroscopy (PAS) is a well-established method for sensitive and selective detection of trace gases such as NO_2 and CO_2 (Bozóki, Pogány, and Szabó 2011) as well as for the measurement of aerosol particles (e.g., Petzold and Niessner 1996). Commercial instruments for measuring soot concentrations of vehicle exhaust reach detection limits of $5\,\mu g\ m^{-3}$ (corresponding to $50\,Mm^{-1}$ for 1 s integration time) and offer a dynamic range of four orders of magnitude, enabling wide commercial success in the automotive industry (AVL List GmbH 2018; Giechaskiel et al. 2014; Lack et al. 2006). However, the high cost, size, and mass of conventional PAS systems (e.g., AVL Micro Soot Sensor [MSS]: $W \times H \times D = 483\text{ mm} \times 400\text{ mm} \times 555\text{ mm}$, $m \approx 26\text{ kg}$) has limited its applicability for widespread use in ambient or environmental monitoring.

Photoacoustic instruments for soot measurement typically use an intensity modulated light source to transfer energy to soot particles (Petzold and Niessner 1996). Thermal relaxation of the soot particles produces an acoustic wave with a frequency that matches the modulation of the light source. For sufficiently small particles, the amplitude of the acoustic wave is directly proportional to the absorbed light energy and therefore to the soot mass absorption (Cremer et al. 2017). In conventional photoacoustic instruments the amplitude of the acoustic wave is usually amplified with a quality factor of around 10–80 (Bozóki, Pogány, and Szabó 2011; Rück, Bierl, and Matysik 2017; Yin et al. 2017) using organ-pipe-like acoustic resonators at resonance frequencies in the low kHz-range and detected with a conventional microphone (Bozóki, Pogány, and Szabó 2011; Schindler et al. 2004; Wolf et al. 2014; Yin et al. 2017). In contrast, quartz-enhanced photoacoustic spectroscopy (QEPAS) (Kosterev et al. 2002), may use mass-produced quartz tuning forks (QTF) with a resonant frequency f_0 of 32.768 kHz to detect acoustic waves with quality factor Q of around 8000 at ambient pressure. The two-orders of magnitude increase in quality factor over conventional PAS enables sensing of trace gases down to the ppb level (Patimisco et al. 2014). The signal in QEPAS is directly proportional to the ratio of Q to f_0. Thus, by designing a custom QTF with reduced f_0 and a similar Q, the signal strength can be further increased in QEPAS at similarly small sizes (Patimisco et al. 2017). Additional advantages are (a) a small and simple sensor design, as the QTF combines the resonator and electric transducer in one component and (b) high background noise immunity, due to the quadrupole characteristic of the QTF (Russell 2000). For a commercial QTF relative to conventional PAS, the effect of background noise is reduced by a factor of 46 (Rück, Bierl, and Matysik 2018).

While QEPAS has been used to study single, laser-trapped droplets (Cremer et al. 2016), this is the first proof of principle of measuring a continuous flow of

---

CONTACT Philipp Breitegger p.breitegger@tugraz.at Institute of Electronic Sensor Systems, Graz University of Technology, Graz 8010, Austria
Color versions of one or more of the figures in the article can be found online at www.tandfonline.com/uast.

soot aerosol. The off-the-shelf QTF is smaller than 5 mm in the longest dimension. Such piezoelectric QTFs are mass-produced for use as a clock in, e.g., quartz watches and are available for prices in the cent range. Therefore, in contrast to conventional PAS instruments, a QEPAS sensor enables significant miniaturization and cost reduction, which would enable large scale monitoring of sources with environmental impact (Breitegger and Bergmann 2016).

In this work, a measurement setup for a miniaturized soot sensor with QEPAS is reported. Specifically, measurements of mass concentrations of soot from a miniCAST soot generator are compared with those from an MSS, which is a common method to measure mass concentrations of soot.

2. Methods

The QEPAS sensor includes a QTF placed in an aluminum cell which allows optical access. The cell is of size 65 mm × 40 mm × 40 mm including all analog amplification circuits as well as temperature and pressure sensors. For proof of principle, the optical components were placed in line with the cell, increasing its length to 160 mm. It is expected that with little engineering effort, a miniaturization by at least a factor of two is feasible. A laser beam enters the cell through an N-BK7 window and is focused between the two prongs of the QTF approximately 0.7 mm from the top of the prongs for a strong signal (cf. Kosterev et al. 2002). The QTF is placed in a volume of only 1.6 cm^3. A photodiode, placed behind an optical filter, monitors the laser's power. A 30 mW optical power FLEXPOINT® Dot Laser Module (Laser Components GmbH) with 850 nm wavelength was chosen, as it has minimal spectroscopic cross-interference to any gases possibly contained in ambient or combustion related aerosol. Further, the module provides the advantages of relatively small size (length <57 mm), low cost (around 200 EUR), a moderate laser safety class, and an integrated laser driver enabling modulation. The laser is modulated by means of a function generator (National Instruments: Model PXI-5402) which shares the same synchronization clock as the acquisition module (National Instruments: Model PXI-6281). The laser is modulated at the resonance frequency of the QTF (Fox Electronics: NC38LF) f_0, determined by a frequency sweep as described below. The aerosol inlet and outlet to the cell are positioned perpendicular to the laser beam direction. Soot particles absorb the modulated laser light and transfer the energy to the surrounding gas molecules, which produces a sound wave of frequency f_0, which excites the QTF. The QTF produces a current from piezoelectric vibrations that is amplified with a transimpedance amplifier. The signal is acquired with the PXI-6281 card at 250 kilosamples per second and demodulated at f_0 with a lock-in amplifier with 1 s integration time, which is realized as a custom LabVIEW application on a personal computer. For further analysis, the QEPAS sensor is equipped with temperature, humidity, and absolute pressure sensors.

A miniaturized electronic solution containing a lock-in amplifier and microcontroller giving similar results is described by Kerschhofer, Breitegger, and Bergmann (2018). As compared to commercial available instruments (MSS by AVL, PAX by Droplet Measurement Technologies) this results in a reduction of size, mass and price by at least a factor of 50.

The experimental setup enables control of mass concentrations of soot particles as well as verification of the size distribution and number concentrations of soot using an MSS and a scanning mobility particle sizer (SMPS) as reference instruments. The setup is shown in Figure 1. The soot aerosol was generated

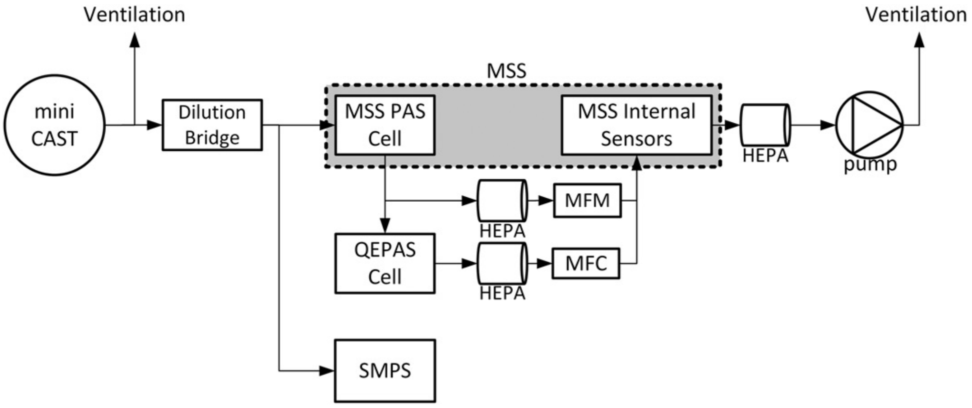

Figure 1. Setup to measure the linearity of the QEPAS cell.

with a miniCAST soot generator (Jing Ltd: Model 6204 Type B, flow settings: C_3H_8 (40 std cm^3 min^{-1}), oxidation air (500 std cm^3 min^{-1}), dilution air (5 std L min^{-1}), and quench gas N_2 (2 std L min^{-1}). The miniCAST was operated such that a size distribution with a geometric mean diameter of 78 nm was generated. To generate different soot concentrations a dilution bridge was used, which consists of a HEPA filter in parallel with a needle valve. The aerosol passed through the organ-like cell of a Micro Soot Sensor (AVL LIST GmbH) at a flow rate of 2 std L min^{-1}. To ensure the QEPAS cell measures the same particles as the MSS, the QEPAS cell was set in series to the PAS cell of the MSS. The flow rate through the QEPAS cell was fixed to 200 std cm^3 min^{-1} by means of a massflow controller (MFC; Vögtlin: Model GSC-B). The aerosol was also characterized using an SMPS (TSI Inc.: Model 3938).

For the determination of the soot mass concentration, the QEPAS signal was corrected for any changes in background. Before setting the dilution bridge to a new mass concentration, a HEPA filter was set in series with the mini CAST to obtain a background measurement. A sweep of the modulation frequency with 1 Hz resolution was performed around an interval of 10 Hz between the previously measured resonance frequency to obtain and adjust the modulation frequency accordingly. This was followed by the acquisition of the background signal for 30 s. The dilution was set such that the desired mass concentration was achieved, as measured by the MSS. The QEPAS signal was logged for 2 min. Each data point is made up of average of the last 30 s of the 2 min sampling time for both the QEPAS and MSS. Additionally, the size distribution of the produced soot was recorded with the SMPS for diagnostic reasons. To verify that the photoacoustic signal was immune to other effects, cross-interferences against NO_2, absolute pressure, and temperature variations were checked. Humidity remained almost constant during the measurements ((50 ± 3) % RH). The influence of humidity is the subject of further investigations. According to Arnott et al. (2003), operation of aerosol PA instruments below 65% RH is advised.

3. Results and discussion

Figure 2 shows the QEPAS signal as a function of the mass concentration of soot measured by the MSS. By performing a linear regression, the sensitivity was determined to be (8.08 ± 0.10) mV m^3 mg^{-1}. The coefficient of determination for the fit is $R^2 = 0.99$.

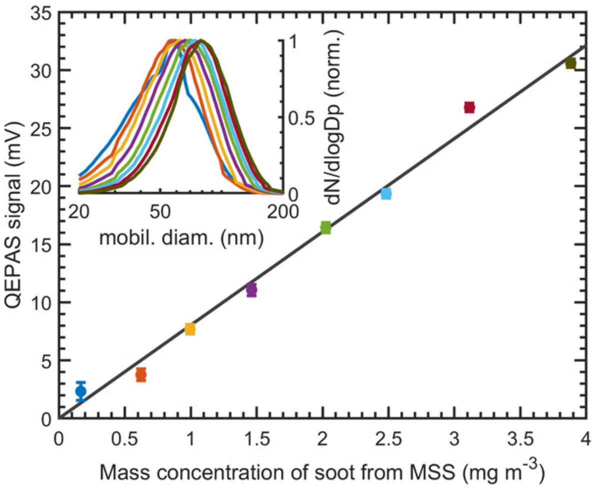

Figure 2. QEPAS signal in mV as a function of the mass concentration of soot particles measured by the micro-soot sensor (MSS). Error bars in the QEPAS signal represent the standard error relatively to the mean. Error bars for the mass concentrations as measured by the MSS are too small to be visible on this scale. The inset shows the measured size distributions with colors corresponding to each point. The best fit line assumes identical zero offsets at zero.

Each datapoint has a different color, which corresponds to the mobility size distribution shown in the inset of Figure 2. Throughout the measurements, the geometric mean diameter increased from 49 nm for the lowest concentration to 78 nm when the dilution bridge was at the lowest dilution and fully open. Deviations of the measurements from a linear slope in Figure 2 for larger particle diameters could not be seen within the investigated size ranges (Cremer et al. 2017).

Important considerations for aerosol sensors are long-term stability as well as the decrease in uncertainty due to increased time for signal averaging. This is commonly analyzed by the Allan deviation methodology (Werle, Mücke, and Slemr 1993), which consists in the standard deviation as a function of averaging time. Figure 3 shows the Allan deviation for a continuous sample drawn from HEPA filtered room air at 200 std cm^3 min^{-1}. The Allan deviation decreases up to an averaging time of 19 s. After that time, drift occurs, therefore, the 3σ noise equivalent concentration for 19 s would correspond to 80 µg m^{-3}. In this publication, a 30 mW laser module was selected to demonstrate the applicability of QEPAS for aerosol measurements. For easier compliance with laser regulations, the proof of principle experiments were performed with a low power laser module. Nevertheless by increasing the laser power to, e.g., 500 mW, we expect the limit of detection to be lowered to

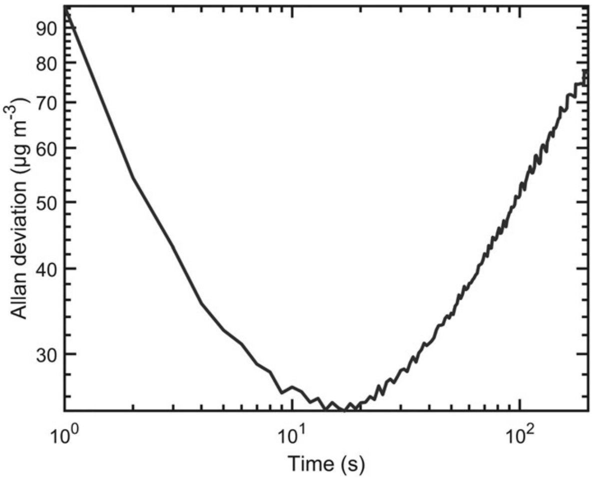

Figure 3. Allan deviation of the QEPAS sensor as a function of averaging time when using suction by a nozzle of ambient, filtered air.

4.8 µg m^{-3} without increasing the over-all sensor size. Furthermore, preliminary tests indicate that sensor fouling due to soot accumulation on the QTF was not detectable at an average soot loading of 2 mg/m^3 for 8 h.

4. Conclusions

In this work, soot mass concentration measurements using QEPAS are reported for the first time. A custom made QEPAS cell with designated aerosol sampling ports operated with a 30 mW laser module resulted in a limit of detection of 80 µg m^{-3} with an averaging time of 19 s. Given the small size, weight, and cost the instrument is suitable for environmental measurements close to the emission source. One possible application could be monitoring failures of particulate filters for diesel or gasoline engines (e.g., periodical technical inspections as well as real driving emission measurements). The results show excellent linearity with the reference instrument (MSS) over a wide range of mass concentrations of soot with negligible sensor fouling due to heavy soot loading.

Acknowledgments

The authors acknowledge AVL List GmbH for loaning the Micro Soot Sensor for the experiment.

Funding

Open access publication is supported by the TU Graz Open Access Publishing Fund.

ORCID

Philipp Breitegger http://orcid.org/0000-0003-3049-4921
Robert T. Nishida http://orcid.org/0000-0002-9820-1569
Simone Hochgreb http://orcid.org/0000-0001-7192-4786
Alexander Bergmann http://orcid.org/0000-0003-3343-8319

References

Arnott, W. P., H. Moosmüller, P. J. Sheridan, J. A. Ogren, R. Raspet, W. V. Slaton, J. L. Hand, S. M. Kreidenweis, and J. L. Collett. Jr. 2003. Photoacoustic and filter-based ambient aerosol light absorption measurements: Instrument comparisons and the role of relative humidity. *J. Geophys. Res.* 108 (D1):4034–4044. doi:10.1029/2002JD002165.

AVL List GmbH. 2018. Avl Micro Soot Sensor Operating Manual, Rev. 14. Graz, Austria.

Bozóki, Z., Pogány, A., and Szabó, G. 2011. Photoacoustic instruments for practical applications: Present, potentials, and future challenges. *Appl. Spectrosc. Rev.* 46 (1):1–37.

Breitegger, P., and A. Bergmann. 2016. Air quality and health effects – How can wireless sensor networks contribute? A critical review. In *2016 International Conference on Broadband Communications for Next Generation Networks and Multimedia Applications (CoBCom)*, vol. 9, 1–8. Graz, Austria: IEEE. http://ieeexplore.ieee.org/document/7593507/.

Cremer, J. W., K. M. Thaler, C. Haisch, and R. Signorell. 2016. Photoacoustics of single laser-trapped nanodroplets for the direct observation of nanofocusing in aerosol photokinetics. *Nat. Commun.* 7 (1):1–7. doi:10.1038/ncomms10941.

Cremer, J. W., P. A. Covert, E. A. Parmentier, and R. Signorell. 2017. Direct measurement of photoacoustic signal sensitivity to aerosol particle size. *J. Phys. Chem. Lett.* 8 (14):3398–3403. doi:10.1021/acs.jpclett.7b01288.

Giechaskiel, B., M. Maricq, L. Ntziachristos, C. Dardiotis, X. Wang, H. Axmann, A. Bergmann, and W. Schindler. 2014. Review of motor vehicle particulate emissions sampling and measurement: From smoke and filter mass to particle number. *J. Aerosol Sci.* 67:48–86. doi:10.1016/j.jaerosci.2013.09.003.

Kerschhofer, A., P. Breitegger, and A. Bergmann. 2018. Laser driver and analysis circuitry development for Quartz-Enhanced photoacoustic spectroscopy of NO2 for IoT purpose. *Proceedings.* 2 (13):1062. doi:10.3390/proceedings2131062.

Kosterev, A. A., Y. A. Bakhirkin, R. F. Curl, and F. K. Tittel. 2002. Quartz-enhanced photoacoustic spectroscopy. *Opt. Lett.* 27 (21):1902.

Lack, D. A., E. R. Lovejoy, T. Baynard, A. Pettersson, and A. R. Ravis- Hankara. 2006. Aerosol absorption measurement using photoacoustic spectroscopy: Sensitivity, calibration, and uncertainty developments. *Aerosol Sci. Technol.* 40 (9):697–708. doi:10.1080/02786820600803917.

Patimisco, P., A. Sampaolo, H. Zheng, L. Dong, F. K. Tittel, and V. Spagnolo. 2017. Quartz-enhanced photoacoustic spectrophones exploiting custom tuning forks: A review. *Adv. Phys.* 2 (1):169–187. doi:10.1080/23746149.2016.1271285.

Patimisco, P., G. Scamarcio, F. Tittel, and V. Spagnolo. 2014. Quartz-enhanced photoacoustic spectroscopy: A review. *Sensors*. 14 (4):6165–6206. doi:10.3390/s140406165.

Petzold, A., and R. Niessner. 1996. Photoacoustic soot sensor for in-situ black carbon monitoring. *Appl. Phys. B.* 63 (2):191–197. doi:10.1007/BF01095272.

Rück, T., R. Bierl, and F. M. Matysik. 2017. Low-cost photoacoustic NO_2 trace gas monitoring at the pptV-level. *Sens. Actuat. A.* 263 (2):501–509. doi:10.1016/j.sna.2017.06.036.

Rück, T., R. Bierl, and F. Michael Matysik. 2018. NO_2 trace gas monitoring in air using off-beam quartz enhanced photoacoustic spectroscopy (QEPAS) and interference studies towards CO_2, H_2O and acoustic noise. *Sens. Actuat. B.* 255 (2):2462–2471. doi:10.1016/j.snb.2017.09.039.

Russell, D. A. 2000. On the sound field radiated by a tuning fork. *Am. J. Phys.* 68 (12):1139–1145. doi:10.1119/1.1286661.

Schindler, W., C. Haisch, H. A. Beck, R. Niessner, E. Jaco, and D. Rothe. 2004. A photoacoustic sensor system for time resolved quantification of diesel soot emissions. In *SAE 2004 World Congress & Exhibition*, SAE International in United States, March 8. http://papers.sae.org/2004-01-0968/. https://www.sae.org/content/2004-01-0968/.

Werle, P., R. Mücke, and F. Slemr. 1993. The limits of signal averaging in atmospheric trace-gas monitoring by tunable diode-laser absorption spectroscopy (TDLAS). *Appl. Phys. B.* 57 (2):131–139.

Wolf, J. C., A. Danner, R. Niessner, and C. Haisch. 2014. NO_2 measurement artifacts in the presence of soot. *Anal. Bioanal. Chem.* 406 (2):447–453. doi:10.1007/s00216-013-7495-8.

Yin, X., L. Dong, H. Wu, H. Zheng, W. Ma, L. Zhang, W. Yin, S. Jia, and F. K. Tittel. 2017. Sub-ppb nitrogen dioxide detection with a large linear dynamic range by use of a differential photoacoustic cell and a 3.5 W blue multimode diode laser. *Sens. Actuat. B.* 247:329–335. doi:10.1016/j.snb.2017.03.058.